Summer 8-31-2004

Fluidization of agglomerates of nanoparticles under different force fields

Jose A. Quevedo
New Jersey Institute of Technology

ABSTRACT

FLUIDIZATION OF AGGLOMERATES OF NANOPARTICLES UNDER DIFFERENT FORCE FIELDS

by
Jose A. Quevedo

Nanoparticles are the focus of many research activities, and in the near future they will be handled in large amounts by industry. Fluidization is a very important unit operation which is applied in several industrial processes.

In the present work, fluidization experiments with agglomerates of nanoparticles were done under different force fields: (1) gravity force or conventional fluidization; (2) a magnetic force field, which uses magnetic particles under the influence of a magnetic field; and (3) a centrifugal force, generated by a rotating frame that simulates higher gravity conditions.

Among the significant results with agglomerates of nanoparticles, conventional fluidization was possible by separating out large agglomerates from the bed; the movement of magnetic particles at the bottom of the fluidized bed enhanced the fluidization by increasing the bed expansion and avoiding the bypass of gas through the bed under the form of bubbles; fluidization of the agglomerates in a rotating fluidized bed was accomplished under different simulated gravity conditions, which allowed to fluidize the agglomerates under higher than normal gas flow conditions. Theoretical approaches for the estimation of the agglomerate size and the bed pressure drop were included.

FLUIDIZATION OF AGGLOMERATES OF NANOPARTICLES UNDER DIFFERENT FORCE FIELDS

by
Jose A. Quevedo

A Thesis
Submitted to the Faculty of
New Jersey Institute of Technology
In Partial Fulfillment of the Requirements for the Degree of
Master of Science in Chemical Engineering

Department of Chemical Engineering

August 2004

APPROVAL PAGE

FLUIDIZATION OF AGGLOMERATES OF NANOPARTICLES UNDER DIFFERENT FORCE FIELDS

Jose A. Quevedo

Dr. Robert Pfeffer, Thesis Advisor — Date
Distinguished Professor, Dept. of Chemical Engineering, NJIT

Dr. Rajesh N. Dave, Committee Member — Date
Professor, Dept. of Mechanical Engineering, NJIT

Dr. Norman W. Loney, Committee Member — Date
Associate Professor, Dept. of Chemical Engineering, NJIT

BIOGRAPHICAL SKETCH

Author: Jose A. Quevedo

Degree: Master of Science

Date: August 2004

Undergraduate and Graduate Education:

- Master of Science in Chemical Engineering,
  New Jersey Institute of Technology, Newark, NJ, 2004

- Engineer Degree in Chemical Engineering,
  National University of Engineering, Lima, Peru, 2002

- Bachelor of Science in Chemical Engineering,
  National University of Engineering, Lima, Peru, 1998

Major: Chemical Engineering

Publications:

J. Quevedo, H. Nakamura, R. Dave, R. Pfeffer, S. Watano, "Fluidization of Nanoparticles in a Rotating Fluidized Bed," *in preparation*.

Q. Yu, J.Quevedo, R. Pfeffer, R. Dave, C. Zhu, ""Fluidization of Nanoparticle Agglomerates with the Assistance of Magnetic Particles in an Oscillating Magnetic Field," *in publication*.

This thesis is dedicated to my family and best friends.

(Dedicada a mi familia y mis mejores amigos.)

ACKNOWLEDGMENT

I cannot find the words to express my gratitude toward Dr. Robert Pfeffer who advised and supported me during the development of the present work and my graduate studies. Actually, he called my attention to do research in the field of fluidization. I am and will be very grateful for the opportunity he gave me to work under his supervision at the New Jersey Center for Engineered Particles.

I would like to acknowledge the support and advice from Dr. Rajesh Dave, member of the committee. I feel deeply in debt to him for his advice during my research work.

I thank Dr. Norman Loney very much for being a member of the committee and for his encouragement and understanding.

I would like to acknowledge the support of the National Science Foundation through the Award Number 0210400 dedicated to the study of Nanodomains and Nanoparticles.

I have to mention my colleagues, Caroline Nam, Qun Yu, Yueyang Shen and Gary Liu; without their assistance much of the present work could not have been possible. Thank you so much for your patience, encouragement, and advice. In addition, I am grateful to all the staff at the NJCEP who shared their experience with me, and in particular to Dr. Dongguang Wei, Dr. Jun Yang and Dr. Junya Kano.

TABLE OF CONTENTS

TABLE OF CONTENTS
(Continued)

LIST OF TABLES

LIST OF FIGURES

LIST OF FIGURES
(Continued)

LIST OF FIGURES
(Continued)

LIST OF FIGURES
(Continued)

LIST OF FIGURES
(Continued)

LIST OF SYMBOLS

a	Constant in Equation 3.1, dimensionless
b	Constant in Equation 3.1, dimensionless
A	Hamaker constant, J (usually $A=10^{-19}$ J approximately)
Ar	Archimedes number, dimensionless
A_t	Transversal area of the fluidization column, m^2
C_D	Drag coefficient, dimensionless
d_c	Channel height, m
d_p	Diameter of particle, m
E_k	Ekman number, dimensionless
$\mathbf{f}$	Vectorial force, N
F	Force, N
F_b	Buoyancy force, N
F_c	Cohesive force, N
F_d	Drag force, N
F_g	Gravitational force, N
F_e	Adhesion force transmitted in particle contact, N
g	Gravitational acceleration, m/s^2 (9.8)
g_c	Conversion factor, 1 $N.s^2/(kg.m)$
G	Gravitational factor, dimensionless
H	Fluidized bed height, cm
H_0	Initial bed height at no flow, cm

LIST OF SYMBOLS
(Continued)

$\underline{i_r}$	Unit vector in the radial direction, dimensionless
$\underline{i_\theta}$	Unit vector in the angular direction, dimensionless
$\underline{i_k}$	Unit vector in the axial direction, dimensionless
k_1	Energy cohesive constant, J/nm
K_1	Constant, dimensionless
K_2	Constant, dimensionless
K_3	Constant in Equation 2.5
N	Number of particles per unit volume, $1/m^3$
n	Richardson & Zaki index, dimensionless
L	Length relative to the Ro or Ek numbers, cm
L_C	Length of the channel in Equation 3.16, m
L_m	Length of the bed expansion, m
L_{mf}	Length of the bed expansion at minimum fluidization, m
P	Pressure, Pa
P_O	Pressure at the beginning of the channel, Pa
P_L	Pressure at the end of the channel, Pa
P_r	Radial pressure, Pa
r	Radial direction, m
R	Radius of the channel in Equation 3.16, m
Re	Reynolds number, dimensionless

LIST OF SYMBOLS
(Continued)

Re_p	Reynolds number based on particle diameter, dimensionless
$Re_{p,mf}$	Reynolds number based on particle diameter at minimum fluidization conditions, dimensionless
Re_t	Reynolds number based on particle diameter at terminal velocity conditions, dimensionless
Re_Ω	Reynolds number based on angular velocity, dimensionless
Ro	Rossby number, dimensionless
t	Time, s
u	local fluid velocity, cm/s
u_o	fluid velocity, cm/s
U	Gas velocity, cm/s
U_{mf}	Minimum fluidization velocity, cm/s
U_{mb}	Minimum bubbling velocity, cm/s
U_p	Particle velocity, cm/s
u_g	Fluidization velocity, m/s
u_{mf}	Minimum fluidization velocity, cm/s
u_r	Fluid radial velocity, m/s
u_t	Terminal velocity of the particle, m/s
U_t	Terminal velocity of the particle, m/s
v	Local velocity of the particle in Equation 2.18, m/s
$\mathbf{v}$	Fluid velocity vector, m/s

$\mathbf{v}_\theta$	Tangential fluid velocity, m/s
$\mathbf{v}_r$	Radial fluid velocity, m/s
v_t	Terminal velocity of the particle, m/s
V_p	Volume of particle, m^3
V_f	Volumetric flow rate of the fluid, m^3/s
V_s	Volumetric flow rate of the solid particles, m^3/s
w	Mass rate of flow, kg/s
W	Weight of the bed of powder, N
z	*B*ed expansion, m

Greek letters

ε	Void fraction or interparticle voidage, dimensionless
ε_m	Void fraction, dimensionless
ε_I	Empty spaces inside the agglomerate of nanoparticles, dimensionless
ε_{mf}	Void fraction at minimum fluidization, dimensionless
μ	Fluid viscosity, $(N.s/m^2)$
μ_f	Fluid viscosity, $(N.s/m^2)$
μ_g	Viscosity of the gas, $(N.s/m^2)$
ρ_a	Density of agglomerate, kg/m^3

LIST OF SYMBOLS
(Continued)

ρ_b	Bulk density of the bed of agglomerates, kg/m^3
ρ_f	Gas or fluid density, kg/m^3
ρ_p	Particle density, kg/m^3
ρ_s	Solid particle density, kg/m^3
δ	Distance between two particles, nm
Ω	Angular speed, rd/s
ϕ	Solids volume fraction, dimensionless
ϕ_s	Sphericity of a particle, dimensionless
Δp	Bed pressure drop, Pa
τ_{rz}	Shear stress, Pa

CHAPTER 1

INTRODUCTION

1.1 Overview

The study of the fluidization phenomena is a focus of attention in many industries and it has been a subject of research for a very long time. The most significant application of the fluidization technique is found in catalytic cracking of heavy hydrocarbons in refineries. The fluidization regime implies high rates of mass and heat transfer and involves a mixture of solid particulates in a fluid medium. Therefore, its application in processes that depend on the use of particulates as either reactants or catalyst and high rates of transport is very common.

The fluidization process is characterized by the presence of a fluid phase and a solid phase, which interact in terms of momentum, heat and mass transfer depending on the application and materials involved. There are several types of fluidization, but they can be classified by the continuous phase involved in the process; thus, there is liquid phase fluidization and gas phase fluidization. The material that is fluidized is a powder which can be defined as a finely divided solid. The particle primary sizes can vary from thousands of micrometers to a very few nanometers; however, due to strong cohesive forces, small particles tend to group together, forming agglomerates of about several micrometers or larger. Many industrial applications already exist that use fluidization of millimeter and micron size particles. However, since the uses of nanoparticles

are relatively new, few fluidization applications exist and the behavior of the nanoparticles agglomerates is not well known.

The fluidization of agglomerates of nanoparticles has become of great interest recently because current research on the production of these nanoparticles is underway and the handling of these powders in large quantities will be a major concern for industries in the near future. Actually, in the production process of these powders, fluidization is used for removal of residual reactants from the particles or to change their surface properties by coating them. In addition, agglomerates of nanoparticles are used in several applications such as sealants, paints, coatings, printing inks, toners, adhesives, gels, catalyst carriers, stabilizer agents. Many other potential applications are in development.

The present work is focused on the gas fluidization of agglomerates of nanoparticles, particularly fumed silica. Different fluidization methods were applied, such as conventional fluidization, in which fluidization of agglomerates takes place only by passing gas through them at high velocities. Other methods involve the use of external forces to break up the cohesion between particles, such as the movement of magnetic particles under the presence of an oscillating magnetic field. Another external force is a high centrifugal force field generated by a rotating frame.

1.2 How Nanoparticles are Produced

The powders used in the experiments of the present work were produced by Degussa Corporation (Mangold et al., 1999). They use the pyrogenic process, which has been developed for large scale synthesis of nanoparticles. The fumed silica nanoparticles formation reaction is:

$$SiCl_4 + O_2 + H_2 \rightarrow SiO_2 + 2\,HCl \qquad \text{(under high temperature)} \qquad (1.1)$$

The $SiCl_4$ is vaporized at a temperature of about 90°C, and then it is mixed with hydrogen and oxygen; this gaseous mixture is then ignited and burned in a combustion chamber of a water cooled flame reactor. After the cooling off of the reaction gases, the pyrogenic silica is separated from the hydrogen chloride gases in a filter unit. The pyrogenic silica is then treated in a deacidification unit for a very short time (20 to 30 seconds) at a moderate temperature of about 600°C with steam and air.

In general, the same principle is applied for the production of nanoparticles of oxides of other materials such as titanium, using as a raw material a chlorinated compound. The nanoparticles studied in this research are Aerosil® R974, Aerosil® R972, Aeroxide® Titanium Dioxide P25, Iron Oxide, and Aeroxide® Aluminum Oxide C. Their primary particle size is about 12 to 21 nm, and they form agglomerates of about several tenths or hundreds of microns.

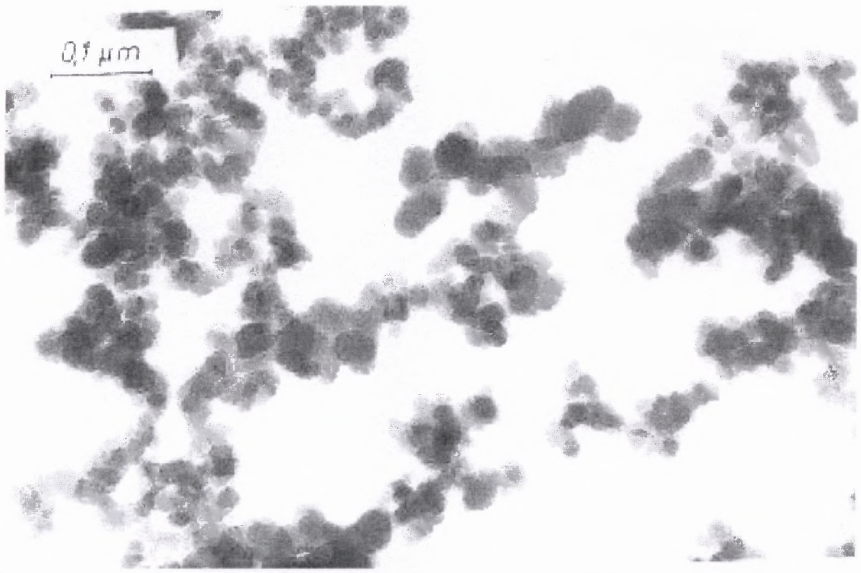

Figure 1.1 Nanoparticles agglomerated product of the pyrogenic process.

1.3 Previous Studies About Fluidization of Nanoparticles

Many of the fluidization principles already known apply to the fluidization of agglomerates of nanoparticles; however, these agglomerates of nanoparticles have a very low density based on a fractal porous structure, characteristics that are different from agglomerates of micron size particles. The lower density and irregular shape give agglomerates of nanoparticles a different hydrodynamic behavior reflected in a very low minimum fluidization velocity and high bed expansion.

For example, the Ergun equation for the pressure drop across packed spheres and the Stokes equation for the terminal velocity have been used by many researchers to estimate the fluidization behavior, but in combination with parameters that represent the bed voidage and shape of the particles (sphericity). Stokes, in 1851, derived an equation for the viscous resistance to the motion of a single spherical particle falling in an infinite fluid; a force balance

approach was used in this derivation which included the drag force which characterizes the interaction between the solid sphere and the fluid medium.

Among previous research work in fluidization, Richardson & Zaki (1954) had shown the existence of an exponential relationship between the porosity of the bed and the ratio of the gas and the settling velocities. Their result is important because it allows the estimation of the size of the particles based on gas velocity and bed voidage data. The Richardson & Zaki equation, applied to the fluidization of agglomerates of nanoparticles has been studied by Nam et al. (2004). Nam et al. used fractal dimension theory to estimate the number of primary particles in typical agglomerates; by selecting an appropriate Richardson & Zaki index, the agglomerate size was estimated.

Wang et al. (2000) studied the conventional fluidization of agglomerates of nanoparticles. They found that the gas velocity corresponding to the minimum fluidization velocity for different kinds of nanoparticles was about 1 cm/s but not larger than 10 cm/s, very low values when comparing to micron size particles. In addition, elutriation of agglomerates of nanoparticles could be seen at even these small gas velocities.

In order to solve the elutriation problem, the fluidization of agglomerates of nanoparticles is being enhanced by applying external forces, like magnetic particles moving under the effects of a magnetic field, vibration of the bed, fluidization assisted by sound, or fluidization under high gravity forces simulated by a rotating fluidized bed. All these methods have been previously applied to micron-size particles.

For vibrated assisted fluidization, Nam et al. (2003) have shown experimental data regarding the enhancement of the fluidization of agglomerates of nanoparticles by reducing the minimum fluidization velocity, increasing bed expansion, decreasing elutriation to almost zero, and increasing the stabilization of the fluidized bed by extending the settling time after the vibration is turned off.

Research on the magnetically assisted fluidization and the fluidization in a rotating frame are the object of study in the present work. Previous research on magnetically assisted fluidization has only been done with all magnetic particles and a mixture of magnetic and non-magnetic particles. However, in all of these previous studies the magnetic particles were fluidized wheras in this study the magnetic particles remained at the bottom of the bed and simply served to break up the interparticle forces of the large nanoagglomerates.

The rotating fluidized bed is a technology that has been used for several applications in the past and it is still in development. Filtering of soot gases from a diesel combustion machine was done in a rotating fluidized bed unit, due to its capacity to accept high flow rates; moreover, past experiments on gas-solid fluidization of micron size particles (Qian et al., 2001), and coating and/or granulation of fine powders were carried out in a rotating fluidized bed giving good results and showing that the rotating fluidized bed (RFB) is a promising technology (Watano et al., 2001). However, the fluid pattern inside of a RFB is not completely known; therefore, in the present work, the fluid behavior inside of the rotating frame is analyzed by using computational fluid dynamic (CFD) methods.

1.4 Objectives of the Present Study

This research work covers the fluidization of agglomerates of nanoparticles under different external forces, in which the following methods are studied: conventional fluidization, magnetically assisted fluidization and fluidization in a rotating frame. The powders studied are fumed silica, titanium dioxide, iron oxide and aluminum oxide (Aerosil® R972, Aerosil® R974, Aeroxide® P25 and Aeroxide® Aluminum Oxide C).

Several aspects of the fluidization of agglomerates of nanoparticles such as the experimental setup, the fluidization behavior and some preliminary modeling are described. One of the major objectives is to characterize and describe the peculiar fluidization behavior of these powders and subsequently, after analysis of the data, some modeling is proposed to explain the fluidization characteristics regarding the estimation of the agglomerate size for conventional fluidization and bed pressure drop for fluidization in a rotating assembly.

1.5 Organization of the Thesis

The present chapter has been an overview of the objectives of the research. By introducing how particles are made, it is shown that some nanoparticles are produced by the pyrogenic process; however, due to their small size and high surface area strong cohesive forces are present leading to the formation of agglomerates several times larger than the primary particle size.

In Chapter 2, the basic concepts of fluidization are introduced. A summary of the hydrodynamic classification of powders and the most important

parameters that describe fluidization are mentioned, such as bed pressure drop, minimum fluidization velocity, terminal velocity and bed empty voidage. Since the bed voidage fraction is a variable involved in many of the models, such as the Richardson & Zaki equation, the theory related to the bed voidage has been emphasized in this chapter.

Chapter 3 describes the conventional fluidization of agglomerates of nanoparticles. The experimental work, procedures and results of fluidization experiments with Aerosil® R974 are explained extensively. The Richardson & Zaki equation was applied to the fluidization results, allowing the estimation of the agglomerate size based on the terminal velocity. Furthermore, since fluctuations in some variables, such as the bed pressure drop, were observed and a mechanism that explains this phenomenon was developed.

The role of an external force field generated by the movement of magnetic particles under the influence of an oscillating magnetic field is evaluated in Chapter 4 for Aerosil® R974. In this chapter, the behavior of the magnetic particles under an oscillating magnetic field and its characterization gives an idea of how magnetic particles work in fluidization experiments. Several parameters of the fluidization experiments were changed such as the magnetic field intensity, frequency and weight of magnetic particles. Among the conclusions, the amount of magnetic particles used plays a significant role in the fluidization results which also depend on the magnetic field intensity.

The fluidization of agglomerates of nanoparticles in a rotating fluidized bed is the object of study in Chapter 5. The experimental conditions are explained in

detail as well as the results of the experiments. Moreover, as previous theoretical models show some discrepancies with the experimental data, a novel model based on the Navier-Stokes equation in a rotating frame was derived. Not withstanding the difficulties in getting an analytical solution to the Navier-Stokes equation for a rotating fluidized bed, the new model based on a rotating frame of reference allowed us to identify several additional forces that can play a role in the fluidization of powders depending on the rotating speed, the velocity and pressure of the fluid at the entry and the geometry of the unit. These were subsequently verified by using a computational fluid dynamic (CFD) program (Fluent®).

CHAPTER 2

PREVIOUS CONCEPTS IN FLUIDIZATION

2.1 Introduction

Fluidization is the term commonly used to refer to a fine solid matter when it behaves like a liquid by the passage of a fluid at a certain rate above a critical value and without having been exposed to a temperature high enough to make a phase transition from solid to liquid state. It can be also understood as the dilution of particulate solid matter by gas or liquid. Many publications describe the fluidization phenomena as shown below.

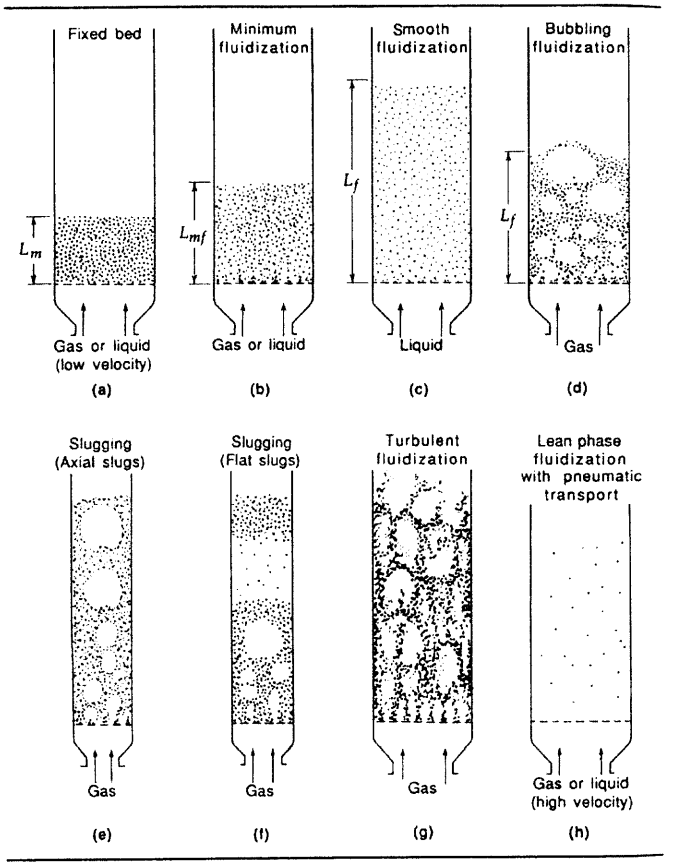

Figure 2.1 Different stages in fluidization (Kunii et al., 1991).

There are mainly three stages: Pre-fluidization, fluidization and conveying; the characteristics of these stages are different depending on the powder size, density and structure. Pre-fluidization can be defined as the state in which either there is not enough fluid through the bed or the bed is too cohesive so that only bubbling, channeling and/or spouting occurs; the pressure drop is not equal to the bed weight which means that the powder has not been lifted, and the gas is not evenly distributed in the bed of powder; this condition is also called incipient fluidization. A bed of powder is fluidized when the pressure drop is equal to the bed weight, which means that all the powder is being lifted; in addition, the gas is evenly distributed through the bed of powder and it acquires a liquid like behavior. Finally, the conveying stage, can be defined as the one in which solid particles start to abandon the dense-phase of the fluidized bed, and are carried out of the system following the path of the gas since they are driven by a superficial velocity larger than their terminal velocity.

The classification of the solid particulates in fluidization can be based on their hydrodynamic response. According to the literature (Gupta et al., 1999), several classifications can be found as follows: Geldart groups (1973), Molerus groups (1982) and Clark et al. (1986) groups. The reason for these classifications is for extrapolating data of fluidization only among the same class of powders. As shown in Figure 2.2, Geldart classified the powders by the difference in density between the fluidized gas (i.e., air and solid) and the mean size of the particles; Groups A and B are suitable for fluidization while Group C is

very difficult to fluidize and Group D is spoutable. The numerical criteria for the plot in Figure 2.2 defined by Geldart are as follows:

$$\left(\rho_s - \rho_f\right) \cdot d_p \leq 225 \qquad \text{for Group A} \qquad (2.1)$$

this is the boundary between Group A and Group B powders,

$$\left(\rho_s - \rho_f\right) \cdot d_p^2 \geq 10^6 \qquad \text{for Group D} \qquad (2.2)$$

Equation 2.2 is the boundary between Groups B and D powders. Geldart did not provide a criteria for the boundary line between Group A and Group C powders.

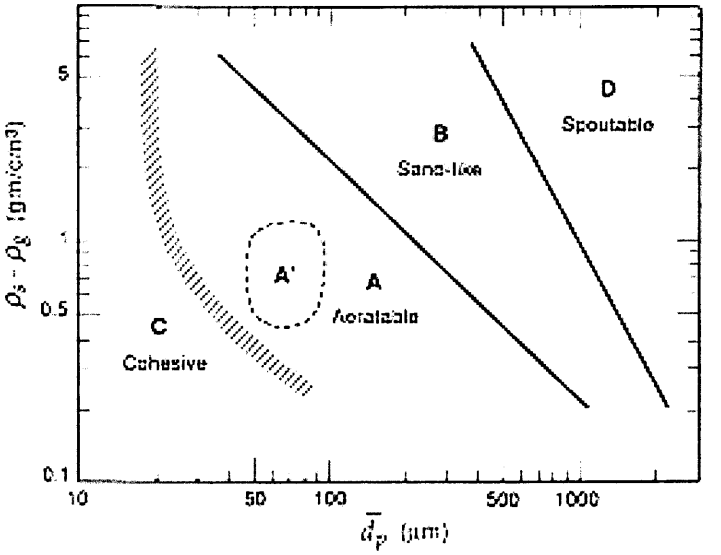

Figure 2.2 Classification by Geldart.

Similarly, Molerus proposed some criteria to group the powders by considering the interparticle force as well as the drag exerted by the gas on the particle (Gupta et al., 1999), Figure 2.3. The criterions for the definition of the boundaries between the classes of powders are as follows:

$$\left(\rho_s - \rho_f\right) \cdot \frac{\pi \cdot d_p^3 g}{6F_e} = K_1 \qquad \text{transition from Group A to B} \qquad (2.3)$$

$$\left(\rho_s - \rho_f\right) \cdot \frac{d_p^3 g}{F_e} = K_2 \qquad \text{transition from Group C to A} \qquad (2.4)$$

$$\left(\rho_s - \rho_f\right) \cdot d_p g = K_3 \qquad \text{transition from Group B to D} \qquad (2.5)$$

According to Molerus, the constants K_i depend on the nature of the powder, and F_e represents the estimated cohesive force. Molerus was able to introduce an equation for the boundary between the Groups C and A.

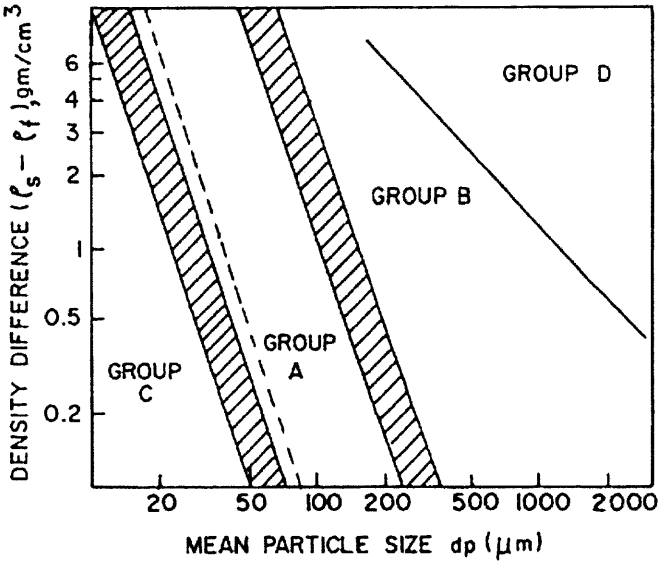

Figure 2.3 Powder classification of Geldart as modified by Molerus.

The most significant contribution by Clark et al. (1986) was to devise a method of representing the powders groups of Geldart by certain dimensionless numbers; this was useful for computer analysis, however, their equations are long and tedious (Gupta et al., 1999).

Nanoparticles may be initially considered as Class "C" powders, however, due to their different behavior during fluidization and the formation of agglomerates, some researchers have suggested that these powders should be classified into a new type. They have classified agglomerates of nanoparticles in two types which they called "Agglomerate Bubbling Fluidization" (ABF), Group "C" like behavior, and "Agglomerate Particulate Fluidization" (APF), Group "A" like (Wang et al., 2002).

The liquid-like behavior is a very important characteristic of the fluidization of particulates, as shown in Figure 2.4; once fluidized, the dense-phase which is the homogenous mixture of solid particles and the gas, shows the following characteristics: a horizontal surface, levels of different connected beds equalize, and the pressure drop is equal to the static head (Kunii et al., 1991). For example, a heavy object that would rest at the top of a static bed would sink in a fluidized bed; likewise a light object would tend to float. These properties indicate that a fluidized bed can be taken as a denser gas phase or a light liquid phase.

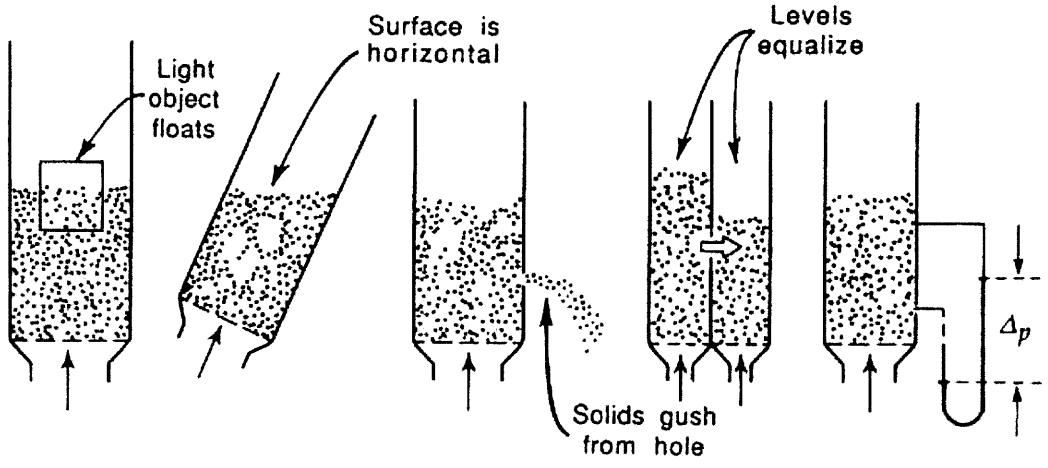

Figure 2.4 Fluid like behavior of fluidized particles (Kunii et al., 1991).

2.2 Parameters that Describe the Fluidization

2.2.1 Bed Pressure Drop

The bed pressure drop is a very important parameter in fluidization because it determines the work to be done by the fluid media to lift the dense phase, and an estimation of the power consumption can be made.

The most common criteria used to determine the pressure drop across a homogeneous bed of particles is the Ergun equation (Ergun, 1952); and it is related to the frictional pressure drop by the very well known equation:

$$\frac{\Delta p}{L_m} g_c = 150 \frac{(1-\varepsilon_m)^2}{\varepsilon_m^3} \frac{\mu u_o}{(\phi_s d_p)^2} + 1.75 \frac{1-\varepsilon_m}{\varepsilon_m^3} \frac{\rho_g u_o^2}{\phi_s d_p} \tag{2.6}$$

However, it is important to remind ourselves that this is an empirical equation and it was developed for an inertial frame, it also considered a fixed bed of particles and not a dynamic assembly of particles. This equation describes the almost linear relationship between the bed pressure drop and the fluid velocity until reaching fluidization conditions (pre-fluidization or fixed bed).

Once the bed of powder is fluidized, the drag force exerted on the particles by the fluid has to be equal to their weight over the cross-sectional area of the column. Therefore, the pressure drop across the bed of powder should follow the equation:

$$\frac{\Delta p}{L_{mf}} g_c = (1-\varepsilon_{mf})(\rho_s - \rho_g) \frac{g}{g_c} \tag{2.7}$$

It will be shown below that the Ergun equation for the pressure drop is not applicable at all, since for very fine particles the distribution of the gas is not even and the bed is not homogeneous. In the case of the agglomerates of nanoparticles, the stage before fluidization usually exhibits channeling and there are also many fluctuations in the pressure drop that cannot be explained at all with the Ergun model for the pressure drop.

2.2.2 Minimum Fluidization Velocity (U_{mf})

The minimum fluidization velocity (U_{mf}) is important because it determines the instant in which there is a homogeneous mixture between the solid particles and the fluid, in addition almost all the particles present a dynamic behavior (they are moving).

According to the literature (Gupta et al., 1991), there are many experimental methods that can lead to the determination of the U_{mf} such as the pressure drop method, voidage method and heat transfer method, as shown in Figure 2.5. Regarding the theoretical predictions of U_{mf}, the following methods are commonly used: dimensional analysis, drag force method, pressure drop method and terminal velocity method.

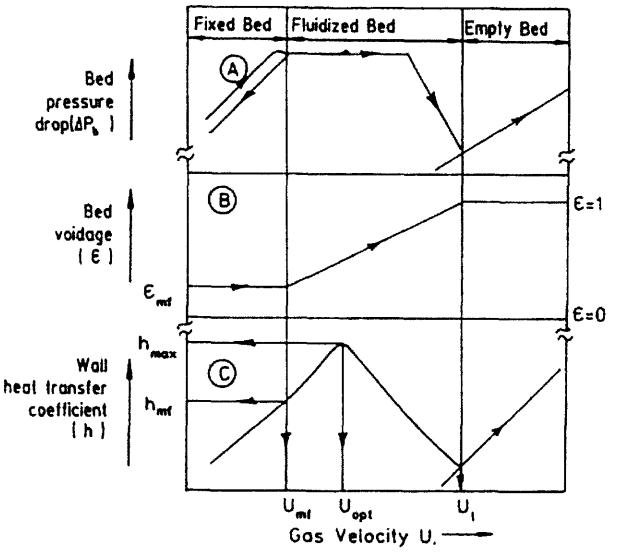

Figure 2.5 Various experimental methods to determine minimum fluidization velocity: (A) pressure drop, (B) bed voidage, and (C) heat transfer.

Following the theoretical pressure drop approximation, the equations for the pressure drop given above (Equations 2.6 and 2.7) should apply at the minimum fluidization velocity and the following quadratic expression results:

$$150\frac{(1-\varepsilon_m)^2}{\varepsilon_m^3}\frac{\mu u_o}{(\phi_s d_p)^2}+1.75\frac{1-\varepsilon_m}{\varepsilon_m^3}\frac{\rho_g u_o^2}{\phi_s d_p}=(1-\varepsilon_{mf})(\rho_s-\rho_g)\frac{g}{g_c} \tag{2.8}$$

This equation, after manipulation of the variables, can be simplified to:

$$\frac{1.75}{\varepsilon_m^3\phi_s}\mathrm{Re}_{p,mf}^2+150\frac{(1-\varepsilon_{mf})}{\varepsilon_m^3\phi_s^2}\mathrm{Re}_{p,mf}=\mathrm{Ar} \tag{2.9}$$

Where

$$\mathrm{Re}=\frac{d_p u_{mf}\rho_g}{\mu} \tag{2.10}$$

And

$$\mathrm{Ar} = \frac{d_p^3 \rho_g \left(\rho_s - \rho_g\right) g}{\mu^2} \tag{2.11}$$

Simplifications of the equation of the minimum fluidization velocity based on the size of the particles can be made (Kunii et al. 1991). For very small particles at $\mathrm{Re}_{p,mf} < 20$,

$$u_{mf} = \frac{d_p^2 \left(\rho_s - \rho_g\right) g}{150\mu} \frac{\varepsilon_{mf}^3 \phi_s^2}{1-\varepsilon_{mf}} \tag{2.12}$$

It can be seen that the equation to find the minimum fluidization velocity is of quadratic form with respect to the Re number

$$K_1 \mathrm{Re}_{p,mf}^2 + K_2 \mathrm{Re}_{p,mf} = Ar \tag{2.13}$$

and the coefficients of this quadratic expression have been found constant for certain ranges; in the case of small particles, it can be presented in the form as indicated by Wen and Yu (1966) and recalled in Kunii-Levenspiel (1991). Therefore, this equation can be transformed into the following expression as proposed by Wen and Yu (1966) for fine particles.

$$\mathrm{Re}_{p,mf} = \left[(33.7)^2 + 0.0408 Ar\right]^{1/2} - 33.7 \tag{2.14}$$

Figure 2.6 shows a typical plot of the experimental data showing the traditional form in which U_{mf} is defined and the plateau region that the value of the bed pressure drop reaches once the bed is fully fluidized.

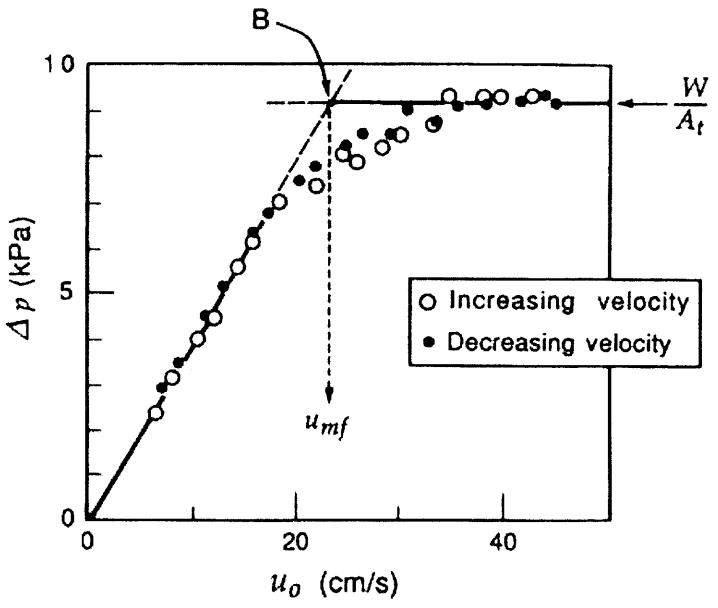

Figure 2.6 Formal definition of U_{mf} and the bed pressure drop (Kunii et al., 1991).

In the same way, Figure 2.7 shows the behavior of three different classes of powders. The experimental bed pressure drop response and bed expansion for each class of powder are different.

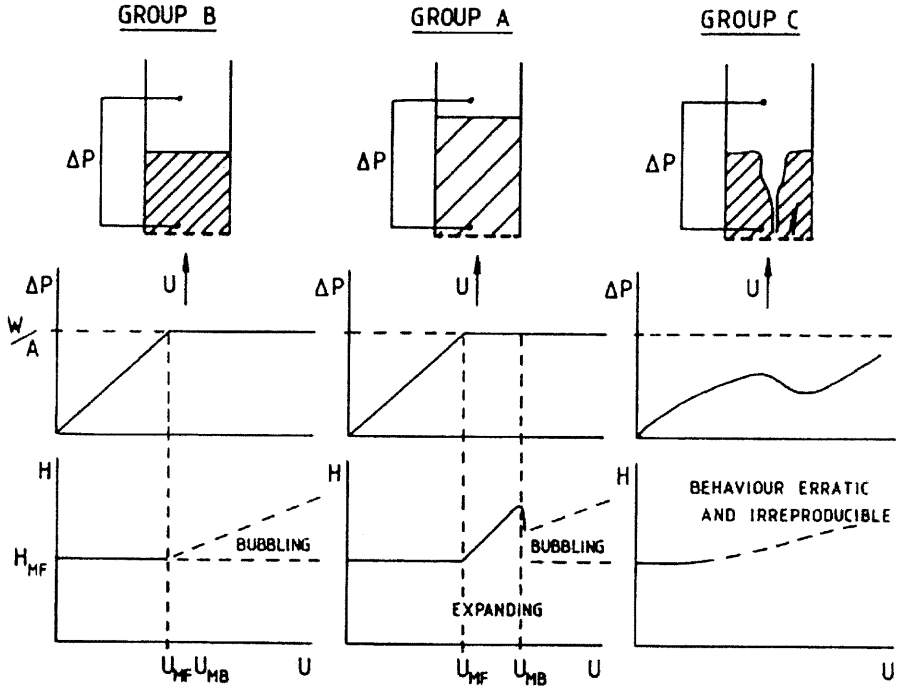

Figure 2.7 Typical fluidization behaviors of powders class B, A and C (Kunii et al, 1991).

2.2.3 Terminal Velocity

The terminal velocity is important because it establish the maximum allowable fluid velocity for the operation or the minimum velocity for carryover of the particles (Gupta et al., 1999). Applying Newton's second law, the following equations can be written:

$$V_p \rho_p \frac{dU_p}{dt} = -\left(F_{drag} + F_{buoyance}\right) + F_{gravity} \tag{2.15}$$

At conditions of terminal velocity, $\frac{dU_p}{dt} = 0$

then the equation for the terminal velocity is given by:

$$u_t = \left[\frac{4d_p(\rho_s - \rho_g)g}{3\rho_g C_D} \right]^{1/2} \tag{2.16}$$

where C_D is the drag coefficient which for spherical particles can be found using the following expression:

$$C_D = \frac{24}{\mathrm{Re}_P} + 3.3643\,\mathrm{Re}_P^{0.3471} + \frac{0.4607\,\mathrm{Re}_P}{\mathrm{Re}_P + 2682.5} \tag{2.17}$$

as proposed by Haider and Levenspiel (1989).

However, there are many correlations for the drag coefficient depending on the range of the Reynolds number and the shape of the particles; the large number of correlations are based on the conditions at which the terminal velocity is being estimated; there are differences in the terminal velocity between spherical particles settling in an infinite medium as compared to non spherical particles, and if they are settling in an assembly of particles were collisions can occur.

The experimental methods used for finding the terminal velocity are the same ones for measuring the minimum fluidization velocity (U_{mf}) except for the selection of the point at which the values of bed pressure drop and fluid velocity are considered.

The most common method for finding the terminal velocity from experimental data is by extrapolation of the bed expansion represented by the bed voidage. Nevertheless, special attention should be taken when applying these criteria to fine particles since it can overestimate the value of the terminal velocity (Gupta et al., 1999).

2.2.4 Importance of the Empty Bed Voidage

The empty bed voidage (ε) is a very important variable in fluidization, since the empty bed voidage is present in all the equations that model fluidization. For example, it is used for determining the local average axial velocities of fluid and particles.

Let introduce V_f and V_s as the volumetric flow rates of the fluid and the solid particles respectively. Taking into account the bed empty voidage, the local velocities of fluid and particles can be found by the following equations:

$$u = \frac{V_f}{\varepsilon}, \qquad v = \frac{V_s}{1-\varepsilon}. \tag{2.18}$$

As mentioned before, during bed expansion there is a drag force (f) exerted by the fluid on the particles and it is expected to be proportional to $u - v$ with a proportionality factor β that is an increasing function of ε:

$$f = \beta(\varepsilon)\left[\frac{V_f}{\varepsilon} - \frac{V_s}{1-\varepsilon}\right]. \tag{2.19}$$

One important contribution to fluidization theory was made by Richardson & Zaki (1954); they assigned an empirical expression to the proportionality factor β as shown below:

$$\beta(\varepsilon) = \frac{\rho_s(1-\varepsilon)g}{v_t\varepsilon^n}, \tag{2.20}$$

where ρ_s is the density of the solid material, v_t is the terminal velocity and n is the so called Richardson & Zaki index which depends on the Reynolds number of the particle (Jackson, 2000).

A force balance on the particles per unit volume of the suspension gives

$$\frac{\overline{V}_f / v_t}{\varepsilon} - \frac{\overline{V}_s / v_t}{1-\varepsilon} = \varepsilon^n . \tag{2.21}$$

A corresponding force balance on the gas shows that its pressure gradient must support the weight of the suspended particles, so

$$\frac{dp}{dz} = -\rho_s (1-\varepsilon) g , \tag{2.22}$$

For analysis purposes, Equation 2.21 can be presented as follows

$$\frac{\overline{V}_f / v_t}{(1-\phi)} - \frac{\overline{V}_s / v_t}{\phi} = (1-\phi)^n , \tag{2.23}$$

in this equation ϕ represents the fraction of the total volume occupied by the particles; moreover, this expression can be manipulated to get

$$\frac{\overline{V}_f}{v_t} = \frac{(1-\phi)}{\phi}\frac{\overline{V}_s}{v_t} + (1-\phi)^{n+1} . \tag{2.24}$$

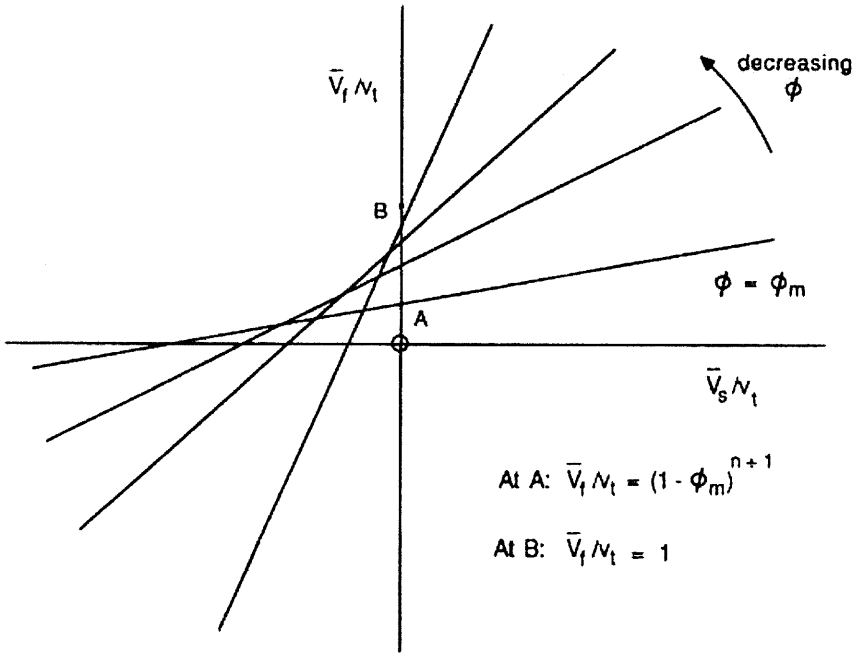

Figure 2.8 Contours of constant ϕ in the plane of $\bar{V}_s/v_t$ and $\bar{V}_f/v_t$. (Jackson, 1993).

Figure 2.8 is a result of Equation 2.24, and it shows the contours of the volume fraction of the particles into the first, second and third quadrants, where they represent concurrent upflow, countercurrent flow and concurrent downflow respectively. The fourth quadrant lacks physical meaning since in that region the particles will move up with a downward flow of fluid. In Figure 2.8, the line between the intercepts A and B represents fluidized beds in which the overall velocity of the solid particles is zero. Nevertheless, this does not mean that the solid particles are static inside of the fluidized bed, but that the mass velocity of the solid particles upward is equal to the mass velocity of the solid particles downward (Jackson, 2000).

According to Equation 2.22, the pressure drop is proportional to the void fraction and therefore the volume fraction of the particles; a set of curves that relate the pressure gradient (equivalent to the volume fraction) to the gas flow rate, for different fixed values of the particles flow rate can be represented by the Zenz diagram shown in Figure 2.9 (Jackson, 2000).

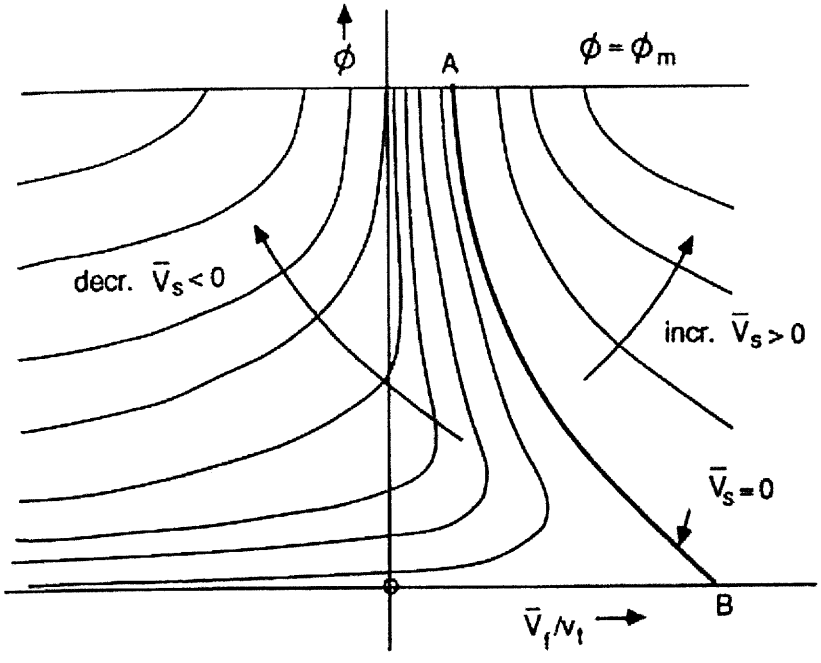

Figure 2.9 Zenz diagram corresponding to Figure 2.8.

Again, the line between the points A and B correspond to fluidized beds; contour lines at flow of particulates larger than zero $V_S > 0$ represent conveying of solids , so called "elutriation" of particles, and contour lines at flow of particles less than zero $V_S < 0$ represent sedimentation of solids, so called "collapse" of the fluidized bed.

The contour line between the points A and B occurs when $V_S = 0$, if this value is replaced in Equation 2.24 then the following equation results

$$\frac{\overline{V}_f}{v_t} = (1-\phi)^{n+1} = \varepsilon^{n+1}, \tag{2.25}$$

Equation 2.25 can be expressed in logarithmic form in order to have a linear relationship to make it easy to find the exponent "n" as shown below

$$\log\left(\frac{\overline{V}_f}{v_t}\right) = (\text{n+1})\ \log(1-\phi) = (n+1)\log(\varepsilon). \tag{2.26}$$

Another form to express this equation is by expanding the term in the left side as shown below,

$$\log(\overline{V}_f) = (\text{n+1})\ \log(1-\phi) + \log(v_t) = (n+1)\log(\varepsilon) + \log(v_t). \tag{2.27}$$

It will be shown in Chapter 3, that for fluidization of agglomerates of nanoparticles, Equation 2.27 is frequently used to find the values of "*n*" (Richardson & Zaki index) and "v_t" (terminal velocity). In addition, Figure 2.9 shows the changes in the slopes of the different curves at different solids velocities and that an increase in the slope of the experimental data plotted (Equation 2.27) means that the particles start to be carried out by the flow, in other words, elutriation is present. This can be more clearly seen in Figure 2.10 which is the same as Figure 2.9 except for changing the variable from the volume fraction of solids (ϕ) to the bed empty voidage (ε) and rotated in a way that the gas velocity appears as the ordinate.

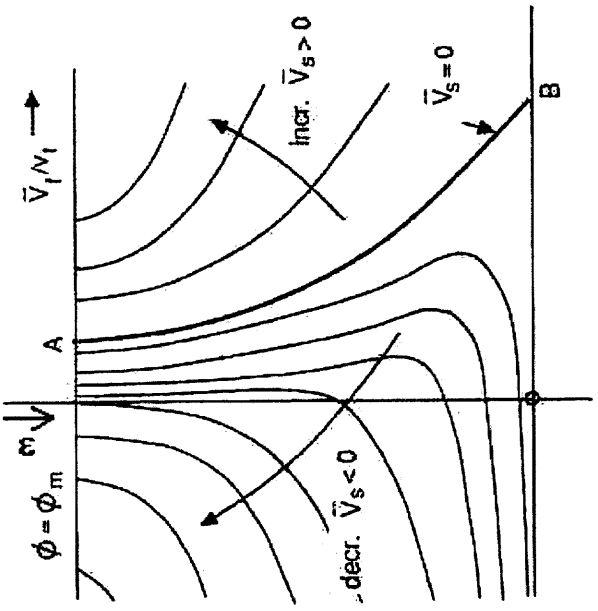

Figure 2.10 Zenz diagram corresponding to Figure 2.9, but rotated and as a function of the bed voidage instead of the solid volume fraction.

The experiments carried out by Richardson & Zaki gave information about the sedimentation velocity v_s of a dispersion of particles in liquid and their relationship with the concentration, measured by ε. They came up with the following empirical relation for a suspension of uniform, spherical particles, infinite in extent:

$$v_s = v_t \varepsilon^n , \tag{2.28}$$

with

$$n = \begin{cases} 4.65 & \text{for } Re_t < 0.2 \\ 4.35\ Re_t^{-0.03} & \text{for } 0.2 < Re_t < 1 \\ 4.45\ Re_t^{-0.1} & \text{for } 1 < Re_t < 500 \\ 2.39 & \text{for } 500 < Re_t \end{cases} \tag{2.29}$$

where

$$\mathrm{Re}_t = \frac{d_p \rho_f v_t}{\mu}, \tag{2.30}$$

the Reynolds number for an isolated particle falling at its terminal velocity in the fluid.

It is important to note that there are at least two kinds of empty voidage (Gupta et al., 1999). The following equation correlates the bulk density (or density during fluidization) and the true density,

$$\frac{\rho_b}{\rho_t} = (1-\varepsilon_I)(1-\varepsilon). \tag{2.31}$$

where the intraparticle voidage, ε_I, corresponds to the empty spaces inside the agglomerates of nanoparticles and it is almost invariable during fluidization; while the interparticle voidage ε, is related to the voids between agglomerates and depends on the fluid flow during fluidization.

This chapter has covered the main principles on which the present work relies in explaining diverse phenomena in conventional fluidization experiments. Chapters 3 and 4 will make reference to some of the equations and/or figures shown in this chapter. However, this chapter could not cover the many aspects of the theory already developed for fluidization, new concepts such as the involvement of the Stokes number in the modeling has been already mentioned (Jackson, 2000); this concept is important for dense phase fluidized beds and would help to explain the effect of recirculation of solid particles and the dynamics of the bed.

CHAPTER 3

CONVENTIONAL FLUIDIZATION OF AGGLOMERATES OF NANOPARTICLES

3.1 Introduction

This type of fluidization takes place when the powder, composed of many agglomerates of nanoparticles, and the fluid gas interact inside the column in the absence of any kind of force field but gravitational. It has been mentioned before that agglomerates of nanoparticles have very low density, therefore, the gas velocity for their fluidization is expected to be very low compared to micron size particles. Conventional fluidization takes place in a vertical fluidization column which will be described in the experimental section.

During the experiments, it was observed that some of the powders expanded very uniformly about several times the initial bed height; for this homogeneous fluidization to occur, it was very important to have a homogenous gas field and to separate agglomerates larger than 500 um from the bed of particles.

Among the new findings, it will be shown that there are fluctuations in variables related to fluidization, such as bed pressure drop and bed height, before reaching the minimum fluidization velocity, and that some powders present an exponential bed expansion which follows the Richardson & Zaki model.

3.2 Experimental Set-Up

An acrylic pipe of 2.25" I.D. was used as a column; in its bottom, a 100 um or 20 um porous sintered metal plate was placed and used as a gas distributor. Before the distributor, a packed bed of spherical glass beads (particle diameter of about 2 mm) was placed in order to make the gas fluid flow uniform even before reaching the distributor. The length of the column was of about 6 feet, and in the top, a filter was located to trap any elutriated particles.

The gas flow was either dry nitrogen or bone dry air measured by an area variable or a differential pressure flowmeter depending on the range. The differential pressure flowmeter was used for ranges under 1 l/min, while the area variable was used for ranges under 4 l/min. The pressure drop across the bed was measured using a high accuracy differential pressure transmitter which allowed us to measure even mils of inches of water with a range of 0 -1" H_2O. A diagram of the apparatus is shown in Figure 3.1.

All the gas connections were sealed with clear silicon to avoid leaks, since the gas flow used in the experiments was so low that a small leak could distort the results. Additional experiments were done in a 0.75" I.D. column.

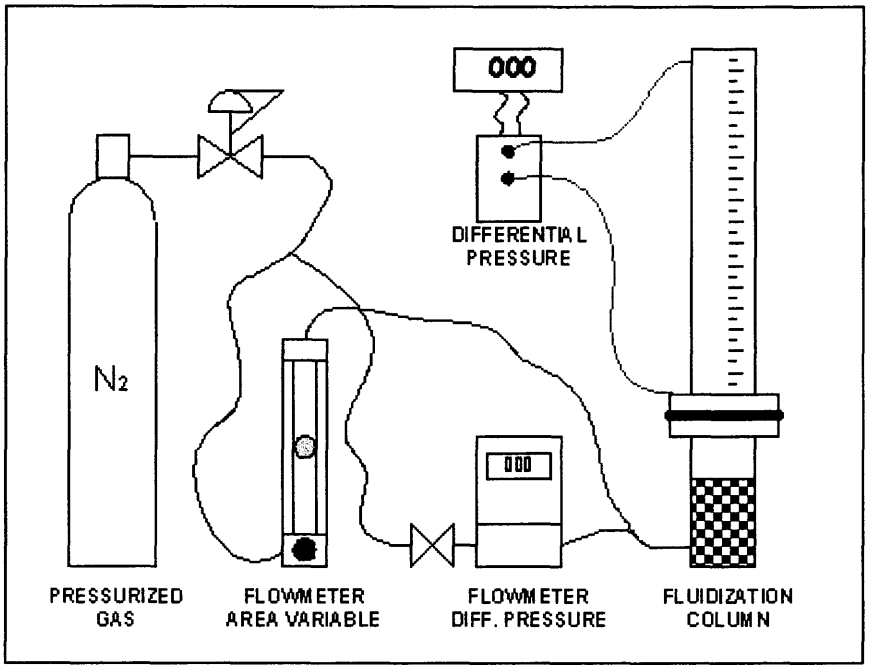

Figure 3.1 Schematic of the fluidization set-up for nanoagglomerates.

3.3 Procedure

The agglomerates of nanoparticles were sieved in order to obtain only particles under 500 um, since it was found that large agglomerates break the homogeneity of the gas flow field required for a smooth fluidization. After sieving a certain amount of powder was weighed; experiments were done with 5, 10 and 20 grams of powder. The weight of the powder was changed, to find out if it affected the behavior of the fluidization. After the powder was loaded into the column, the gas flow was increased progressively. At the beginning, due to the strong cohesive forces, the powder formed a plug, then it was broken by tapping the bed. Once the powder became loose, channeling occurred, and circulation of the dense phase began.

Bed pressure drop and bed height oscillated when the gas velocity was below the minimum fluidization velocity. At larger flow rates the plateau of the bed pressure drop was reached and fluctuations no longer occur. Bed expansion began as soon as the gas flow started to circulate through the bed but it oscillated which means that the density in the bed was not homogeneous. Flow rates higher than the minimum fluidization velocity the bed height increased at a larger rate and oscillations did not occur. The large bed expansion of about five times the initial bed height without flow is a very important characteristic since no other class of powder behaves in this way (large bed expansion before minimum fluidization conditions). The gas flow was stopped when bubbling began and elutriation was significant.

3.4 Results

Typical results of the fluidization experiments are plots of bed pressure drop vs. gas velocity. As mentioned in Chapter 2, the minimum fluidization velocity (U_{mf}) is found when the bed pressure drop reaches the plateau region (see Figure 2.6); however, there are fluctuations in the bed pressure drop and bed height before the U_{mf}. These fluctuations are not noticeable when using a water manometer for measuring the bed pressure drop since its sensitivity is too low.

Figures 3.2, 3.3 and 3.4 are plots for 5, 10 and 20 grams of Aerosil® R974, respectively, in a 2.25 inch I.D. column. At gas velocities less than 0.4 cm/s there are many fluctuations in the bed pressure drop and bed height readings; in addition, some of the values of the bed pressure drop match the plateau value

even before the minimum fluidization velocity is reached. These unstable high values of bed pressure drop before full fluidization may lead to an incorrect determination of the U_{mf}. For example, if we assume that the bed pressure drop plateau region begins at these unstable points the U_{mf} would be about 0.2 cm/s for Aerosil® R974, rather than 0.4 cm/s.

As mentioned before, fluidization experiments were carried out using different amounts of agglomerates of nanoparticles. It is clear that the value of U_{mf} is independent of the amount of powder used to fluidize; however, the bed expansion is proportional to the initial bed height in all cases. However, the nondimensional bed height, which is the ratio of the actual bed height divided by the initial bed height at no flow, is almost independent of the amount of fluidized powder.

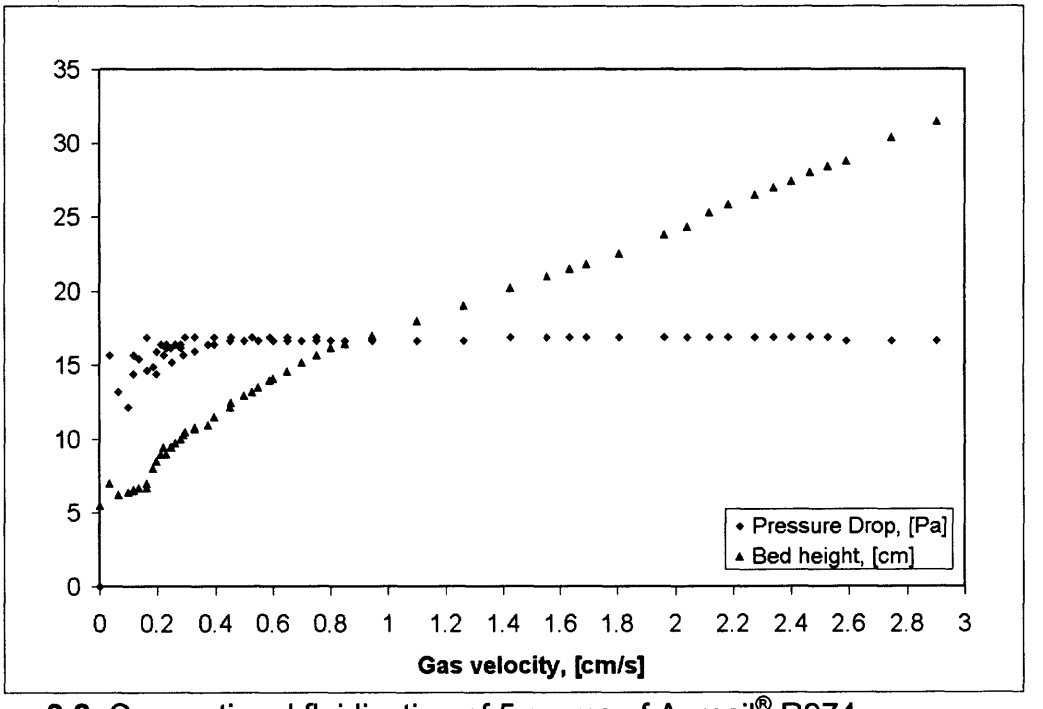

Figure 3.2 Conventional fluidization of 5 grams of Aerosil® R974.

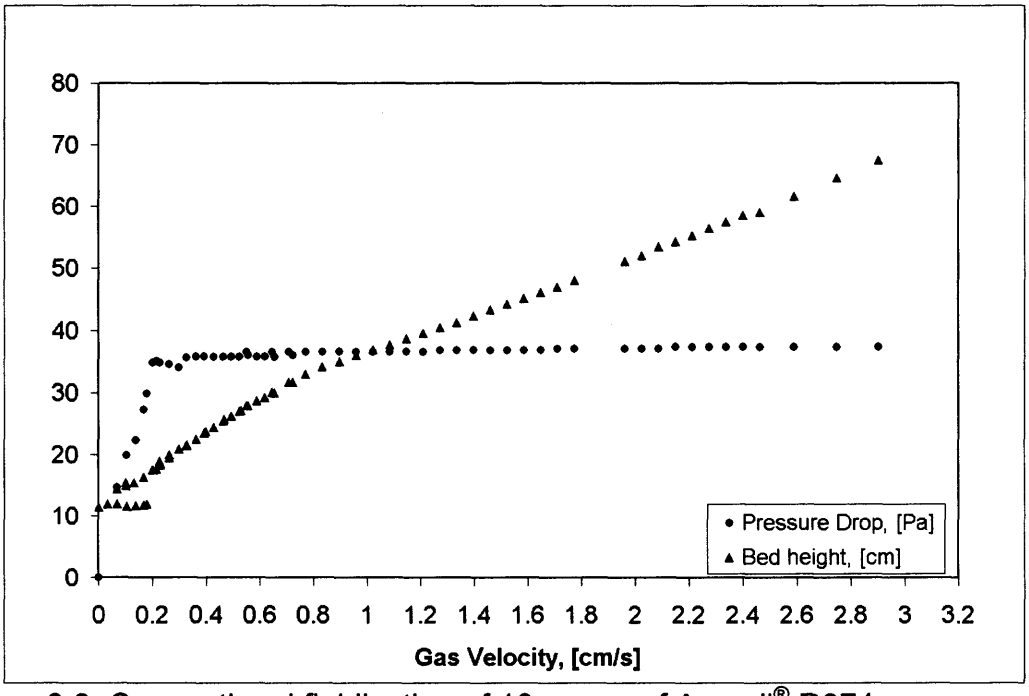

Figure 3.3 Conventional fluidization of 10 grams of Aerosil® R974.

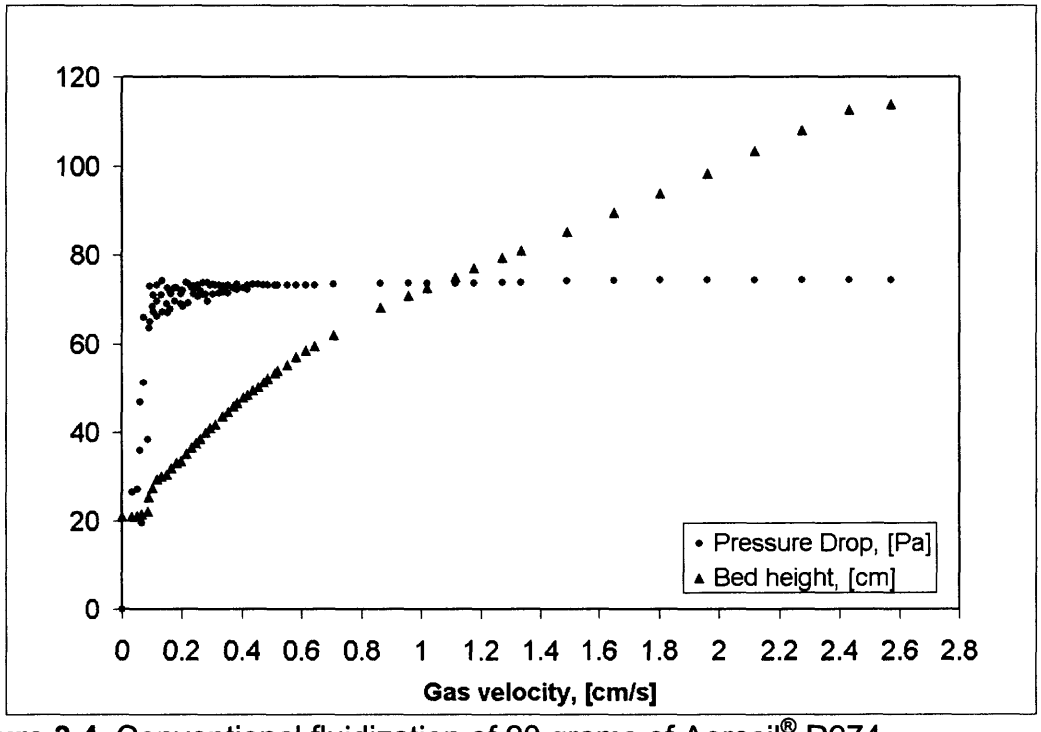

Figure 3.4 Conventional fluidization of 20 grams of Aerosil® R974.

Since there are fluctuations in the bed pressure drop in the region close to the U_{mf}, it can be inferred that the fluidization is not fully developed in the entire bed; moreover, these fluctuations show up when either fluidizing or de-fluidizing the bed (increasing or decreasing the gas velocity). Figure 3.5 shows that the fluctuations disappear when the gas velocity is around 0.4 cm/s or more, for Aerosil R974, and that they increase at gas velocities below that value.

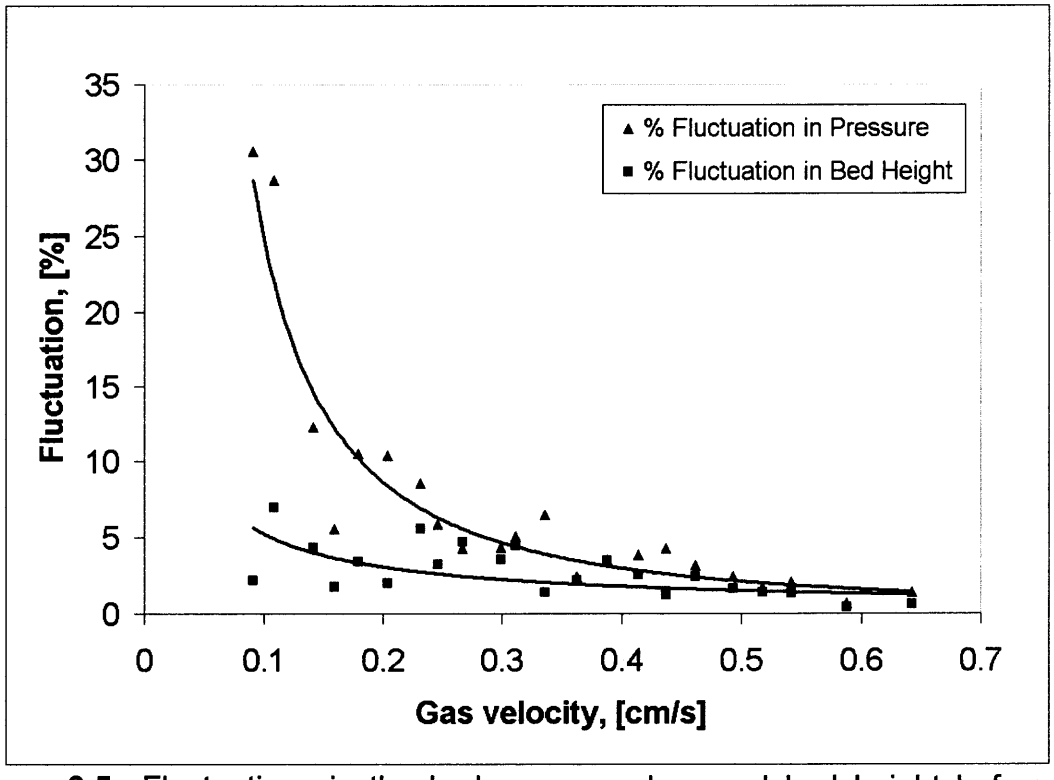

Figure 3.5 Fluctuations in the bed pressure drop and bed height before full fluidization.

Due to these fluctuations, the value calculated for the U_{mf} by using the pressure drop approach became uncertain because of the instabilities of the bed. Thus, it is necessary to find a procedure to confirm the value of the minimum fluidization velocity.

As mentioned in Chapter 2, there are different methods for finding the U_{mf}, such as bed voidage or heat transfer based methods. Since the bed expansion is proportional to the bed voidage fraction, a tendency was sought to relate bed expansion and gas velocities in a way that the U_{mf} could be found by the empty voidage method. Hence, a plot of the fluidized bed height vs. the logarithm of the gas velocity is introduced as shown in Figure 3.6; clearly, a linear tendency can be seen. This relationship between the bed expansion and the logarithm of gas velocity may mean that an increase in the bed voidage due to an increase in the gas flow is homogeneous throughout the bed of agglomerates. Moreover, it can be noticed that this linearity can be used to confirm the value of the U_{mf} when the bed of particles is fully fluidized and stable. These plots may also be useful to identify the gas velocity range in which elutriation becomes significant. According to Figure 3.6, the U_{mf} for Aerosil® R974 is around 0.35 cm/s (-0.45 logarithm scale) and the U_{mb} is around 1.3 cm/s (0.15 logarithm scale).

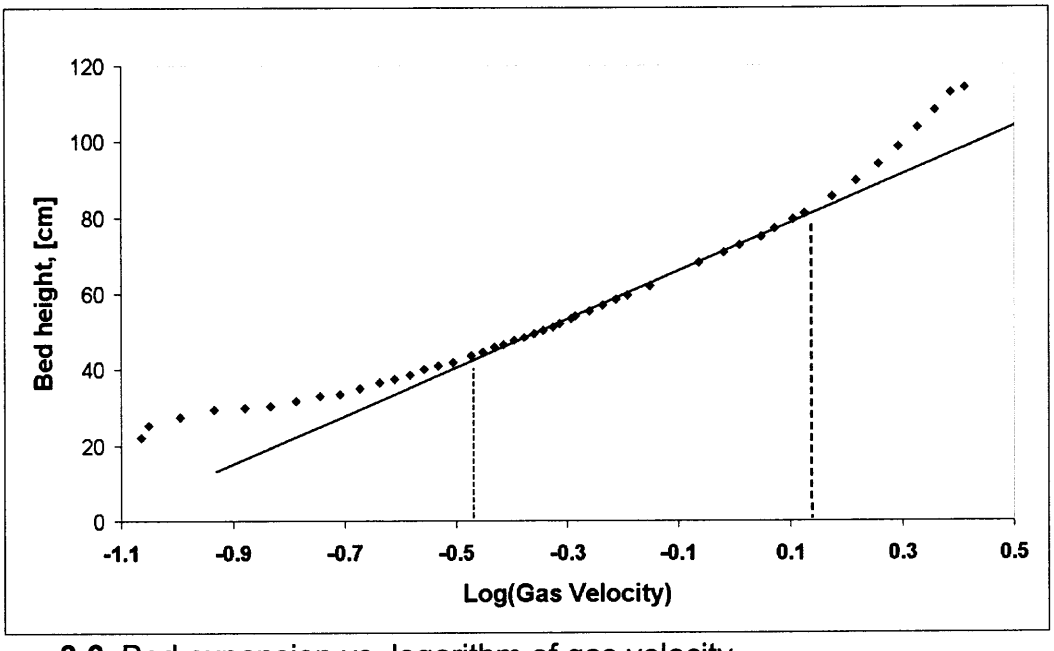

Figure 3.6 Bed expansion vs. logarithm of gas velocity.

The bed height can be made non-dimensional by dividing it by the initial bed height at no flow. After running experiments with three different amounts of agglomerates of Aerosil® R974 and measuring bed expansion, Figure 3.7 was obtained. The linear correlation found in Figure 3.7 (Equation 3.1) can be applied for any amount of powder, and can be used for predicting the bed expansion in the range of our experiments, where the coefficients "a" and "b" were found according to a linear regression.

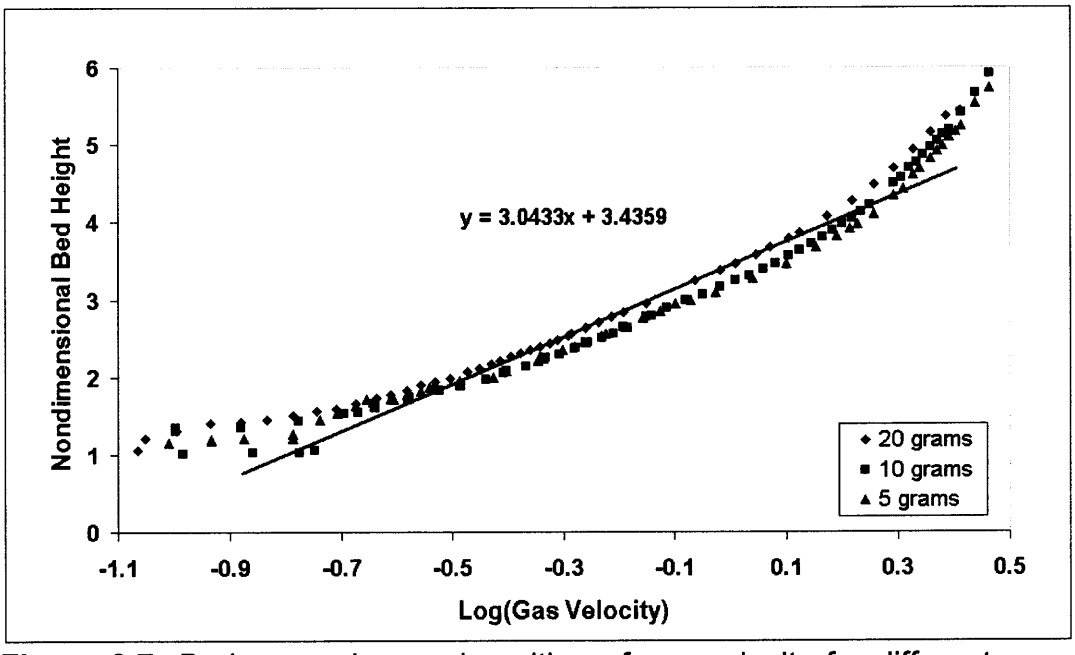

Figure 3.7 Bed expansion vs. logarithm of gas velocity for different amount of agglomerates.

$$\frac{H}{H_0} = a \cdot \log(U) + \log(b) \qquad U_{mf} < U < U_{mb} \tag{3.1}$$

Figures 3.8, 3.9 and 3.10 show the Richardson & Zaki plots for the fluidization of three different amounts of agglomerates of Aerosil® R974. The data can be fitted by two linear approximations. These results are not clearly

understood yet, but they may mean that either there is a change in the size of the agglomerates of nanoparticles at different gas velocities during fluidization or elutriation/conveying of particles increases the bed voidage at a higher rate than in smooth fluidization which is explained by the Zenz diagrams (Figure 2.10, Chapter 2). In these, the average velocity of the agglomerates is zero during fluidization, but an increment on the velocity of the solids is reflected by an increase on the rate of change of the fluid velocity against the empty bed voidage.

For these plots, the empty voidage was calculated by Equation (3.2) using the experimental bed pressure drop (ΔP) and the bed expansion (H). The agglomerate density was found by using Equation (3.3).

$$\frac{\Delta P}{H} = (1-\varepsilon)(\rho_a - \rho_g)g \tag{3.2}$$

$$\rho_a = \frac{W_{bed}}{V_0} = \frac{W_{bed}}{H_0 A_t} \tag{3.3}$$

The slope of the linear regression at low gas velocities can be explained by the criteria of Richardson & Zaki. These plots give straight lines in which the slope is the index *"n"* and the *constant coefficient* is the terminal velocity of the agglomerate; therefore, its size can be estimated using the terminal velocity equation. However, this method overestimates the size of the agglomerates since it is based on the extrapolation of the empty voidage fraction to unity, a condition that works for the largest agglomerate but for the average one (Lewis et al., 1949).

In addition, the Richardson & Zaki criteria can be applied only to a fully fluidized bed of nanoparticles. At gas velocities lower than U_{mf}, the data scatter and clearly fall out of the linear regression.

The very well known correlation for these plots follows Equation 3.4

$$\log(U) = n\log(\varepsilon) + \log(U_t), \tag{3.4}$$

where *"n"* is the Richardson & Zaki index, ε is the bed voidage, U is the gas velocity and U_i is the average terminal velocity. From the values of the terminal velocities, the agglomerate sizes can be calculated.

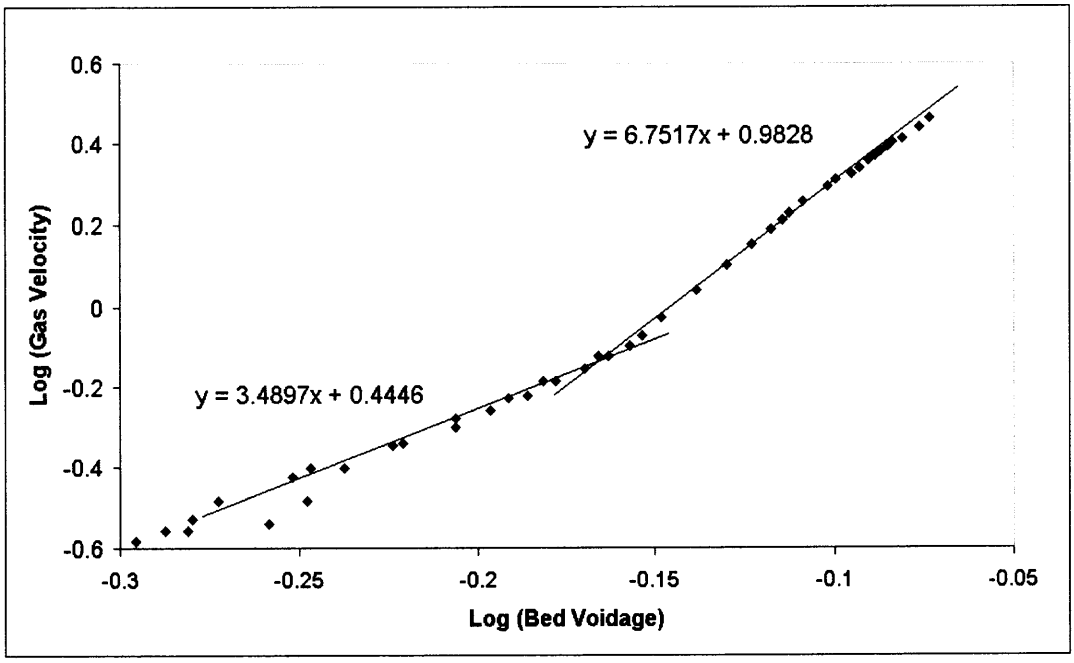

Figure 3.8 Richardson & Zaki plot for the fluidization of 5 grams of R974.

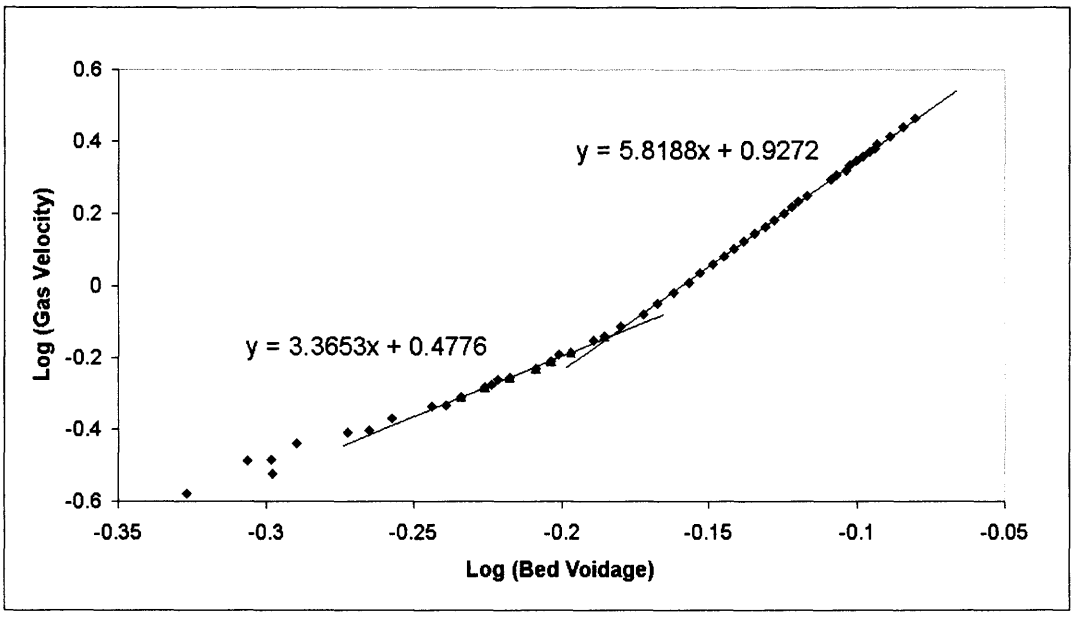

Figure 3.9 Richardson & Zaki plot for the fluidization of 10 grams of R974.

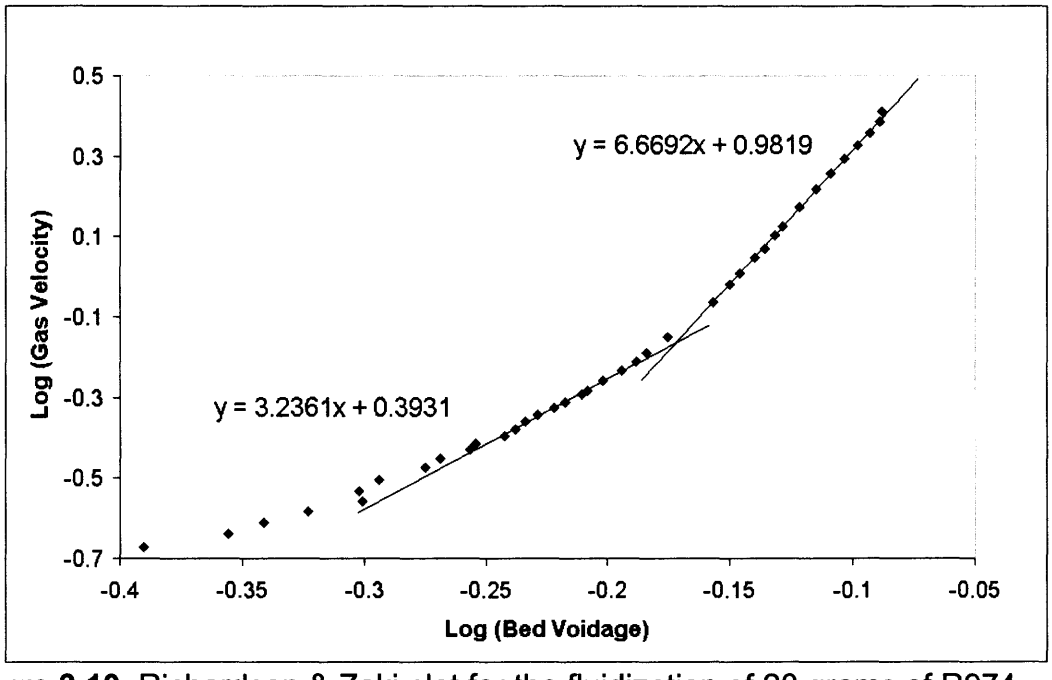

Figure 3.10 Richardson & Zaki plot for the fluidization of 20 grams of R974.

Table 3.1 Richardson & Zaki Data of Fluidization of Aerosil® R974.

	Fluidization of R974			
	First Slope		Second Slope	
	n	Log(Ut)	n	Log(Ut)
5 grams	3.6264	0.476	6.7517	0.9828
10 grams	3.3653	0.4776	5.8188	0.9272
20 grams	3.2361	0.3931	6.6691	0.9819
Average	**3.41**	**0.45**	**6.41**	**0.96**
Stand. Dev.	0.20	0.05	0.52	0.03
% Error	6.14	12.29	7.74	3.24

By assuming a creeping flow around a spherical particle ($Re_t < 0.1$), in which Stokes' law applies, a preliminary estimation of the agglomerate size can be done by using the values of terminal velocities of Table 3.1 and the following equation (Seville et al., 1997):

$$U_t = \frac{d_p^2(\rho_p - \rho_g)g}{18\mu} \quad \Leftrightarrow \quad d_p = \sqrt{\frac{18U_t \cdot \mu}{(\rho_p - \rho_g)g}}; \tag{3.5}$$

which after substitution of appropriate values gave us the approximate agglomerate sizes, 160 um for the first slope (U_t = 2.8 cm/s) and 285 um for the second slope (U_t = 9.12 cm/s). These approximated agglomerate diameters were used to calculate the Reynolds number as follows

$$\mathrm{Re}_t = \frac{(0.00016)(1.229)(0.028)}{0.0000175} = 0.3203, \tag{3.6}$$

$$\mathrm{Re}_t = \frac{(0.000285)(1.229)(0.0912)}{0.0000175} = 1.84648. \tag{3.7}$$

The Reynolds number obtained by Equation (3.6) corresponds to low flow conditions and the first slope of the Richardson & Zaki plots while the one obtained in Equation (3.7) corresponds to high flow conditions and the second slope of the plots. These results imply that the flow regime is in the intermediate range between the creeping flow and Newton's law, say $0.1 < Re_t < 750$, for which there is no explicit equation for the terminal velocity; and it is necessary to use an equation based on a drag coefficient correlation.

Thus, the average diameter of the agglomerates was calculated by using an equation that relates the terminal velocity for a single spherical particle (Gupta et al., 1999):

$$\mathrm{Re}_t = \left[\frac{4}{3}\cdot\frac{Ar}{a}\right]^{1/(2-b)}, \tag{3.8}$$

where

$$\mathrm{Re}_t = \frac{d_p \rho_f U_t}{\mu}, \quad Ar = \frac{d_p^3 \rho_g \left(\rho_s - \rho_g\right) g}{\mu_g^2}. \tag{3.9}$$

The values of the coefficients "a" and "b" in Equation (3.8) depend on the flow regime as shown in the table below and they relate the Reynolds number to the drag coefficient for three different flow regimes (Gupta et al., 1999).

Table 3.2 Constants for Evaluating Drag Coefficient for Three Flow Regimes.

Range	**a**	**b**	**Range $(Ar)^{1/8}=K$**
Re < 2, Stokes	24	1	<3.3
2 < Re < 500, intermediate	18.5	0.6	3.3 - 48.6
500 < Re < 200000, Newton	0.44	0	43.6 – 2360

Source: Gupta et al. (1999). Generalities and Basics of Fluidization.

Agglomerates of nanoparticles are not spherical and are surrounded by other agglomerates in the fluidized bed. Therefore a drag coefficient correlation that considers porous non spherical particles and multiparticle effects should be more suitable; however, such a more general correlation is not available. Nevertheless, there are some correlations for the drag coefficient based on the Reynolds number, the sphericity, permeability, volume fraction, and density of the particles and for comparison purposes the following correlation was used (Clift et al., 1978.)

$$W = \log_{10} \mathrm{Re} \tag{3.10}$$

$$\log\left[\left(C_D \,\mathrm{Re}/24\right) - 1\right] = -0.881 + 0.82W - 0.05W^2 \qquad 1 < \mathrm{Re} \le 20 \tag{3.11}$$

$$\mathrm{Re}_t = \sqrt{\frac{4}{3}\frac{Ar}{C_D}} \tag{3.12}$$

The diameter of the particles can be calculated by using either Equations 3.8 or 3.12 in an iterative procedure, having the initial values of the agglomerate sizes estimated by Equation 3.5; in which, the density of the agglomerate is estimated from the mass of powder divided by the volume occupied by the bed at no flow as shown in Equation (3.3) and this value can change slightly due to bed aeration. A typical value for the agglomerate density of Aerosil® R974 is about 0.27 to 0.34 kg/m^3.

Table 3.3 Estimations of the Agglomerate Diameter by the Terminal Velocity.

Agglomerate density (kg/m^3)	Diameter of agglomerate in microns			
	First Slope (low flow)		Second Slope (higher flow)	
	Equation 3.8	Equation 3.12	Equation 3.8	Equation 3.12
27	186.4	191.8	335.3	377.5
28	182.9	188.1	329	370.5
29	179.6	184.6	323	362.8
30	176.4	181.3	317	355.8
31	173.4	178.2	312	349.5
32	170.6	175.2	305	343
33	167.9	172.3	302	337
34	165.3	169.6	297	331.5

Finally, the Reynolds numbers that resulted from the iterative process by which Table 3.3 was obtained, for an agglomerate density of 30 kg/m^3, are shown below for each of the slopes considered on Table 3.1.

First slope: $$\mathrm{Re}_t = \frac{(0.0001813)(1.229)(0.028)}{0.0000175} = 0.3629, \tag{3.13}$$

Second slope: $$\mathrm{Re}_t = \frac{(0.000355.8)(1.229)(0.0912)}{0.0000175} = 2.305. \tag{3.14}$$

Once again, these results confirm that the flow regime around the agglomerates is intermediate, between the Stokes (creeping flow) and Newton flow regimes.

3.5 Discussion

Certainly, it is very difficult to apply the Ergun equation mentioned in Chapter 2 to the fluidization of nanoparticles for the region before full fluidization is obtained; since this equation was empirically designed for a packed bed of spherical large particles, where the gas flows uniformly through all the empty spaces of the bed. This does not occur in the fluidization of agglomerates of nanoparticles since,

before full fluidization, the gas flow is not uniform through the entire bed and it forms channels as shown in Figure 3.11.

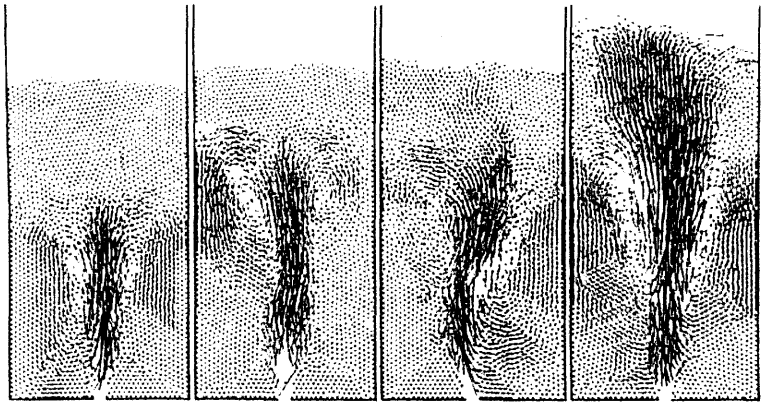

Figure 3.11 Simulation of a fluidized bed in its early stages (Seville et al., 1997).

For example, when the gas velocity in the column is 0.4 cm/s (value close to the U_{mf} of R974), the empty voidage calculated from the experimental data and Equation 3.2 is 0.56 and taking into account the Richardson & Zaki index from Figure 3.10 (n= 3.2) the terminal velocity of the agglomerates can be calculated as follows:

$$\frac{U_{mf}}{U_t} = \varepsilon_{mf}^{n} \quad \Leftrightarrow \quad \frac{0.4}{U_t} = 0.56^{3.2361} \quad \Leftrightarrow \quad U_t = 2.61\,\text{cm/s} \tag{3.15}$$

In the same context, since the gas velocity value of 0.4 cm/s considers the full cross section area of the fluidization column (25.7 cm^2 for a 2.25 inch I.D. column), the volumetric flow rate is about 10.3 cm^3/s. However, the effective cross section area, considering the agglomerates inside of the column, can be approximated by multiplying the full cross section area by the void fraction, resulting in a reduced area of about 14.46 cm^2; since the volumetric flow rate

found (10.3 cm^3/s) is constant through the column, the interstitial velocity of the fluid gas becomes 0.7 cm/s. In some cases the relative gas velocity respect to the agglomerate can be even larger depending on its velocity in the fluidized bed.

Moreover, during channeling the gas velocity in the channel may become as high as 81.7 cm/s, assuming a channel diameter of about 4 mm. If the Reynolds number is calculated inside the channel, a value of Re = 90 is obtained, this condition can still be considered laminar flow (Hagen - Poiseuille type); therefore, the shear stress can be calculated according to the formula:

$$\tau_{rz} = \frac{(P_O - P_L)}{2L_C} R \tag{3.16}$$

Solving this equation, a value of 0.19 Pa of shear stress at the bottom of the bed is obtained and this value for Aerosil® R974 powder is approximately the same at different powder loads. The U_{mf} is important because it can help us to determine the shear stress necessary for the gas flow to carry up the agglomerates in the channel and begin the dynamic fluidization process. The agglomerates that have been carried up by the gas stream will locate on the top of the bed forming layers of a new bed of increased voidage or porosity, and the increased porosity reduces the shear stress required to carry up the agglomerates; these effects are explained by Figures 3.12 and 3.13 (Rietema, 1991).

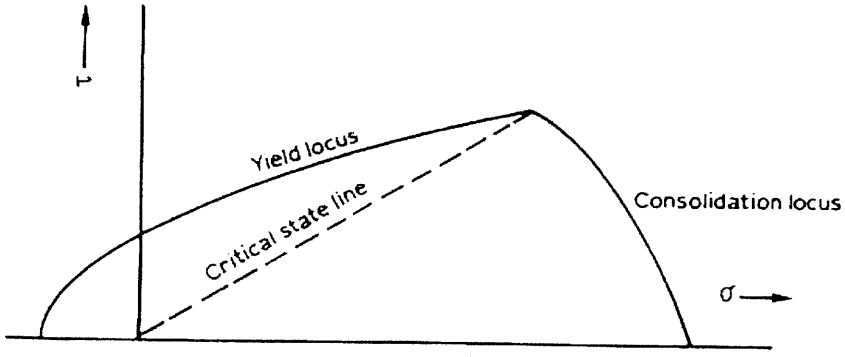

Figure 3.12 Yield locus, consolidation locus, critical state line.

Figure 3.12 shows that for a powder to start to flow, the shear stress (τ) has to reach a critical value determined by the critical state line. At these conditions, the normal stress σ is not too high, but the elasticity limit of the powder has been reached and the powder will yield and be sheared off along a plane "X" which is moving in the direction of the normal stress. The critical shear stress depends on the normal stress acting on the plane "X" and increases when the normal stress increases, as indicated by the yield locus. For non-cohesive powders the yield locus will intercept the origin of the (σ, τ) diagram, but for fine cohesive powders it will pass through a point in the negative σ-axis (Rietema, 1991).

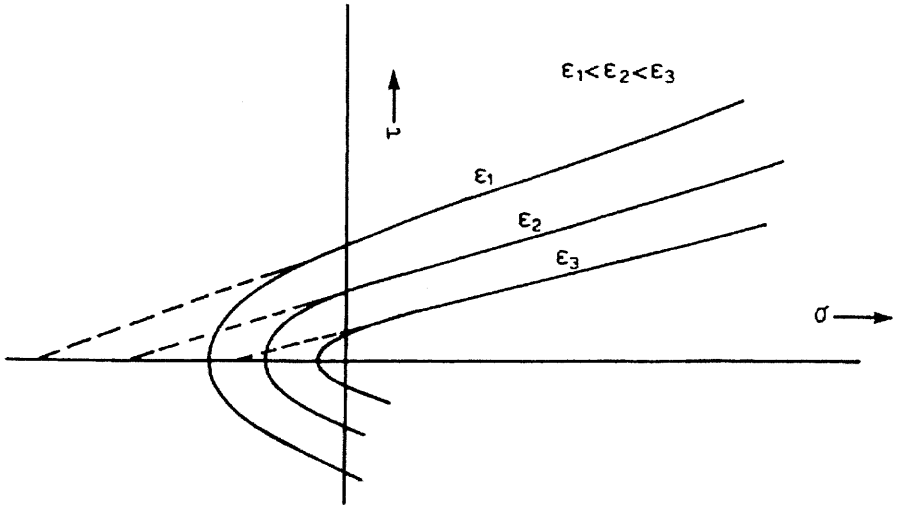

Figure 3.13 Yield locus at increasing porosity.

Figure 3.13 shows that the yield locus and consolidation locus depend on the original porosity of the powder in such a way that they shift to higher values at decreasing porosity. Also the critical normal stress and the corresponding critical shear stress will decrease at increasing porosity (Rietema, 1991). Hence, during channeling, the new layers of agglomerates formed at the top of the bed will have larger porosity, which means that they will require less normal and shear stresses to be moved.

One additional explanation for the channeling effect is that the powder packing of the agglomerates in the proximity of the wall increases the porosity of the bed as shown in Figures 3.14 and 3.15 (Rietema, 1991). Therefore, the fluid velocity will be higher in the proximity of the wall giving birth to the channel.

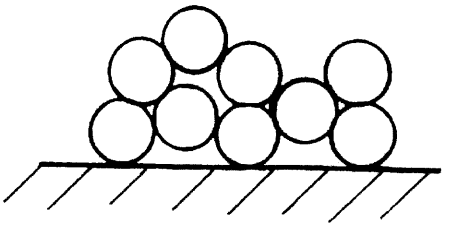

Figure 3.14 Increased porosities near the wall.

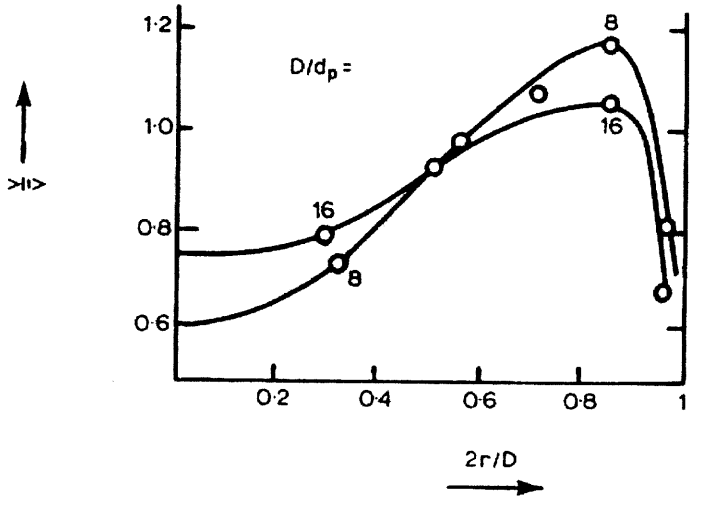

Figure 3.15 Local fluid velocity near the wall of the container.

In addition, the channel formation occurs randomly due to the non-uniformity of the porosity in the bed as mentioned in Rietema (1991). The wall effect, the random settling of particles, the cohesion between the particles and the particle size distribution deviate the porosity in the bed of powder.

Due to these factors, a model that can justify the fluctuations of the bed pressure drop found before fluidization must be based on channeling and the Hagen – Poiseuille equation. Thus the pressure drop across a channel can change if the density of the fluid (ρ), the diameter (R) and length of the channel

(L_C) change according to the equation for the mass rate flow (w) as mentioned by Bird, Stewart & Lightfoot (2001):

$$w=\frac{\pi(P_O-P_L)R^4\rho}{8\mu L_C} \tag{3.17}$$

and it can be seen that,

$$\Delta P \propto \frac{L_C \cdot w}{\rho R^4} \tag{3.18}$$

The density of the fluid going through the channel was assumed as the density value of the mixture of the gas and carried particles which may range between 10 to 20 kg/m^3 and it will depend also on the amount of particles dragged by the gas flow. Before reaching the minimum fluidization velocity, the length of the channel remains almost constant and equals to the initial bed height approximately. According to Equation 3.18, a small change in radius can change the pressure drop across the channel significantly and the pressure drop can also change due to the mass of dragged particles.

Regarding the estimation of the agglomerate size, the drag coefficient method can be used for the calculations, but a more accurate correlation for it is needed since agglomerates of nanoparticles are porous, non spherical particles and even collide with each other during fluidization. Therefore, further research could lead to an appropriate drag coefficient correlation for agglomerates of nanoparticles. Agglomerate sizes can be measured in the bed during fluidization by Focused-beam Reflectance Measurement (FBRM), and then the experimental agglomerate size measurements can aid in finding a suitable drag coefficient correlation.

CHAPTER 4

MAGNETICALLY ASSISTED FLUIDIZATION OF AGGLOMERATES OF NANOPARTICLES

4.1 Introduction

As it has been seen in the last chapter, one of the main problems in fluidization is to overcome the shear forces of the powder, in order to make it loose so that the gas flow can distribute uniformly across the entire bed. There are two main obstacles to obtain fluidization: the presence of large agglomerates right above the distributor that promote the formation of channels by breaking the uniformity of the gas field, and the cohesive force between agglomerates. Cohesion among agglomerates result in shear forces which need to be overcome, to separate the agglomerates and open new paths for the gas to flow through the bed by increasing the bed voidage.

The use of magnetic particles to obtain smooth bubble-less fluidization was based reported by Coulaloglou (1979), in which different kinds of ferromagnetic materials with different coercivity were fluidized before and after being magnetized; in all the cases, the minimum fluidization velocity increased for the magnetized particles. Also, Rosensweig et al. (1987) stabilized a fluidized bed containing nonmagnetizable particles with a magnetizable fluid or ferrofluid, which consists of a stable colloidal dispersion of super paramagnetic particles of about 0.01 microns in size. Saxena et al. (1996) studied magnetically stabilized air fluidized beds of a mixture of magnetic and non-magnetic millimeter size particles. In these experiments a Helmholtz coil was used for the generation of a

homogenous vertical magnetic field. Hristov (1997) studied the effects of the direction of the magnetic field on the fluidization of ferromagnetic particles. Li et al. (1999) fluidized a mixture of ferromagnetic particles and calcium carbonate (Group C) particles, and it was found that the fluidization quality of Geldart Type-C particles could be improved by the magnetic assistance. Change in the fluidization behavior, from Group B to A, of iron particles of micron size was studied by Rhodes et al. (2001); in this case the magnetic field generator was placed on the bottom of the column near to the distributor and consisted of a Helmholtz electromagnet, which generated a constant and uniform magnetic field collinear with the air velocity vector. Magnetic particles have been used also as assistance for impaction coating processes (Singh et al., 2001).

In the present work, magnetic particles enhanced fluidization by breaking large agglomerates at the bottom of the bed and by opening new paths for gas flow, increasing the bed porosity and thereby reducing the shear stress necessary to drag the agglomerates towards fluidization.

The improvement of the fluidization of agglomerates of nanoparticles by the movement of magnetic particles under the influence of an oscillating magnetic field depends on several factors such as the magnetic field intensity, percentage of magnetic particles, homogeneity of the magnetic field and frequency, among others. The magnetic field used to move the particles is not homogenous, oscillates and it is located at the bottom of the bed only. Also, the magnetic particles are larger and heavier than the powder to fluidized, and they serve only to disrupt the interparticle forces holding the agglomerates together.

4.2 Behavior of Magnetic Particles in an Oscillating Magnetic Field

The magnetic particles that assist the fluidization of powders play a key role in these processes; many powders will not fluidize without assistance, but can be fluidized if assisted by an external force field such as magnetic field (Yu et al., 2004), sound (Zhu et al., 2004) or vibration (Nam et al., 2004).

One of the objectives of these fluidization experiments is to identify the fluidization characteristics of agglomerates of nanoparticles such as the minimum fluidization velocity, pressure drop and bed expansion when assisted by the movement of magnetic particles. Therefore, it is important to quantify the contribution of the magnetic particles in enhancing the fluidization characteristics and to identify the conditions under which the magnetic particles are effective in promoting fluidization.

Experiments were performed using the experimental setup shown in Figure 4.1.

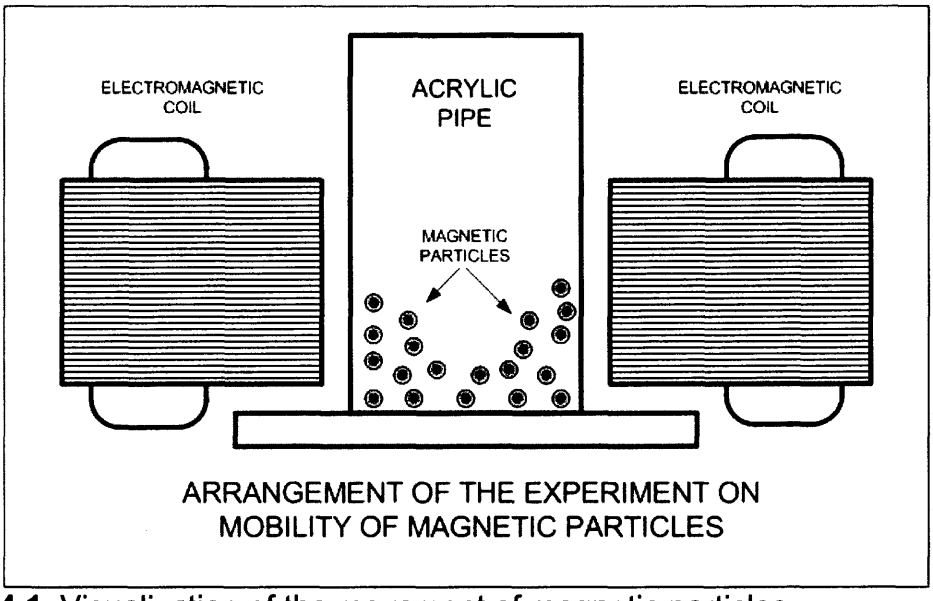

Figure 4.1 Visualization of the movement of magnetic particles.

The magnetic field was characterized by a Gaussmeter, which measured the intensity and direction of the magnetic field over the surface of the distributor at different positions. A close-up view of the geometry of the probe is shown in Figure 4.2; the probe has a flat tip which measures the intensity of the magnetic field perpendicular to it.

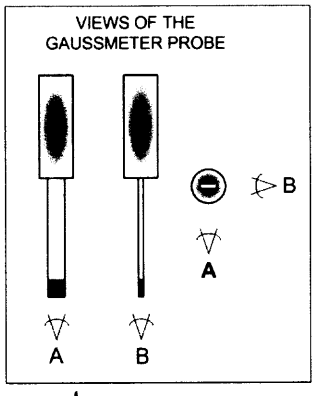

Figure 4.2 Probe of the Gaussmeter.

As previously mentioned, the magnetic field intensity was measured along several points over the distributor as shown in Figure 4.3, to determine the direction and homogeneity of the magnetic field intensity.

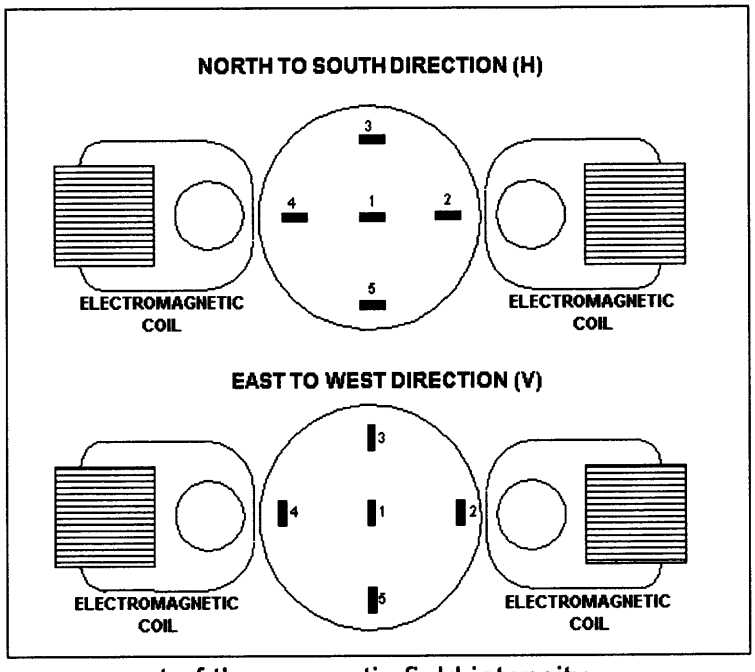

Figure 4.3 Measurement of the magnetic field intensity.

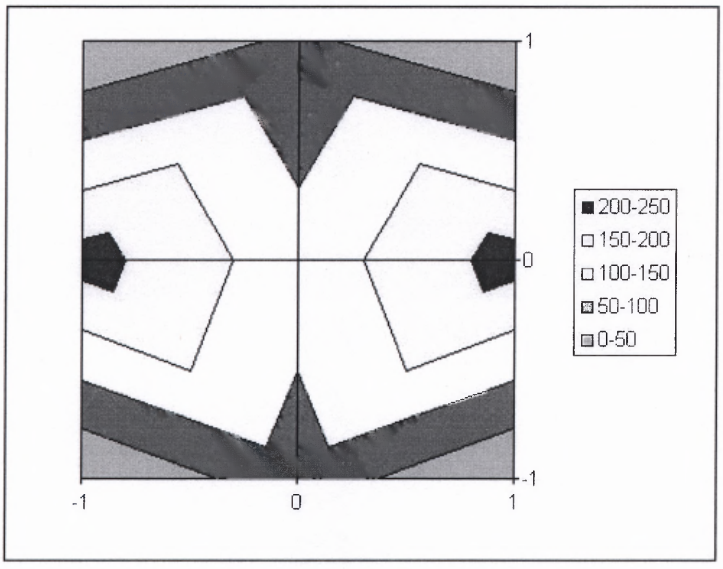

Figure 4.4 Intensity of the AC Magnetic Field over the distributor in Gauss.

Measurements of the magnetic field intensity indicated that it was not homogeneous as can be seen in Figure 4.4; moreover, Figure 4.4 shows the results of measurements done in the North-South direction, in which the highest intensity was obtained. Measurements in the East-West direction showed a similar distribution over the area but a much lower intensity of about 60 Gauss at the highest point. Hence, it played a relatively small role in the movement of the magnetic particles.

It is important to note that a DC magnetic field was also present, but its intensity was negligible compared to the AC magnetic field (the DC magnetic field intensity was about 20 Gauss). In addition, it was found more convenient to work at low frequencies because of the linear relationship between the power required by the electromagnetic coils and the current frequency, as shown in Figure 4.5. However, in these experiments magnetic particles move in the absence of powder, i.e., in an empty bed.

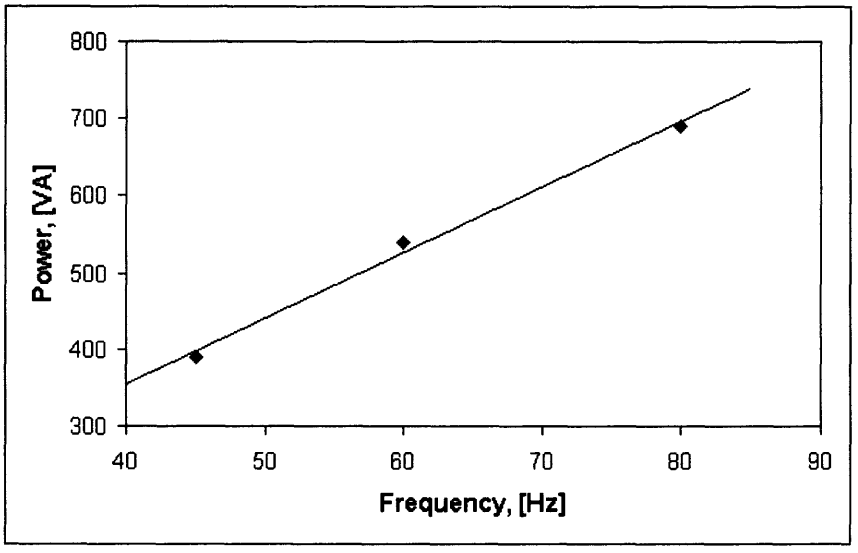

Figure 4.5 Power consumption depending on frequency.

If the magnetic field intensity is weak, the magnetic particles tend to agglomerate and remain motionless over the distributor, breaking the homogeneity of the gas field and therefore causing adverse effects on the fluidization as shown in Figure 4.6. On the other hand, under stronger magnetic field intensity, all the particles move without forming agglomerates as shown in Figure 4.7.

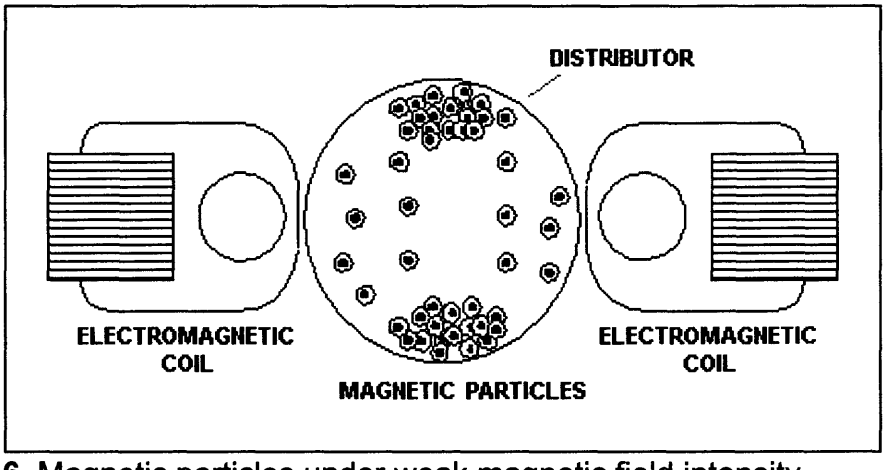

Figure 4.6 Magnetic particles under weak magnetic field intensity.

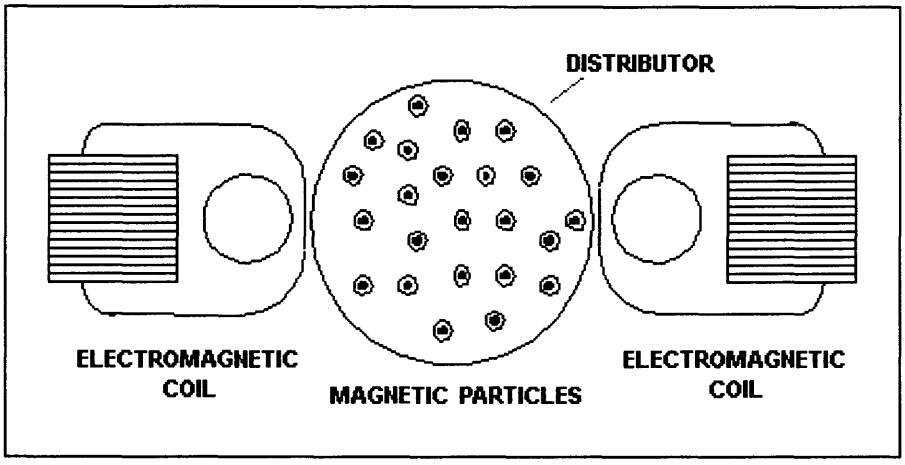

Figure 4.7 Magnetic particles under strong magnetic field intensity.

4.3 Experimental Set-Up

Similar to the conventional fluidization experiments, a column made of acrylic plastic was used, but in addition to the 2.25" column, a 1" column I.D. was also used for comparison purposes. A pair of electromagnetic coils was used for generating the magnetic field, and a frequency converter supplied the desired AC for the coils at a selected frequency. Due to the generation of heat, the coils had to be cooled down by air blown past them by a fan. The experimental set up is shown schematically in Figure 4.8.

A voltage and frequency regulator (Triathlon Precision AC Source) allowed to adjust the power supply to the electromagnetic coils and by doing so the intensity of the magnetic field. It is important to note that the magnetic particles were made of barium ferrite ($BaO\text{-}6Fe_2O_3$), a ferromagnetic material with relatively high coercivity.

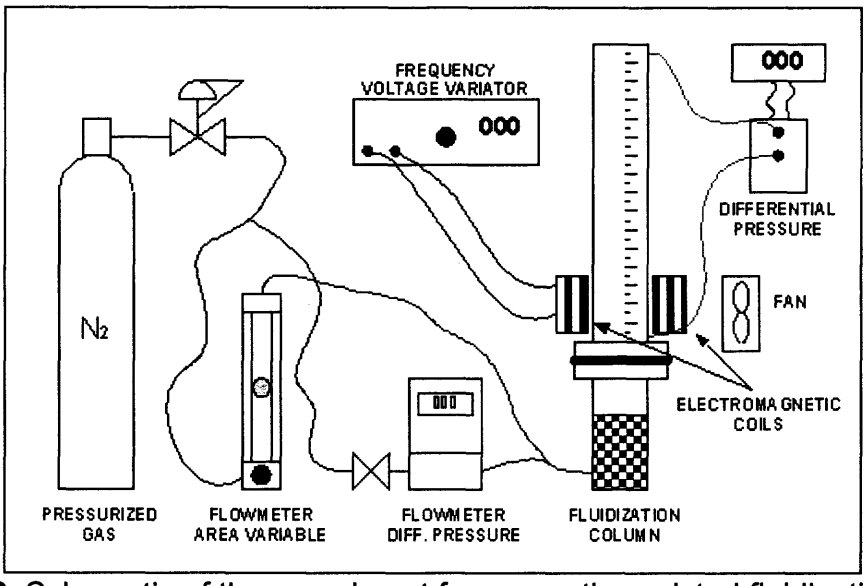

Figure 4.8 Schematic of the experiment for magnetic assisted fluidization.

4.4 Procedure

Different amounts of powder were placed inside the column and it was not necessary to sieve the powder in order to get smooth fluidization since the magnetic excitation was sufficient to break down even the very large agglomerates. However, in order to compare with the conventional fluidization experiments in some cases, the powder was sieved and a certain amount of agglomerates larger than 500 um (the ones that break the homogeneity of the gas flow) were added on purpose to make the fluidization difficult so as to better evaluate this method. Thus experiments were performed using only soft agglomerates (less than 500 um) and a mixture of soft agglomerates and large agglomerates.

After loading the powder into the fluidization column, the magnetic particles (1.5 – 2 mm diameter made of barium ferrite) were added. The mass fraction of magnetic particles was significant due to their high density, but their

volume fraction was small; furthermore, due to the very low air flow required for the agglomerates of nanoparticles to fluidize, movement of the magnetic particles occurred only due to the external magnetic field.

In addition to using different combinations of magnetic particles and agglomerates of nanoparticles, the voltage and frequency were changed using a frequency converter so that the movement of the magnetic particles could be intensified by increasing the intensity of the magnetic field. The frequency was changed in the range of 45 to 100 Hz, and the voltage in the range of 60 to 120 V; these changes were limited by the electromagnetic coils, since they were designed for a current intensity of 3 Amps each.

4.5 Results

One of the major objectives of the experiments was to determine the effect of the magnetic particles on the fluidization of agglomerates of nanoparticles. As discused in Chapter 3, Aerosil® R974 can fluidize at low gas velocities if the agglomerates have a diameter under 500 um.

When using magnetic particles as assistance to fluidization, agglomerates of nanoparticles larger than 500 um can be broken by the collisions with the magnetic particles. Therefore, it is not necessary to sieve the powder to get a smooth fluidization, but if the as received powder without sieving is fluidized, the U_{mf} is very high, and it is significantly reduced by the magnetic assistance as shown in Figures 4.9 and 4.10.

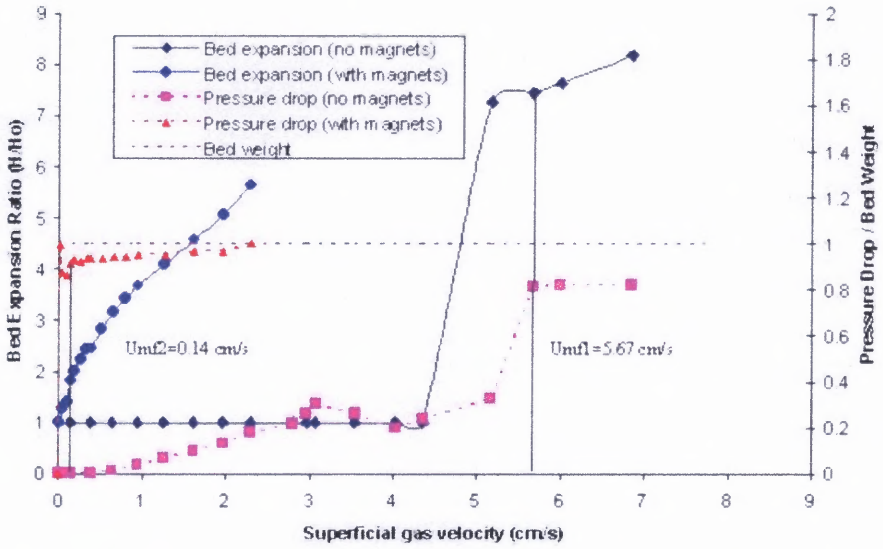

Figure 4.9 Fluidization characteristics of Aerosil® R974 without sieving showing results with and without magnetic assistance.

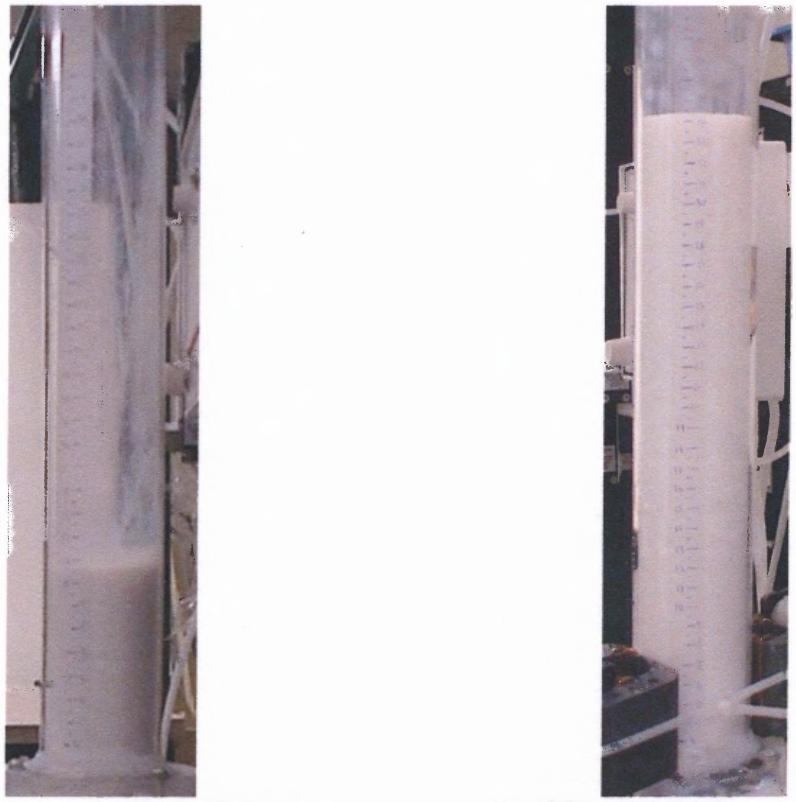

(a) Without magnetic assistance. (b) With magnetic assistance

Figure 4.10 Fluidization of Aerosil® R974 without sieving at similar flow conditions.

The amounts of magnetic particles used in the magnetic assisted fluidization also play a significant role in the results. In order to quantify the effect of using different amounts of magnetic particles a certain quantity of Aerosil® R974 (10 grams) was placed in the fluidization column and fluidization runs were done using 2.6, 5.2, 10.4 and 20.8 grams of magnetic particles, successively. Figures 4.11 and 4.12 show the fluidization characteristics of 10 grams of Aerosil® R974 when assisted by different amounts of magnetic particles; for these experiments the only variable changed between the runs was the amount of magnetic particles.

Although an improvement in the quality of fluidization occurs when increasing the amount of magnetic particles, this does not necessarily mean that the greater the amount of magnetic particles the better; it will be shown later that there is an optimum amount of magnetic particles which depends on the diameter of the column and the intensity of the magnetic field.

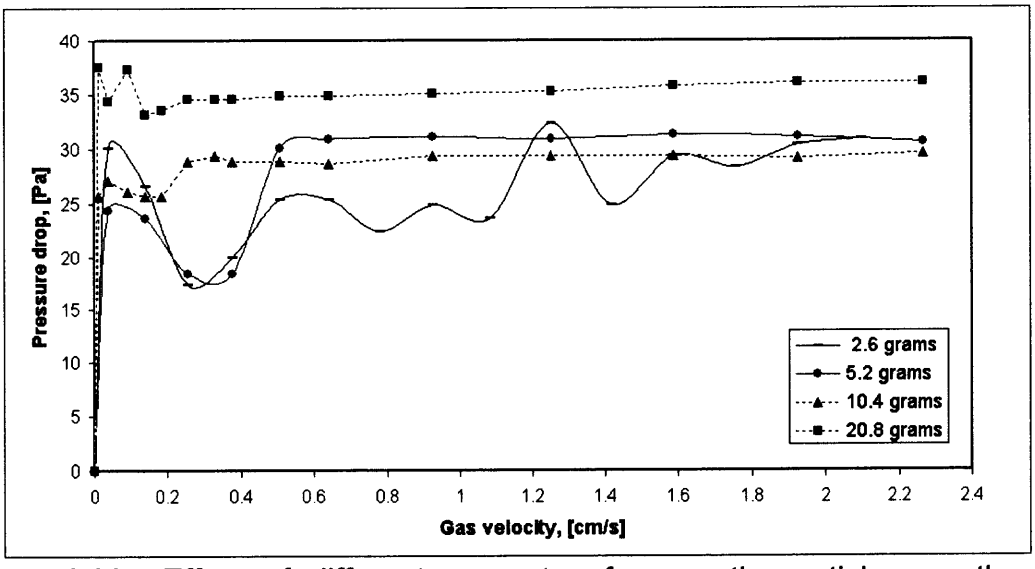

Figure 4.11 Effect of different amounts of magnetic particles on the bed pressure drop during fluidization of 10 grams of Aerosil® R974 previously sieved (110 VAC, 60 Hz).

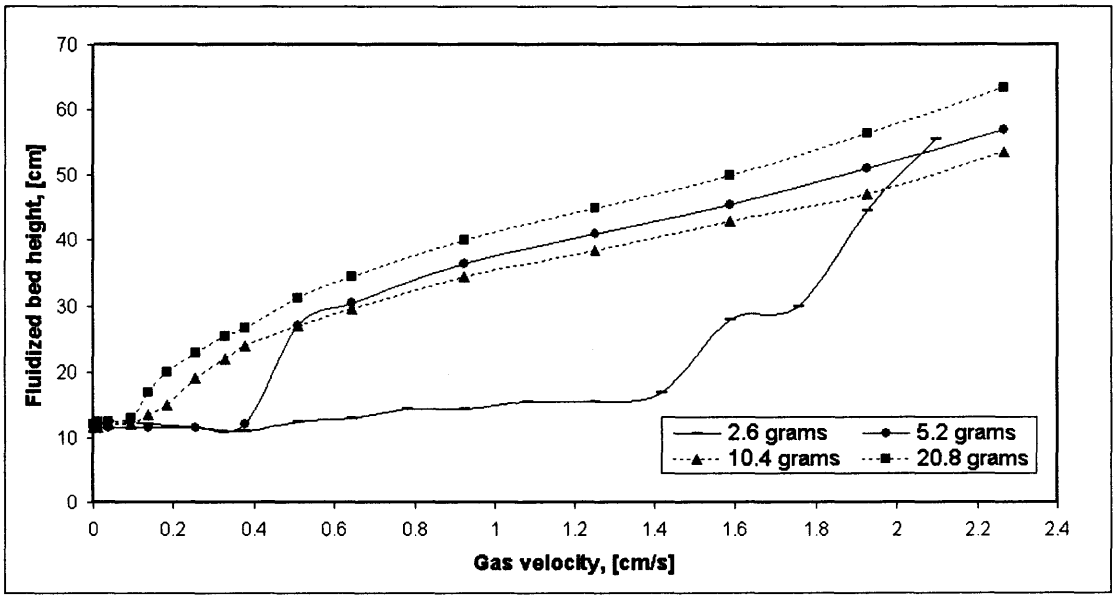

Figure 4.12 Effect of different amounts of magnetic particles on the bed expansion during fluidization of 10 grams of Aerosil® R974 previously sieved (110 VAC, 60 Hz).

The effect of the intensity of the magnetic field was also studied; however, this was limited by the fact that the electromagnetic coils could not generate a stronger than 120 Gauss magnetic field for more than 30 minutes and the time for carrying out the experiments were at least 1 hour.

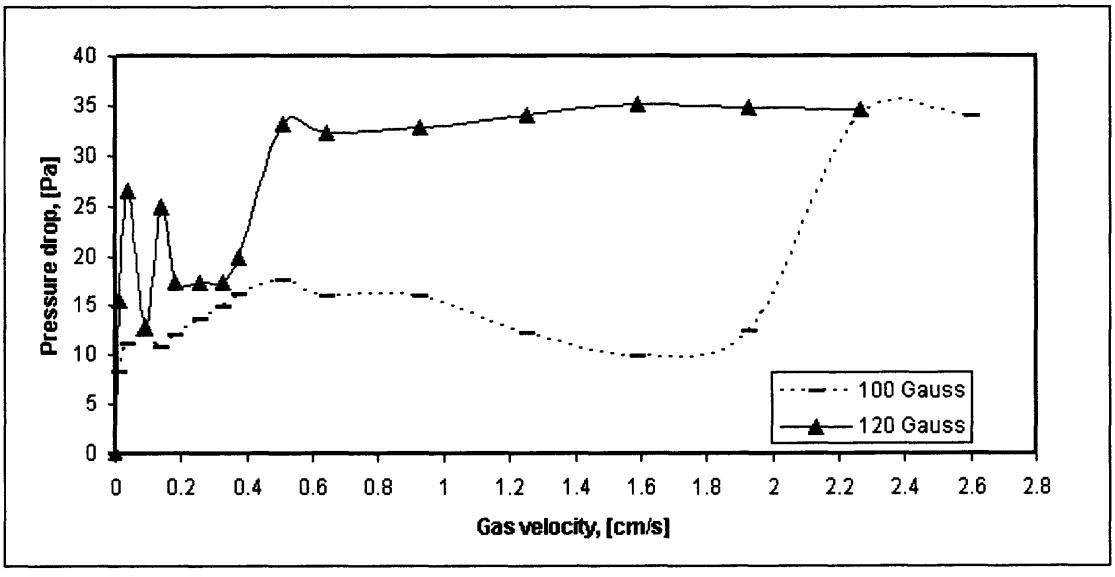

Figure 4.13 Effect of the intensity of the magnetic field on the fluidization of 10 grams of Aerosil® R974, pressure drop (110 VAC, 60 Hz, 20.8 grams of M.P.)

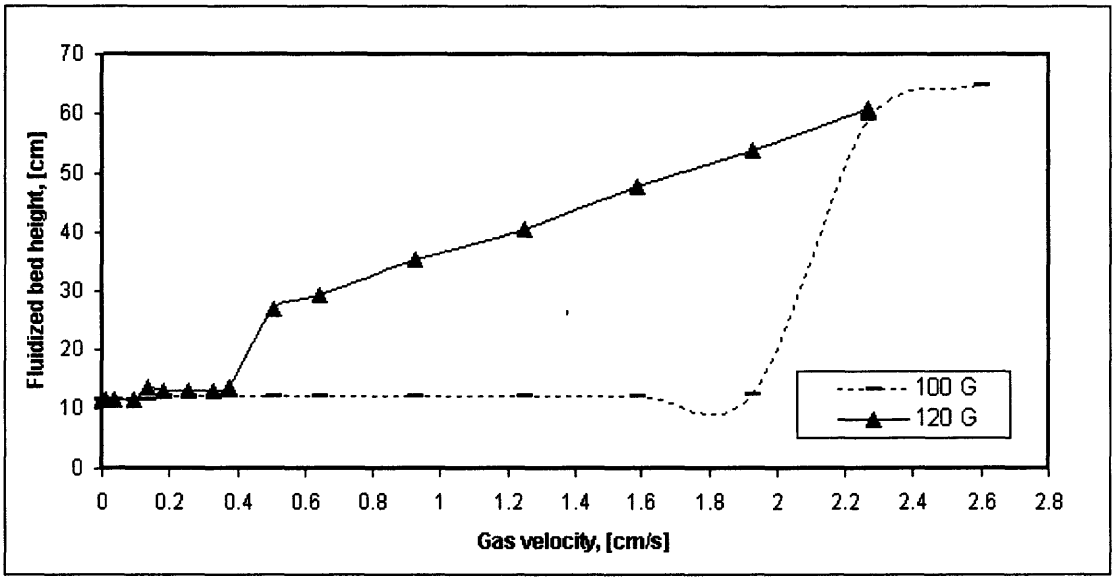

Figure 4.14 Effect of the intensity of the magnetic field on the fluidization of 10 grams of Aerosil® R974, bed expansion (110 VAC, 60 Hz, 20.8 grams of M.P.)

In Section 4.2 it was shown that at lower frequencies of the alternating current less energy is used in the electromagnetic coils. Experiments using different frequencies for the AC supply were run and the effects on the fluidization are shown in Figures 4.15 and 4.16. In these runs the mass of Aerosil® R974 was 10 grams, the amount of magnetic particles was 20.8 grams and the magnetic field intensity was held constant at 120 Gauss. Thus frequency was the only variable that was changed.

It can be seen that both low and high frequencies give poor results. According to these plots, it seems that there should be an optimal frequency. An additional problem arises at lower frequencies due to the increase in current, the electromagnetic coils heat up faster, increasing the resistance of the coil and this may affect the magnetic field intensity performance.

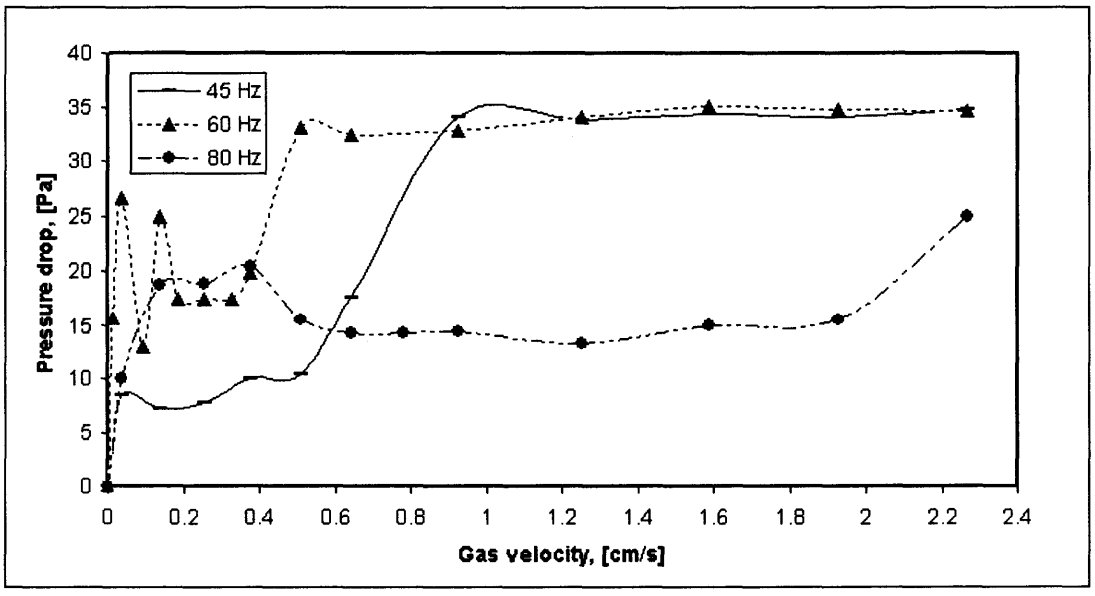

Figure 4.15 Effect of different power supply frequencies on the bed pressure drop.

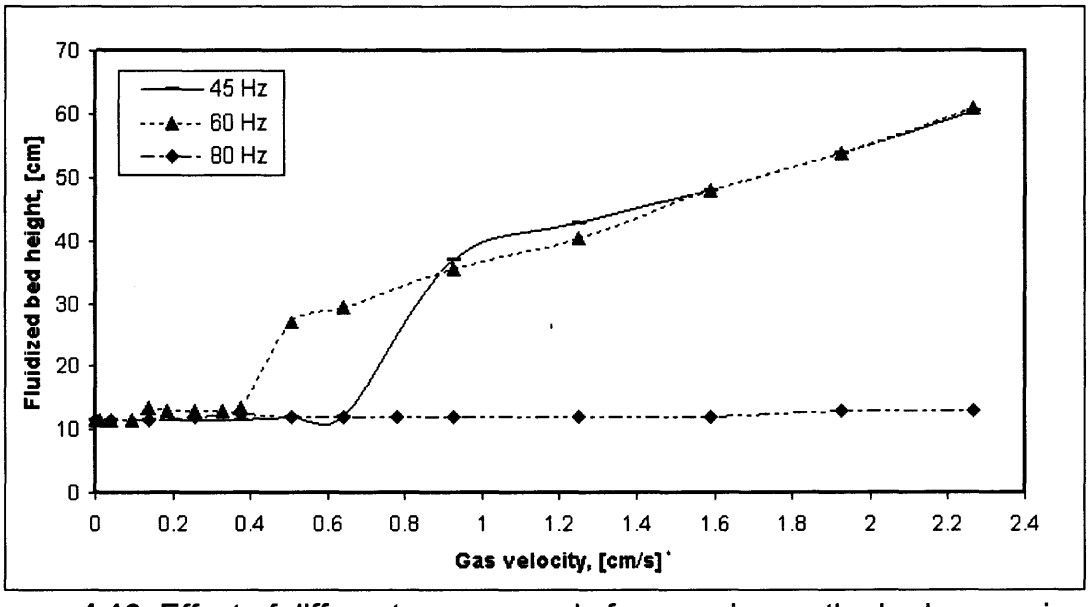

Figure 4.16 Effect of different power supply frequencies on the bed expansion.

For fluidization experiments of Aerosil® R974 in a 1 inch I.D. column, different amounts of agglomerates were used; specifically 1, 2 and 2.5 grams; it was not possible to fluidize these powders without magnetic assistance even though they were previously sieved to select agglomerates under 500 um.

According to mixing experiments, an optimum amount of magnetic particles for use in the 1 inch I.D. column was about 0.3 grams. Therefore 0.3 grams was used in all the experiments done in this small column with Aerosil® R974.

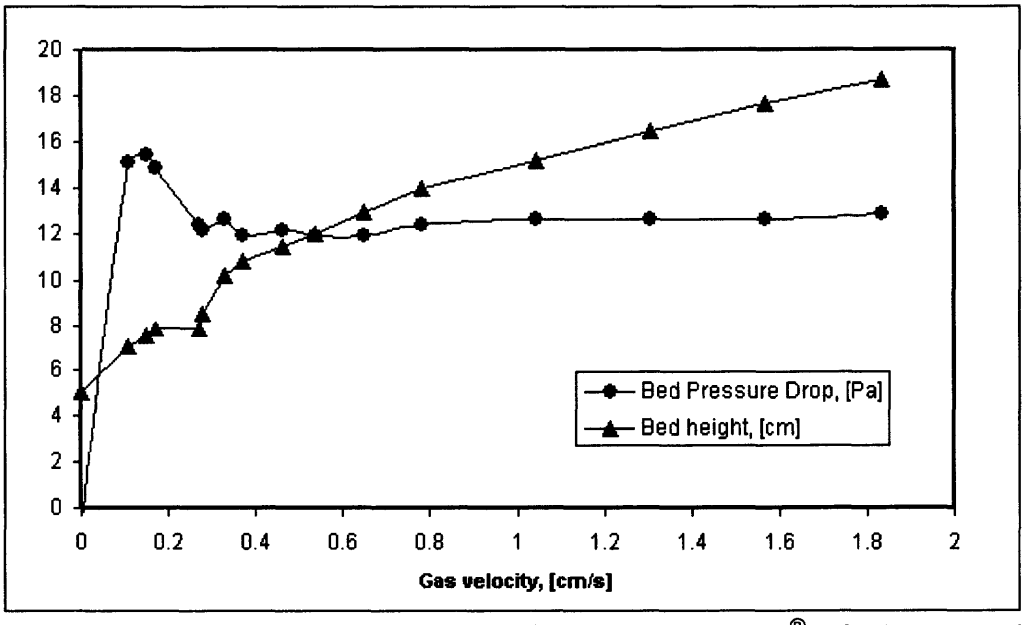

Figure 4.17 Fluidization characteristics of 1 gram of Aerosil® R974, magnetically assisted experiments with 0.3 grams of magnetic particles.

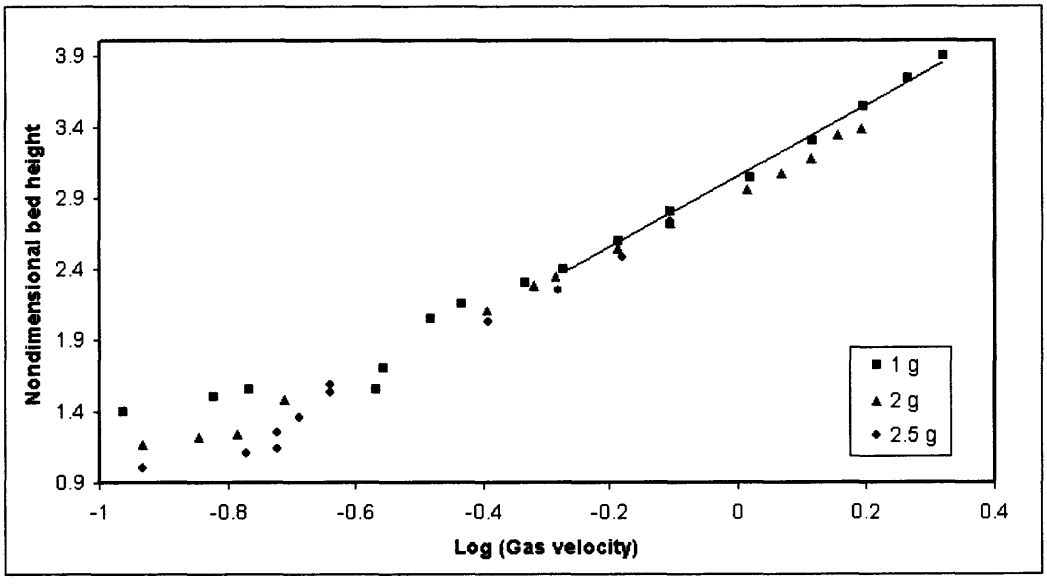

Figure 4.18 Nondimensional bed expansion of the fluidization experiments of different amounts of Aerosil® R974 in a 1" I.D. column.

Figure 4.17 shows a typical fluidization plot for 1 gram of Aerosil® R974 in a 1" I.D. column when assisted by 0.3 grams of magnetic particles. There is a pressure "overshoot," when gas velocities are below the U_{mf} due to column wall effects. In Figure 4.18, the non-dimensional bed expansion vs. the logarithm of the gas velocity is shown for different amounts of powder, and it can be seen that the fluidization behavior does not depend on the amount of powder that was fluidized and that there is a linear tendency when the bed is fully fluidized. Moreover, scatter of the data can be seen at gas velocities below the U_{mf} (U_{mf} = 0.4 cm/s; Log (U_{mf}) = -0.4).

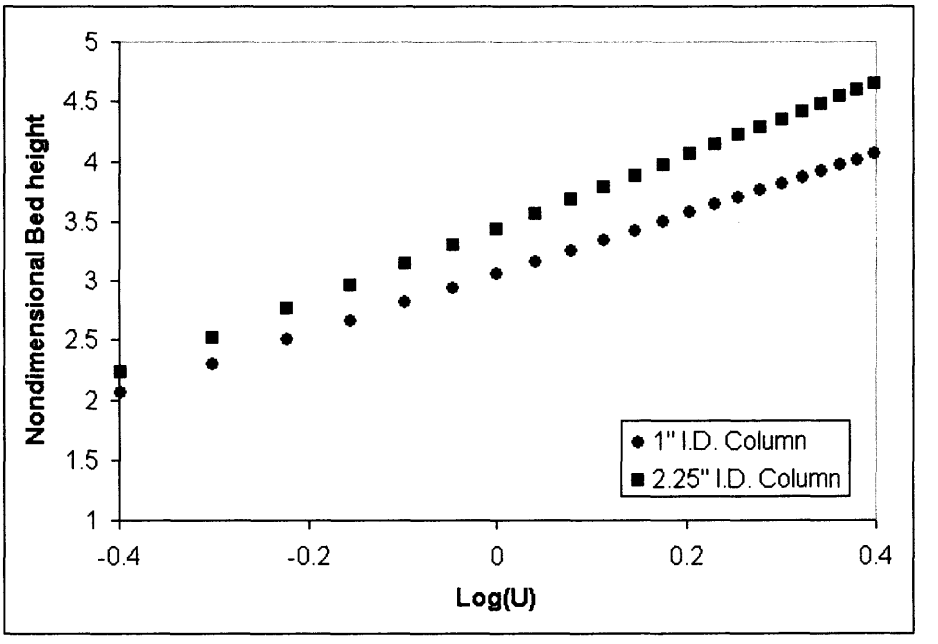

Figure 4.19 Effect of different power supply frequencies on the bed expansion.

Figure 4.19 shows that in a 2.25" I.D. column, the bed expansion is larger than in a 1" I.D. column. The lower expansion in the smaller column may mean that more energy is required to overcome friction between the moving powder and the walls of the fluidization column.

4.6 Mixing of Agglomerates of Nanoparticles by Magnetically Assisted Fluidization

One of the applications of magnetic assisted fluidization is in mixing of agglomerates of different nanoparticles. Therefore, experiments were done in the 1 inch I.D. column. The two powders used were Aerosil® Aluminum C (Al_2O_3 nanopowder, white, primary particle size of about 13 nm) and Nanocat® Superfine Iron Oxide (ferric oxide nanopowders, reddish brown, primary particle size of about 3 nm) provided by Mach 1, Inc.

The minimum fluidization velocity for Aerosil® Aluminum C mixed with Nanocat® Iron Oxide in the proportion of 10:1 was found to be close to 1 cm/s (data not shown). The reason for the 10:1 ratio was because at higher iron oxide to aluminum ratios it was very difficult to visually quantify the mixing, which was based mainly on the homogenous dispersion of aluminum oxide agglomerates.

It was not possible to fluidize either aluminum oxide or iron oxide in the 1 inch I.D. column without the magnetic assistance. However, the amount of magnetic particles used in the experiments played a significant role and an optimum ratio of agglomerates of nanoparticles to magnetic particles was found to be 10:1 for the 1 inch I.D. column as can be seen in Figure 4.20. This ratio can change depending on the size of the column.

It was also found that the fluidization results were affected with respect to time because of the formation of a cake over de distributor and/or the increase of the resistance of the electromagnetic coils due to overheating causing a decrease in the intensity of the magnetic field.

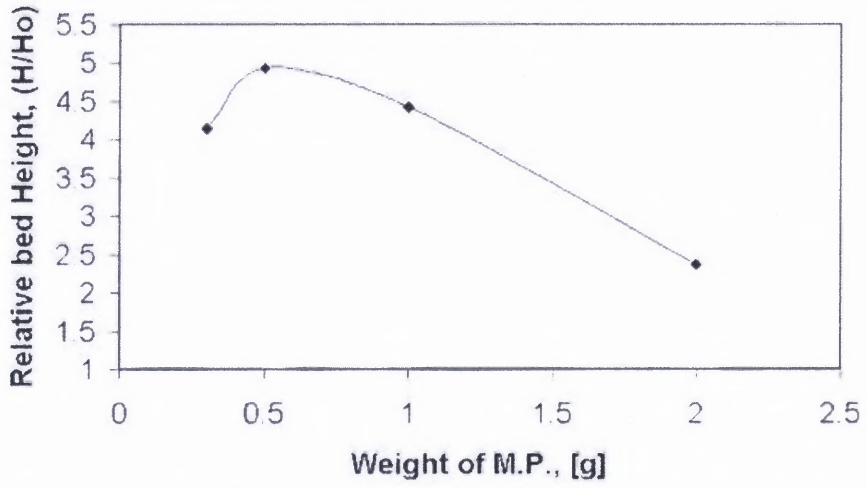

Figure 4.20 Effect of the amount of magnetic particles on the maximum bed height expansion during the mixing by magnetically assisted fluidization (Powders: Aluminum oxide, ferric oxide; ratio: 10:1; 1" I.D. column).

After 10 minutes of fluidization, a homogeneous mixture can be seen; but some large aluminum oxide agglomerates still remain. After 30 minutes, the experiment had to be stopped because of the overheating of the electromagnetic coils. Figure 4.21 (a) and (b) show a comparison between the agglomerates of nanoparticles before and after mixing, respectively.

(a) Before fluidization: Al_2O_3 (white) and Fe_2O_3 (reddish brown)

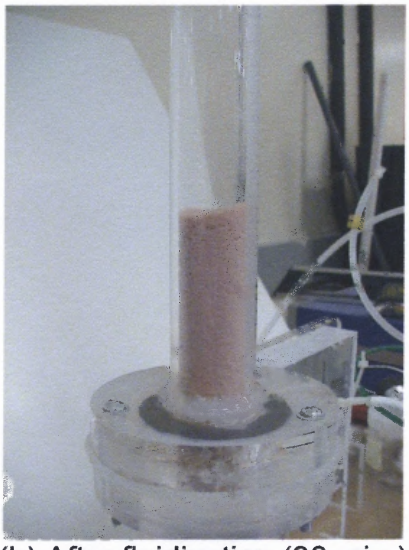

(b) After fluidization (30 min.)

Figure 4.21 Mixing of Al_2O_3 and Fe_2O_3 nanopowders.

4.7 Conclusions and Discussion

It has been shown that assistance of fluidization by the movement of magnetic particles under the influence of a magnetic field enhances the fluidization by lowering the minimum fluidization velocity (Figure 4.9); but the effect of the magnetic assistance on fluidization depends on the amount of magnetic particles (Figures 4.11 & 4.12), the magnetic field intensity (Figures 4.13 &4.14) and the frequency of the power supply of the electromagnetic coils (Figure 4.15 & 4.16), among others. It is also interesting to note that sieving of the agglomerates of nanoparticles is no longer necessary for obtaining a smooth fluidization of agglomerates of nanoparticles of Aerosil® R974, since the magnetic particles destroy the large agglomerates that break the homogeneity of the air flow at the bottom of the fluidization column. By doing this, magnetic assistance becomes important because it avoids gas bypassing through the fluidized bed enhancing the mixing between the fluid and particulate materials.

The mixing experiments showed that mixing occurs at the micro scale and not at the nano scale, since later SEM images showed that the agglomerate size of Al_2O_3 was of the order of hundreds of microns (data not shown). Therefore, this technique works to mix agglomerates of nanoparticles rather than the nanoparticles themselves; however, it is not known if longer fluidization time may enhance mixing at the nano scale since the agglomerates behave dynamically – that is, they are continually breaking and reforming.

CHAPTER 5

GAS FLUIDIZATION OF AGGLOMERATES OF NANOPARTICLES IN A ROTATING ASSEMBLY

5.1 Introduction

Fluidization of fine powders, like agglomerates of nanoparticles, is important because of the breaking up (disaggregation) and spreading out of the agglomerates into smaller agglomerates, which allows taking advantage of their smaller size and their high specific surface area. Breaking the agglomerates requires force fields in which the agglomerates are subject to opposite forces applied at different points of the agglomerate; for example, the agglomerate's weight is a force applied at the inertial center of the agglomerate while a drag force due to a gas flow is applied at the surface of the agglomerate. These opposite forces generate shear stresses inside the agglomerate, and depending on their intensity, are capable of breaking the agglomerate.

A rotating fluidized bed (RFB) can generate the appropriate conditions for the breaking up of agglomerates and subsequent reduction of their size. In this unit, the angular speed of the chamber, containing agglomerates of nanoparticles, generates a centrifugal force which artificially increases the weight of the agglomerates; moreover, this centrifugal force can be controlled by adjusting the rotating speed. As particles are under a force balance while fluidized, the drag force required to fluidize agglomerates in a rotating fluidized bed has to be larger than in a conventional fluidized bed. It is believed that under these forces, breakup of the agglomerates occurs.

During the fluidization of agglomerates of nanoparticles in a conventional fluidized bed under normal gravity conditions, elutriation takes place at even low gas velocities; however, by using a centrifugal force field it is possible to apply higher gas flow rates without as much elutriation.

Previous works in a rotating fluidized bed include fluidization of micron size particles, glass beads and alumina, (Qian et al., 2001); and corn starch (Watano et al., 2003). A linear relationship between the minimum fluidization velocity and the artificial gravity force (centrifugal force) was found for fluidization of micron size powders.

Some discrepancies were found between the experimentally measured and estimated (theoretical) bed pressure drops in the fluidization experiments. In some cases, the experimental bed pressure drop was less than the estimated pressure drop as can be deduced from data reported in the fluidization of corn starch (Watano et al., 2003). Fluidization experiments done with glass beads, magnesia clinker and sand showed that the estimated bed pressure drop exceeded the experimental one by a margin of 20% (Fan et al., 1985). A mathematical model developed for a rotating fluidized bed overestimated the bed pressure drop for experiments with polyethylene millimeter size granules (Kao et al., 1987). Oddly enough, in some cases, the experimental bed pressure drop exceeded the theoretical bed pressure drop by threefold in the fluidization of ultrafine particles in a rotating fluidized bed (Tsutsumi et al., 2001). Hence, it is difficult to predict the bed pressure drop across a rotating fluidized bed of powder.

Moreover, even though the rotating unit was not loaded with powder, changes in the pressure drop across the chamber, while flowing gas through it, occurred when the direction of the rotation of the chamber was changed even though the magnitude of the gas flow rate was kept constant (Zhu et al., 2001).

It has been reported that rotation is an additional factor for destabilization and may contribute to different flow patterns and pressures (Brouwers, 2002), and that the rotating effect becomes even more important when the Reynolds number based on rotational speed is higher than a certain value.

Besides the factors that can affect the experimental bed pressure drop such as elutriation, wall effects or the design of the unit, it is believed that previous models for estimating the bed pressure drop in a rotating fluidized bed have been missing an important contribution. It will be shown that Coriolis forces and their effects play a role in the discrepancies between experimental and theoretical bed pressure drops in the rotating fluidized bed; these discrepancies become even more noticeable under the low flow conditions required during fluidization of agglomerates of nanoparticles, where the minimum fluidization velocities are of about two orders of magnitude less than those required for fluidizing micron size particles.

In the present work, fumed Silica (Aerosil® R974 and Aerosil® R972 provided by Degussa Japan – Nippon Aerosil Co.) and Titanium Dioxide (Aeroxide® P 25 provided by Degussa USA) were fluidized under different centrifugal force fields, specifically, 211, 299, 366 and 423 rpm which simulated 10, 20, 30 and 40 times the normal gravity force, respectively. The fluidization

behavior of these powders was recorded including the bed height expansion and bed pressure drop. Subsequently, the minimum fluidization velocity for each powder was found by plotting the bed pressure drop vs. the gas velocity; moreover, a relationship between the minimum fluidization velocity and the simulated gravity force was examined.

Due to discrepancies found between the experimental and theoretical bed pressure drops, a review of the existing models led to the conclusion that some of the assumptions made do not apply for a rotating fluidized bed. Therefore, a different model based on a rotating frame of reference is proposed; previous models were based on a fixed inertial frame and did not consider the effects of rotation. Results of numerical simulations using Fluent® corroborate the importance of the Coriolis forces and the magnitude of the tangential velocity of the fluid relative to the rotating frame of reference.

5.2 Experimental Set-Up and Procedures

Details of the rotating unit are shown in Figure 5.1, it includes a chamber which encloses a cylindrical stainless steel sintered wire mesh with an aperture size of 20 um, a thickness of 3 mm, a diameter of 400 mm and 100 mm in depth. This cylindrical mesh distributes the gas and holds the particulate material while rotating along its axis of symmetry at a controlled speed. The unit has a stationary cylindrical filter of 100 um mesh with a thickness of 3 mm, 100 mm in diameter and 90 mm in depth; its function is to retain any elutriated fine powder.

The covers of the chamber and gas distributor are made of acrylic plastic which allowed for visualization of the fluidized bed of powder.

The rotating distributor was driven by a motor and its velocity could be adjusted by a motor speed controller; in addition, the rotating speed was measured with a tachometer. This configuration was assembled by Nara Machinery Co. (Tokyo, Japan) as a medium scale lab prototype.

The plenum chamber, that enclosed the rotating distributor, received air delivered by a blower (Hitachi, VBD-080). Its rotating speed, and therefore its output, was adjusted by a motor speed controller. The air flow delivered by the blower was measured by an area variable flowmeter with a range from 3 to 50 m^3/h.

Inside the chamber, pressure taps connected to a differential pressure transmitter were placed as shown in Figure 5.1. The higher pressure tap was placed in the chamber that surrounded the gas distributor and the lower pressure tap was placed right before the inner filter. Hence, the instrument measured the pressure drop so that if the rotating chamber was empty the readings corresponded to the pressure drop across the distributor and the gas region, but if the rotating chamber was loaded with powder, the readings corresponded to the pressure drop across the distributor, the fluidized powder and the gas region. The differential pressure transmitter was connected to a computer that worked as a display.

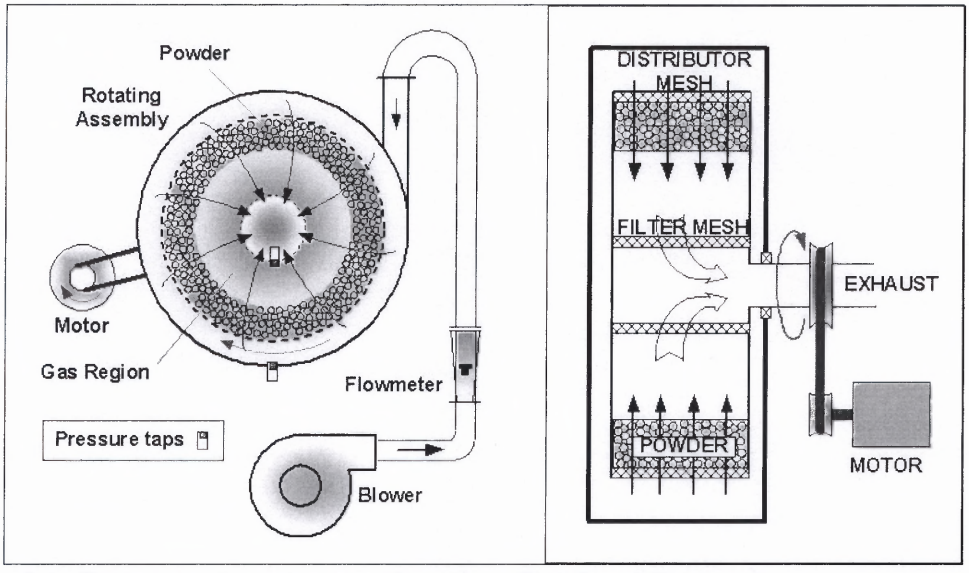

Figure 5.1 Diagram showing the Rotating Fluidized Bed unit.

Since the bed pressure drop across the powder bed could not be measured directly, it was necessary to find a relationship between the gas distributor's pressure drop and the gas velocity; this was done by running the unit without powder at a constant rotating speed and changing the gas flow. Then the bed pressure drop across the powder bed could be quantified by subtracting the pressure drop measured when the unit was empty from the pressure drop when the unit was loaded with powder at the same rotating speed and gas flow conditions.

A digital camera recorded the behavior of the agglomerates of nanoparticles during fluidization; a pointer laser was used to determine the bed expansion as well as its homogeneity and the pressure drop across the inner filter was quantified by a water manometer.

Regarding the hydrodynamic classification of the powders used in the present experiments, Aerosil® R974 and R972 show smooth fluidization without

bubbling, characteristic of Group A powders, and Aeroxide® P25 (TiO_2) shows Group B like behavior. While the nanoagglomerates show a strong cohesive behavior, they are quite different than group C powders due to the formation of highly porous fractal agglomerates.

Due to the relatively long period of time that the as received nanoparticles are contained in a bag for storage and transportation purposes, the cohesive interactions between the particles cause the formation of agglomerates of many different sizes; therefore, for purposes of repeatability of these experiments, the powders were sieved using a shaker and a sieve of Mesh No. 60 (mesh opening about 250 um). This procedure was followed since it was observed that the fluidization behavior could be changed by the size of the agglomerates. Furthermore, fluidization experiments done with non-sieved agglomerates did not result in good fluidization behavior with large bed expansion (data not shown).

The fumed silica used in the experiments has a tapped density of about 50 g/l and a bulk density of about 30 g/l. R974 has an average particle size of 12 nm while R972 has an average particle size of 16 nm; for each powder 70 grams of material were used. Aeroxide® TiO_2 P25 has an average particle size of 21 nm and a tapped density of 130 g/l and a bulk density of about 90 g/l; 250 grams of this powder were used for the experiments. For all three powders, the amount of material used and loaded into the rotating chamber gave an initial bed height of about 0.02 m.

The experimental procedure for each batch of experiments can be summarized as follows. First, the unit was carefully cleaned, so that a uniform

and repeatable air field is generated by the air distributor. Next, all the different parts of the unit were carefully assembled and all the joints were properly sealed in order to prevent leaks which could cause erroneous results in the pressure drop readings. This was followed by the measurement of the pressure drop across the distributor (RFB unit without powder) using different air flow rates, and at a predetermined rotational speed (211, 299, 366 and 423 rpm). Then each batch of the powder was loaded into the unit and the rotating speed was set at the desired value in order to increase the centrifugal force (which simulated an artificial gravity force). Simultaneously, the air flow was increased slowly and the data such as air flow, pressure drop and bed height were recorded for different values of the air flow. A similar procedure was followed for several other values of the rotating speed for all three powders that were studied.

5.3 Results of the Experiments

As explained in previous chapters, a plot of the bed pressure drop against the gas velocity can be used to determine if the powder has reached full fluidization. Before minimum fluidization conditions, as the gas flow increases progressively, the bed pressure drop increases proportionally to the gas flow, but once all the powder is fluidized, and supported by the gas flow, no further increase in the bed pressure drop is expected and it becomes constant. This region is called the "plateau region."

The following figures show the bed pressure drops measured at different rotating speeds that simulated an artificial gravitational force of 10, 20, 30 and 40

times normal gravity (1G = 9.8 m/s^2). Full fluidization of the powder can be seen for all of the different artificial gravitational forces and powders used since a plateau region was reached; however, when compared to conventional fluidization, the plateau region was shortened because of elutriation of powder at higher air velocities.

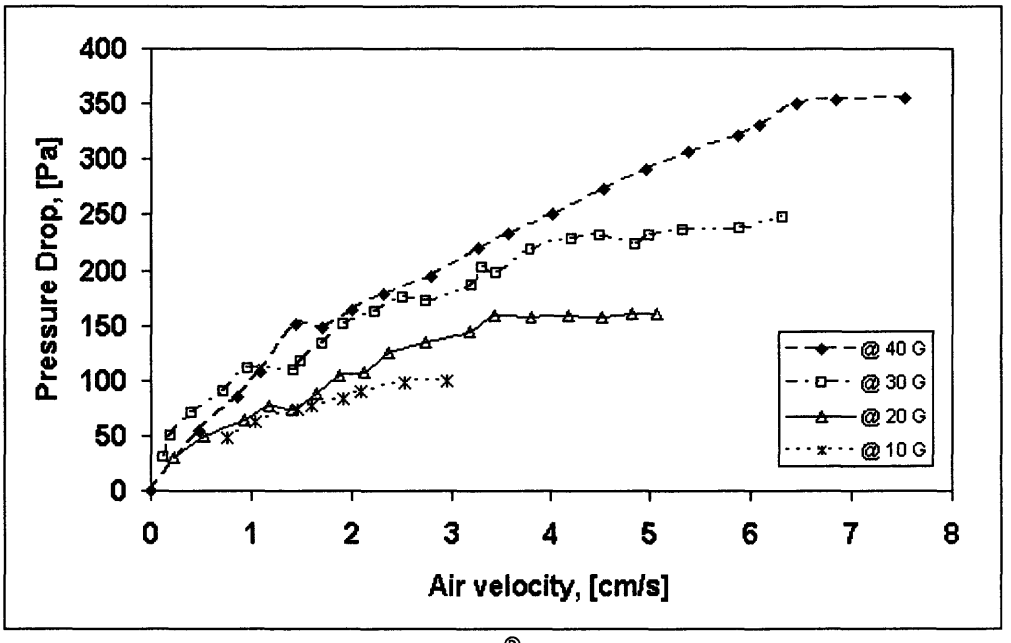

Figure 5.2 Bed Pressure drop of Aerosil® R974.

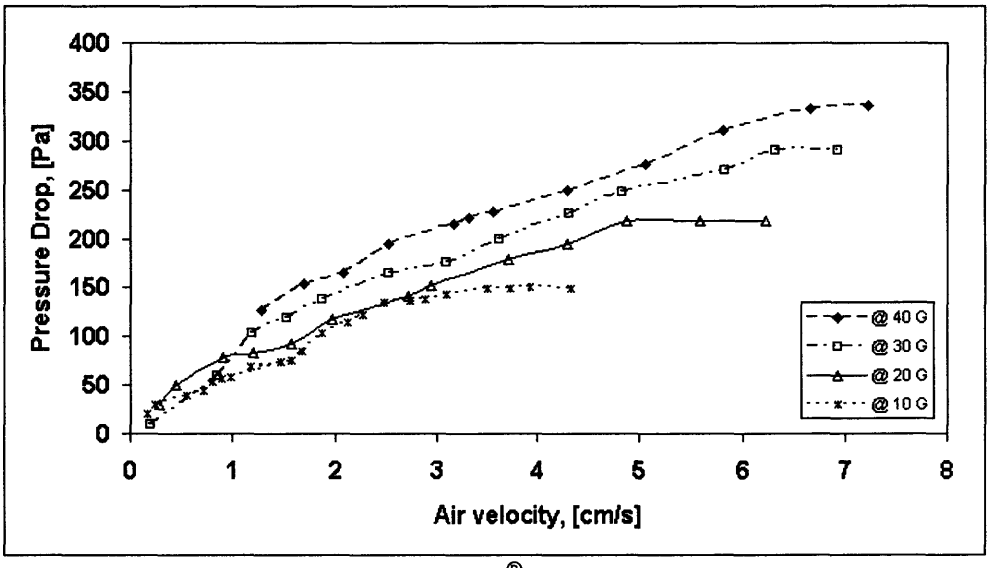

Figure 5.3 Bed Pressure drop for Aerosil® R972.

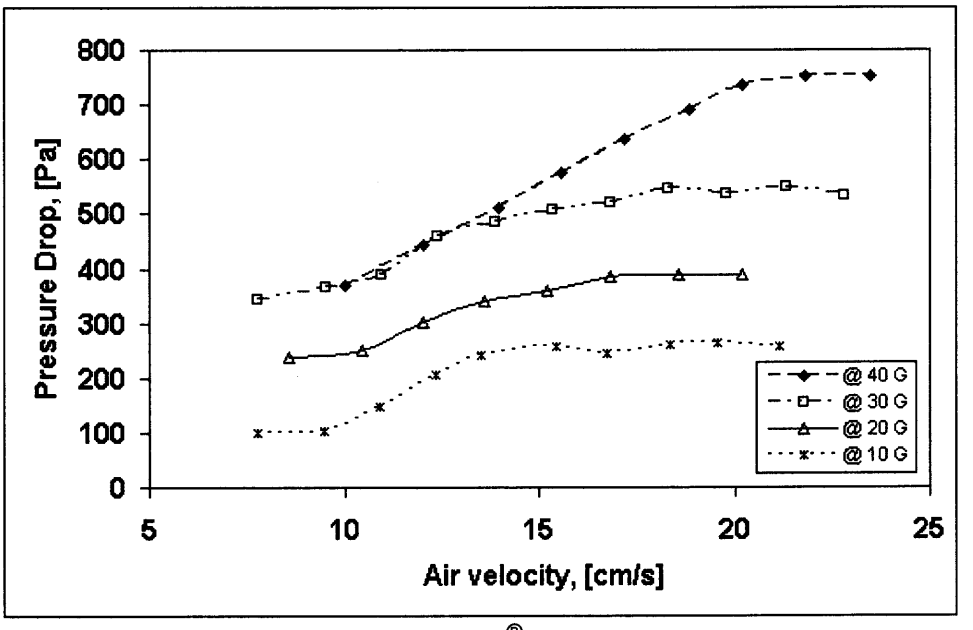

Figure 5.4 Bed pressure drop of Aeroxide® P25.

A further increase in the gas velocity above the values shown in Figures 5.2, 5.3 and 5.4 caused significant elutriation of powder and the experiment was stopped; therefore, the plateau region is shorter than in conventional fluidization. In Figure 5.4, many of the values of bed pressure drop before minimum fluidization have been omitted since they fluctuated widely.

The minimum fluidization velocity was found from the plots from the interception of the straight lines that correspond to the before fluidization and the plateau regions. Table 5.1 summarizes the minimum fluidization velocities obtained from the graphs. The results are also plotted in Figure 5.5.

Table 5.1 U_{mf} for the Different Powders at Different Rotating Speeds

Gravity Force "g"	R974 cm/s	R972 cm/s	P25 cm/s
10	2.4	3.5	15
20	3.4	4.8	16.8
30	4.5	6	18.3
40	6.5	7	20.5

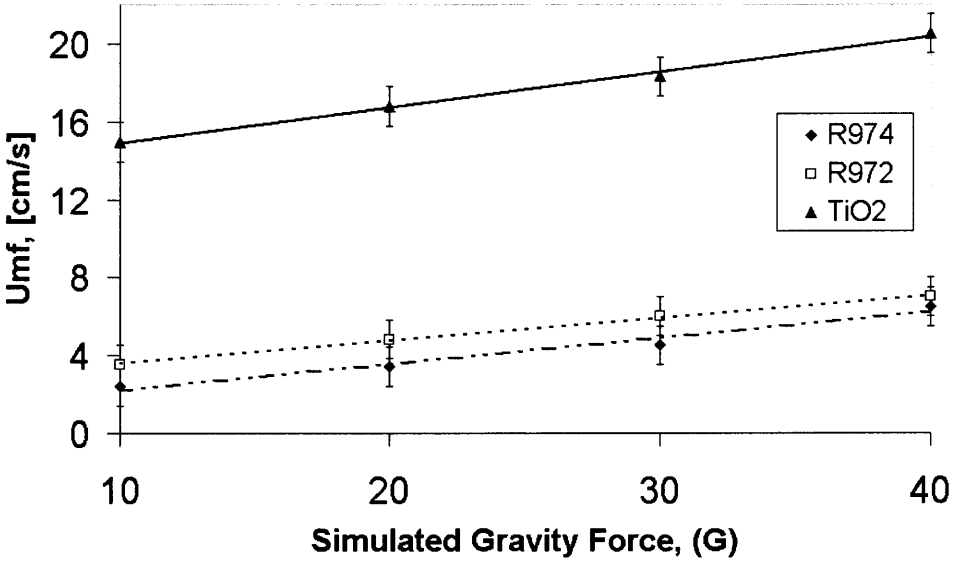

Figure 5.5 Minimum fluidization velocity of the powders at different rotating speeds that simulated an artificial gravity force (1G = 9.8 m/s^2).

Regarding the bed expansion, it was found that Aerosil® R974 and R972 expanded considerably compared to Aeroxide® P25 and micron-size particles as reported in the literature. This high bed expansion is a very peculiar characteristic of agglomerates of nanopowders and it is not seen when fluidizing micron-size denser particles. Figures 5.6, 5.7 and 5.8 show the bed expansion obtained for the powders at different gas velocities and rotating speeds. It is seen that the bed expansion of Aerosil® R974 is slightly less than that of R972;

this is a consequence of the loss of powder due to elutriation. Aeroxide® P25 shows a very small bed expansion that appears to decrease with the centrifugal force "G" and is very difficult to quantify.

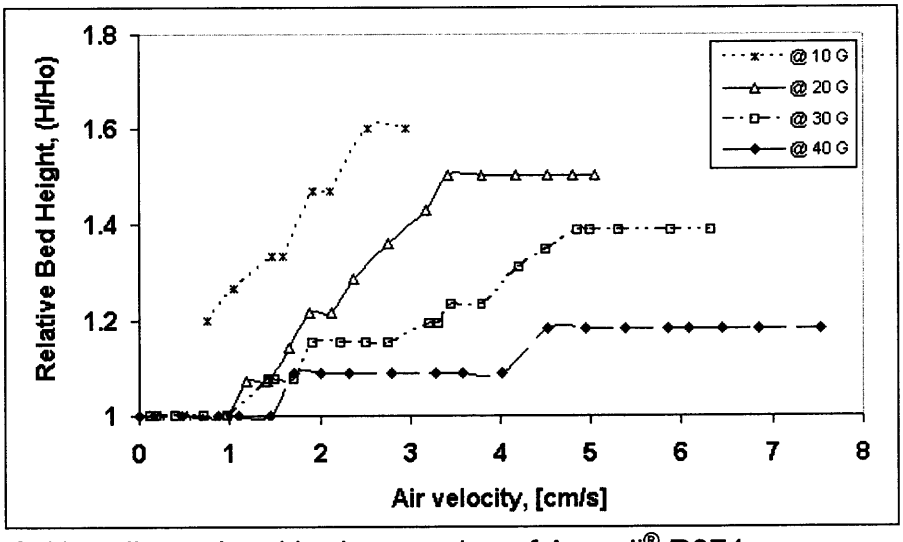

Figure 5.6 Non-dimensional bed expansion of Aerosil® R974.

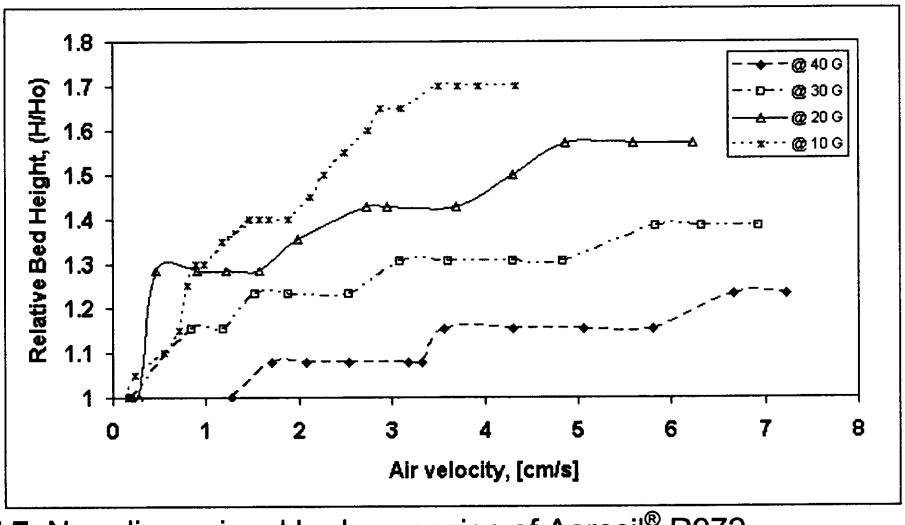

Figure 5.7 Non-dimensional bed expansion of Aerosil® R972.

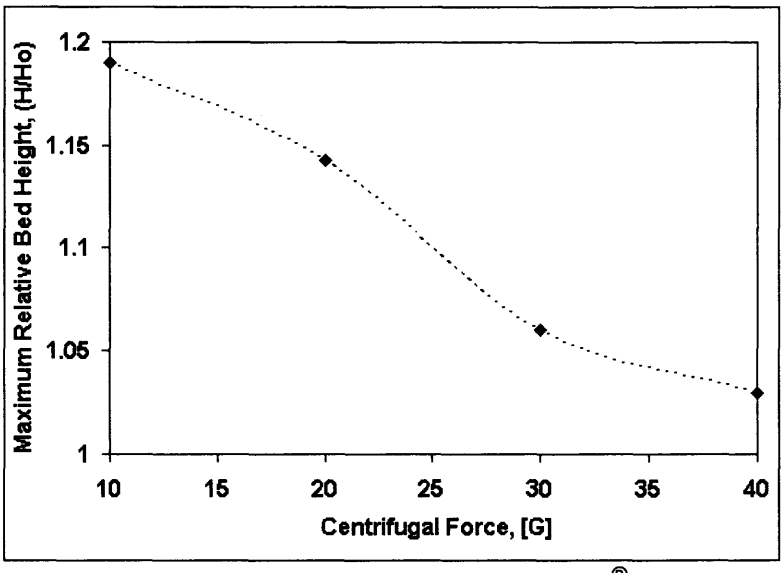

Figure 5.8 Non-dimensional bed expansion of Aeroxide® P25.

5.4 Discussion and Theory

Theoretical analyses of the bed pressure drop in a rotating fluidized bed are based mainly on using the Ergun approach (1952) to obtain the drag force exerted on the particles by the interstitial gas velocity (Chen, 1987). Chen assumed the gas to be an incompressible fluid, and a system configuration as shown in Figure 5.9. This system configuration does not account for changes in the tangential velocity of the gas phase that may occur as a consequence of the geometry of the unit, the initial tangential velocity at the entry, and the gas phase pressure distribution. As can be seen in Figure 5.9, the system is assumed to have a perfect radial symmetry, a fact that does not consider the cyclone type gas entrance of the unit.

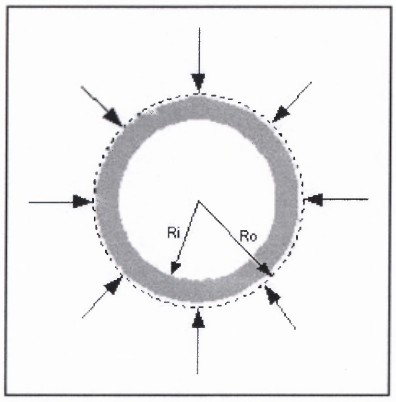

Figure 5.9 Schematic of the flow through the bed according to Chen (1986).

Furthermore, the Ergun equation was conceived for a bed of relatively large spherical particles in an inertial fixed frame, in which the effects of a rotating fluid were not considered. Despite these unfavorable conditions for applying Ergun's equation, a local momentum balance for the gas phase led to a model for estimating the bed pressure drop (Jackson, 1971), as shown in Equation 5.1:

$$\frac{dP}{dr} = -\Phi_1 \bar{u}_r + \Phi_2 \bar{u}_r^2 + \rho_g r\Omega^2 - \rho_g u_r \frac{du_r}{dr} \tag{5.1}$$

By applying the equation of continuity, Equation 5.2 is obtained:

$$\frac{dP}{dr} = -\Phi_1 \bar{u}_r + \Phi_2 \bar{u}_r^2 + \rho_g r\Omega^2 + \frac{\rho_g \bar{u}_r^2}{\varepsilon^2 r} + \frac{\rho_g \bar{u}_r^2}{\varepsilon^3} \frac{d\varepsilon}{dr}, \tag{5.2}$$

where

$$\Phi_1 = \frac{150(1-\varepsilon)^2 \mu}{\varepsilon^3 (\phi_s d_p)^2}, \quad \Phi_2 = \frac{1.75(1-\varepsilon)\rho_g}{\varepsilon^3 \phi_s d_p} \tag{5.3}$$

A theoretical analysis of the bed pressure drop based on the above equations led to the following equation for the fluidized bed region (Chen, 1986).

$$\frac{dP}{dr} = \rho_g (1-\varepsilon) r\Omega^2 + \rho_f \varepsilon r\Omega^2 + \frac{\rho_f U_0^2 r_0^2}{\varepsilon r^3} + \frac{\rho_f U_0^2 r_0^2}{\varepsilon^2 r^2} \frac{d\varepsilon}{dr} \tag{5.4}$$

Equation 5.4 was further simplified, assuming that the effects of inertia and variable porosity were negligible (Kao et al., 1987). Thus

$$\frac{dP}{dr} = (\rho_g - \rho_f)(1-\varepsilon) r\Omega^2 \tag{5.5}$$

represents the bed pressure drop for the fluidized bed region.

The bed pressure drop for the fixed-bed region will not be discussed in this work, since the flow mechanism in a fixed bed of nanoagglomerates is not fully understood even for conventional fluidization. As explained in Chapter 3, applying Ergun's equation to a fixed-bed of agglomerates of nanoparticles is problematical due to the peculiar properties of the nanoagglomerates and the non homogeneity of the flow passing through the fixed bed.

Since discrepancies were found between the experimental and theoretical bed pressure drops in the fluidization experiments of agglomerates of nanoparticles, it was necessary to review the existing models and to rethink the fluidization problem in a rotating assembly. In this context, Figure 5.10 represents in a better description of the flow pattern under which agglomerates of nanoparticles were fluidized. In comparison with Figure 5.9, it can be seen that the unit is not symmetrical since there is only one entrance; in addition, it is believed that changes in the tangential velocity of the fluid inside the chamber must be considered since the tangential velocity will depend on many factors such as the pressure and velocity at the entrance of the chamber and the rotating speed of the distributor. Moreover, agglomerates of nanoparticles are very light

and easy to drag by the air flow which causes a significant bed expansion as shown in the experimental results. This implies the presence of a force that moved the particles in the radial direction, and thus, Coriolis forces may play a significant role.

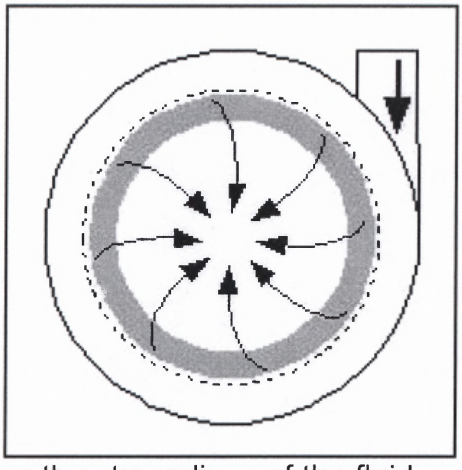

Figure 5.10 RFB showing the streamlines of the fluid.

In fluid flow analysis, the mass conservation and the Navier-Stokes equations are key for finding a solution; even for turbulent flows, both equations are valid, but in this case the flow field becomes so complicated that it is extremely difficult to find an exact solution to the problem. In previous models of the rotating fluidized bed, a rigid-body rotational system in a fixed inertial frame was assumed, in which the tangential velocity is proportional to the radius $\left(v_\theta = \Omega r\right)$. It is believed that this rigid-body assumption does not represent the fluid behavior in a rotating fluidized bed.

In order to analyze a flow region of interest in a rotating fluidized bed, a noninertial rotating reference frame can be used; this leads to the Navier-Stokes vector equation written for a reference frame rotating at constant angular velocity

given by Equation 5.6, which represents the fluid flow problem in a rotating fluidized bed.

$$\frac{\partial \mathbf{v}}{\partial t}+(\mathbf{v}\cdot\nabla)\mathbf{v}+\boldsymbol{\Omega}\times(\boldsymbol{\Omega}\times\mathbf{r})+2\boldsymbol{\Omega}\times\mathbf{v}=\frac{1}{\rho}\mathbf{f}-\frac{1}{\rho}\nabla\mathbf{p}+\frac{\mu}{\rho}\nabla^2\mathbf{v} \tag{5.6}$$

where $\boldsymbol{\Omega}\times(\boldsymbol{\Omega}\times\mathbf{r})$ is the centripetal acceleration, and $2\boldsymbol{\Omega}\times\mathbf{v}$ is the Coriolis acceleration. Both of these additional terms are due to the rotating frame of reference.

The continuity equation is also invariant to the transformation from the fixed inertial to the rotating noninertial frame. It becomes $(\nabla\cdot\mathbf{v}=0)$, with all quantities now relative to, and expressed as components in, the rotating frame (J. P. Vanyo, 2001).

Equation 5.6 represents a force balance if the density of the fluid (ρ) is placed on the left hand side of the equation; i.e., each term has units of force which balance each other according to Newton's law. In this context, it should be noted that the pressure term (second in the right side) can be balanced either by the centrifugal force (third term in the left side) and/or the Coriolis force (fourth term in the left side). It is also important to note that since a new reference frame has been established, the velocity term in Equation 5.6, corresponds to the local velocity, which means the velocity of the fluid relative to the rotating frame. Therefore, if the velocity of the fluid changes, a change in the pressure drop will also occur.

The fundamentals for developing a theoretical model has been explained briefly here and in more detail in Vanyo (2001). The conservation of momentum

and Navier-Stokes can be applied to our rotating fluidized problem; additional factors to consider are that the rotating fluidized bed is modeled at steady state condition $\left(\frac{\partial \mathbf{v}}{\partial t} = 0\right)$ and that the bed of powder behaves fluid-like when fully fluidized. In addition, only the fluid gas phase will be considered so complications with modeling a two phase fluid flow are avoided.

A cylindrical coordinate system is defined as shown in Figure 5.11, having the distributor rotating at an angular speed of $\boldsymbol{\Omega} = \Omega\mathbf{k}$ which is positive since its rotating vector direction, following the right hand rule, is pointing in the same direction as the unit vector **k** of the reference frame. In the rotating unit the fluid enters tangentially like in a cyclone, and it can be assumed that the fluid vector can be represented by $\mathbf{v} = (-v_r, v_\theta, 0)$, neglecting the velocity in the direction of the unit vector **k,** which only becomes important at the exit which is out of the region of interest. Since the directions of the frame of reference are taken arbitrarily, if they were changed, i.e., a unit vector **k** pointing downward in Figure 5.11 or pointing away from the motor in Figure 5.1, the signs of the rotating vector and the tangential velocity would also have to be changed.

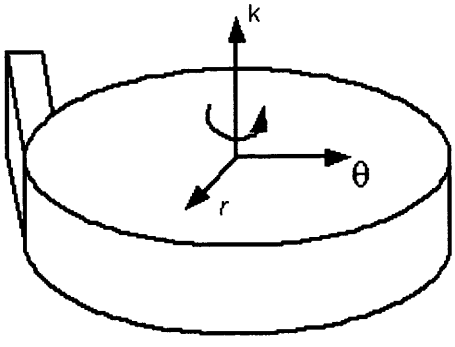

Figure 5.11 Coordinate system selected for the modeling, unit vector k pointing towards the motor (looking the unit from the back).

In Equation 5.6 the term $\boldsymbol{\Omega}\times(\boldsymbol{\Omega}\times\mathbf{r})$ can be expanded using the vector quantities of velocity and rotational speed as follows:

$$\boldsymbol{\Omega}\times(\boldsymbol{\Omega}\times\mathbf{r})=(0,0,\Omega)\times\begin{bmatrix}\underline{i_r} & \underline{i_\theta} & \underline{i_k}\\ 0 & 0 & \Omega\\ r & \theta & z\end{bmatrix}=(0,0,\Omega)\times(-\Omega\theta,\Omega r,0), \tag{5.7}$$

$$\boldsymbol{\Omega}\times(\boldsymbol{\Omega}\times\mathbf{r})=(0,0,\Omega)\times(-\Omega\theta,\Omega r,0)=\begin{bmatrix}\underline{i_r} & \underline{i_\theta} & \underline{i_k}\\ 0 & 0 & \Omega\\ -\Omega\theta & \Omega r & 0\end{bmatrix}=-\Omega^2 r\underline{i_r}-\Omega^2\theta\underline{i_\theta}, \tag{5.8}$$

and the Coriolis acceleration can be expanded to

$$2\boldsymbol{\Omega}\times\mathbf{v}=2\begin{bmatrix}\underline{i_r} & \underline{i_\theta} & \underline{i_k}\\ 0 & 0 & \Omega\\ -\mathrm{v}_r & \mathrm{v}_\theta & 0\end{bmatrix}=-2\Omega\cdot\mathrm{v}_\theta\underline{i_r}-2\Omega\cdot\mathrm{v}_r\underline{i_\theta}\,. \tag{5.9}$$

Hence, the Navier-Stokes equation can be written in the two main component directions of the rotating frame, as shown below.

For the radial component,

$$\left((\underline{\mathrm{v}}\cdot\nabla)\underline{\mathrm{v}}\right)_\mathrm{r}-\Omega^2 r\underline{i_r}-2\Omega\cdot\mathrm{v}_\theta\underline{i_r}=-\frac{1}{\rho}\frac{\partial \mathrm{P}}{\partial r}\underline{i_r}+\frac{\mu}{\rho}\left(\nabla^2\underline{\mathrm{v}}\right)_\mathrm{r}, \tag{5.10}$$

where

$$\left((\underline{\mathrm{v}}\cdot\nabla)\underline{\mathrm{v}}\right)_\mathrm{r}=\left(\mathrm{v}_\mathrm{r}\frac{\partial \mathrm{v}_\mathrm{r}}{\partial \mathrm{r}}+\frac{\mathrm{v}_\theta}{\mathrm{r}}\frac{\partial \mathrm{v}_\mathrm{r}}{\partial\theta}+\mathrm{v}_z\frac{\partial \mathrm{v}_\mathrm{r}}{\partial z}-\frac{\mathrm{v}_\theta^2}{\mathrm{r}}\right), \tag{5.11}$$

$$\left(\nabla^2\underline{\mathrm{v}}\right)_\mathrm{r}=\left(\frac{\partial^2\mathrm{v}_\mathrm{r}}{\partial \mathrm{r}^2}+\frac{1}{\mathrm{r}}\frac{\partial \mathrm{v}_\mathrm{r}}{\partial r}+\frac{1}{r^2}\frac{\partial^2\mathrm{v}_\mathrm{r}}{\partial\theta^2}+\frac{\partial^2\mathrm{v}_\mathrm{r}}{\partial z^2}-\frac{\mathrm{v}_\mathrm{r}}{\mathrm{r}^2}-\frac{2}{r^2}\frac{\partial \mathrm{v}_\theta}{\partial\theta}\right). \tag{5.12}$$

It can be assumed that the radial component of the fluid velocity vector is mainly a function of the radial position in the frame "***r***", independent of the "***z***"

component, and independent of the "***θ***" component. Simplifying Equation 5.10, the following expression is obtained

$$\left(v_r\frac{\partial v_r}{\partial r}-\frac{v_\theta^2}{r}\right)\underline{i_r}-\Omega^2 r\underline{i_r}-2\Omega\cdot v_\theta\underline{i_r}=-\frac{1}{\rho}\frac{\partial P}{\partial r}\underline{i_r}+\frac{\mu}{\rho}\left(\frac{\partial^2 v_r}{\partial r^2}+\frac{1}{r}\frac{\partial v_r}{\partial r}-\frac{v_r}{r^2}\right)\underline{i_r}. \quad (5.13)$$

For the angular component,

$$\left((\underline{v}\cdot\nabla)\underline{v}\right)_\theta-\Omega^2\theta\underline{i_\theta}-2\Omega\cdot v_r\underline{i_\theta}=-\frac{1}{\rho r}\frac{\partial P}{\partial\theta}\underline{i_\theta}+\frac{\mu}{\rho}\left(\nabla^2\underline{v}\right)\underline{i_\theta}, \quad (5.14)$$

where,

$$\left((\underline{v}\cdot\nabla)\underline{v}\right)_\theta=\left(v_r\frac{\partial v_\theta}{\partial r}+\frac{v_\theta}{r}\frac{\partial v_\theta}{\partial\theta}+v_z\frac{\partial v_\theta}{\partial z}-\frac{v_r v_\theta}{r}\right), \quad (5.15)$$

$$\left(\nabla^2\underline{v}\right)_\theta=\left(\frac{\partial^2 v_\theta}{\partial r^2}+\frac{1}{r}\frac{\partial v_\theta}{\partial r}+\frac{1}{r^2}\frac{\partial^2 v_\theta}{\partial\theta^2}+\frac{\partial^2 v_\theta}{\partial z^2}-\frac{v_\theta}{r^2}+\frac{2}{r^2}\frac{\partial v_r}{\partial\theta}\right). \quad (5.16)$$

In this case, the tangential component of the fluid velocity vector is independent of the "***z***" component and independent of "***θ***". The tangential component of the fluid velocity vector can be assumed as a function of the position in the radial "***r***" direction. Hence, Equation 5.14 can be further simplified as follows

$$\left(v_r\frac{\partial v_\theta}{\partial r}-\frac{v_r v_\theta}{r}\right)\underline{i_\theta}-\Omega^2\theta\underline{i_\theta}-2\Omega\cdot v_r\underline{i_\theta}=-\frac{1}{r}\frac{\partial P}{\partial\theta}\underline{i_\theta}+\frac{\mu}{\rho}\left(\frac{\partial^2 v_\theta}{\partial r^2}+\frac{1}{r}\frac{\partial v_\theta}{\partial r}-\frac{v_\theta}{r^2}\right)\underline{i_\theta} \quad (5.17)$$

In order to continue with the analysis, further simplifications are needed; in this context, the dimensionless Rossby and Ekman numbers were considered in order to evaluate the contributions of the convective and viscous terms in the Navier-Stokes equation. The Rossby number is defined as the ratio of the convective to the Coriolis forces while the Ekman number represents the ratio of

the viscous to the Coriolis forces; Equations 5.18 and 5.19 represent the Rossby and Ekman numbers, respectively.

$$R_o = \frac{U}{\Omega L} = \frac{U}{\Omega R} \tag{5.18}$$

$$E_k = \frac{\nu}{\Omega L^2} = \frac{\nu}{\Omega W^2} \tag{5.19}$$

where U represents the fluid velocity, Ω the rotational speed, ν the kinematic viscosity and L a geometric length scale related to the fluid flow analysis. However, the magnitude of "**L**" is not equal in both equations because it depends on the component velocity vector analyzed and the geometry of the unit. Convective contributions to the radial velocity component take place mainly in the radial direction, and therefore "**L**" represents the radius of the distributor (L = R = 0.15 m). Similarly, viscous contributions to the radial velocity component take place mainly in the axial direction "***z***"; hence, "**L**" represents the distributor's width (L = W = 0.1 m). Likewise, convective contributions to the tangential velocity component take place in the tangential direction "***θ***" and "**L**" may be represented approximately by the distributor's perimeter (L = πD = 1.25664 m). The viscous contributions to the tangential velocity component take place mainly in the axial "***z***" direction; thus "**L**" represents the distributor's width (L = W = 0.1 m).

In order to evaluate the nondimensional numbers, experimental conditions and geometry of the RFB unit are referred. The kinematic viscosity of air is approximately 0.141 cm^2/s and the simulated gravity forces of 10, 20 30 and 40 times normal gravity force occurred when the rotating speeds were 22.1, 31.3,

38.3 and 44.3 rad/s, respectively. Using these data, the Rossby and Ekman numbers were estimated for the conditions of the experiment and the results are shown in Table 5.2, for the radial component velocity and Table 5.3 for the tangential velocity component.

Table 5.2 Values of the Dimensionless Ro and Ek Numbers for the Radial Component of the Fluid Velocity

		Radial Component of the Velocity				
Simulated Gravity	Rotation Speed	Gas Velocity	Ekman's Length	Rossby's Length	Ekman Number	Rossby Number
G (m/s^2)	(rd/s)	U (cm/s)	L (cm)	L (cm)	Ek	Ro
10	22.096	2	10	15	6E-05	0.006
10	22.096	3	10	15	6E-05	0.0091
10	22.096	12	10	15	6E-05	0.0362
20	31.311	2.5	10	15	4E-05	0.0053
20	31.311	4	10	15	4E-05	0.0085
20	31.311	14.5	10	15	4E-05	0.0309
30	38.328	3	10	15	4E-05	0.0052
30	38.328	5	10	15	4E-05	0.0087
30	38.328	16	10	15	4E-05	0.0278
40	44.297	5	10	15	3E-05	0.0075
40	44.297	6.5	10	15	3E-05	0.0098
40	44.297	18	10	15	3E-05	0.0271

Table 5.3 Values of the Dimensionless Ro and Ek Numbers for the Tangential Component of the Fluid Velocity

		Tangential Component of the Velocity				
Simulated Gravity	Rotation Speed	Gas Velocity	Ekman's Length	Rossby's Length	Ekman Number	Rossby Number
G (m/s^2)	(rd/s)	U (cm/s)	L (cm)	L (cm)	Ek	Ro
10	22.096	1	10	125	6E-05	0.0004
10	22.096	10	10	125	6E-05	0.0036
10	22.096	100	10	125	6E-05	0.0362
20	31.311	1	10	125	4E-05	0.0003
20	31.311	10	10	125	4E-05	0.0026
20	31.311	100	10	125	4E-05	0.0255
30	38.328	1	10	125	4E-05	0.0002
30	38.328	10	10	125	4E-05	0.0021
30	38.328	100	10	125	4E-05	0.0209
40	44.297	1	10	125	3E-05	0.0002
40	44.297	10	10	125	3E-05	0.0018
40	44.297	100	10	125	3E-05	0.0181

According to the results shown in Tables 5.2 and 5.3, the results of the Ekman number imply that the viscous terms in Equations 5.13 and 5.17 can be neglected; however, the Rossby number requires a more careful evaluation since it is not that small. From the tables it can be seen that the Rossby number becomes small at low fluid gas velocities so that convective terms can be neglected, but as the fluid flow velocity increases, the Rossby number becomes significant, and convective terms cannot be neglected. The fluidization of agglomerates of nanoparticles of Aerosil® R974 and R972 required relatively low fluid velocities and therefore the convective terms in Equations 5.13 and 5.17 can be neglected. However, in the fluidization of Aeroxide® P25 and agglomerates of micron size particles, the fluid velocities are higher and the convective terms in Equations 5.13 and 5.17 should not be ignored.

The dimensionless form of the Navier-Stokes equation at steady state condition is (Vanyo, 2001):

$$R_O\left(\mathbf{v}\cdot\nabla\right)\mathbf{v}+2\mathbf{k}\times\mathbf{v}=-\nabla\mathbf{p}+E_k\nabla^2\mathbf{v} \tag{5.20}$$

where the pressure term includes the effect of the centripetal force according to

$$\nabla\mathbf{p}=\nabla\left[\mathbf{p}^*+\rho\Phi-\frac{1}{2}\rho\left(\Omega\times\mathbf{r}\right)\bullet\left(\Omega\times\mathbf{r}\right)\right] \tag{5.21}$$

by using the identity $\Omega\times\left(\Omega\times\mathbf{r}\right)=-\frac{1}{2}\left(\Omega\times\mathbf{r}\right)\bullet\left(\Omega\times\mathbf{r}\right)$. Equation 5.20 allows us to make further simplifications based on the Rossby and Ekman number values.

Therefore, when fluidizing agglomerates of nanoparticles of Aerosil® R974 and R972 using a very low gas flow, Equation 5.13 can be simplified to:

$$-\Omega^2 r\underline{i_r} - 2\Omega \cdot v_\theta \underline{i_r} = -\frac{1}{\rho}\frac{\partial P}{\partial r}\underline{i_r}\,; \tag{5.22}$$

and Equation 5.14 can be neglected due to expected symmetry of the flow because of the predominance of the rotating distributor in the flow pattern and the relatively low gas pressure at the inlet of the chamber, i.e.; assuming that the initial and boundary conditions are independent of θ and trying to find a solution with the same property.

However, when fluidizing micron size particles and Aeroxide® P25, the Rossby number cannot be neglected since the convective terms can modify the pressure in the region of study. Furthermore, the boundary and initial conditions are dependent on θ due to the asymmetric gas inlet, so that Equations 5.13 and 5.17 become:

$$\left(v_r\frac{\partial v_r}{\partial r} - \frac{v_\theta^2}{r}\right)\underline{i_r} - \Omega^2 r\underline{i_r} - 2\Omega \cdot v_\theta \underline{i_r} = -\frac{1}{\rho}\frac{\partial P}{\partial r}\underline{i_r}\,, \tag{5.23}$$

$$\left(v_r\frac{\partial v_\theta}{\partial r} + \frac{v_\theta}{r}\frac{\partial v_\theta}{\partial \theta} - \frac{v_r v_\theta}{r}\right)\underline{i_\theta} - \Omega^2\theta\underline{i_\theta} - 2\Omega \cdot v_r \underline{i_\theta} = -\frac{1}{\rho r}\frac{\partial P}{\partial \theta}\underline{i_\theta}\,. \tag{5.24}$$

These equations (5.22, 5.23 and 5.24) show that it is very difficult to estimate the experimental pressure drop with a theoretical model, but they allow us to understand the factors, such as the radial and tangential fluid velocities and the boundary conditions, that can modify the pressure drop values in the region of study. Equation 5.22 reduces to the theoretical model of Kao et al. (1986) Equation 5.5, when the tangential velocity of the fluid with respect to the rotating frame is zero, which only occurs when considering a rigid body rotation and at

certain gas flow rates. A comparison between these equations is shown in Figure 5.12.

$$\frac{1}{\rho}\frac{dP}{dr} \propto \Omega^2 r \qquad \frac{1}{\rho}\frac{\partial P}{\partial r} \propto \Omega^2 r + 2\Omega \cdot v_\theta$$

(a) Kao et al. model (1986) (b) This work's model

Figure 5.12 Comparison between the model for the pressure drop of Kao et al. (1986) and the present work.

Equations 5.22 and 5.23 can explain the higher experimental pressure drop than expected. The increase in the bed pressure drop not only have been found for Aerosil® R974 and R972, which is about three times the theoretical bed pressure drop, but also in the experimental data reported by Matsuda et al. (2001) as shown in Figure 5.13. According to our model, it is believed that the increase in the bed pressure drop is due to the Coriolis forces, a term that was neglected in past theoretical models.

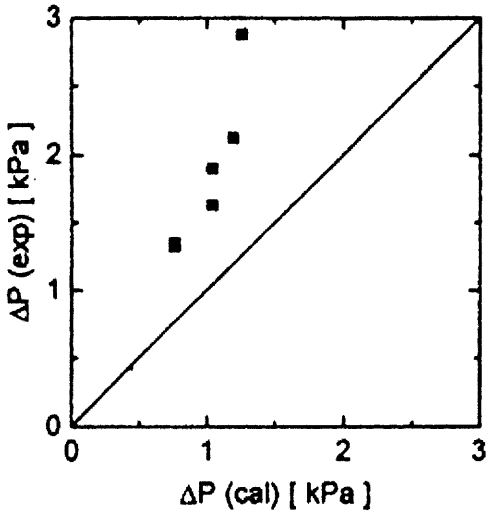

Figure 5.13 Comparison between calculated and experimental values for the bed pressure drop (Matsuda et al. 2001). Fluidization of ultrafine particles in a RFB.

Since the experimental measurements of the pressure drop were done in the radial direction, then Equations 5.22 and 5.23 are more significant for comparison purposes; however, Equation 5.24 shows that since the boundary conditions are θ dependent, this equation needs to be solved to determine the magnitude of the tangential velocity of the fluid, which will depend on the initial and boundary conditions.

In order to verify that the tangential fluid velocity component can differ from the rotating frame velocity, FLUENT 6.1 was used to predict the flow patterns and other parameters in the rotating fluidized bed system. This commercial software is capable of handling complex geometries; and after iteration, the velocity, density and pressure profiles were obtained at the desired cross sections as shown in figures below.

The simulation region is a rotating fluidized bed system which consists of a cylindrical chamber with an outer diameter of 50 cm and a height of 15 cm. The chamber has a rectangular tangential entry for the gas with a length that matches the chamber's height of 15 cm and a 4 cm width with a gas outlet cylinder of length of 1 meter coaxially connected to the center of the chamber. Inside the static cylindrical chamber, there is a moving cylindrical mesh set with a diameter of 40 cm, a height of 10 cm and 3 mm of thickness. The geometry and meshes were constructed by Gambit from Fluent Inc., which established a total of around 320,000 tetrahedral meshes that were used in this simulation. Figure 5.14 and 5.15 shows details of the geometries used in the computational calculations.

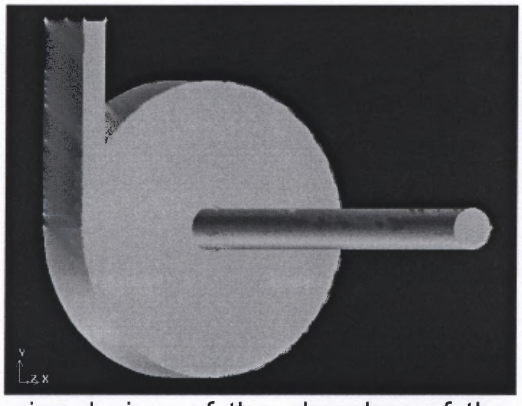

Figure 5.14 Tridimensional view of the chamber of the RFB unit used in the numerical simulations.

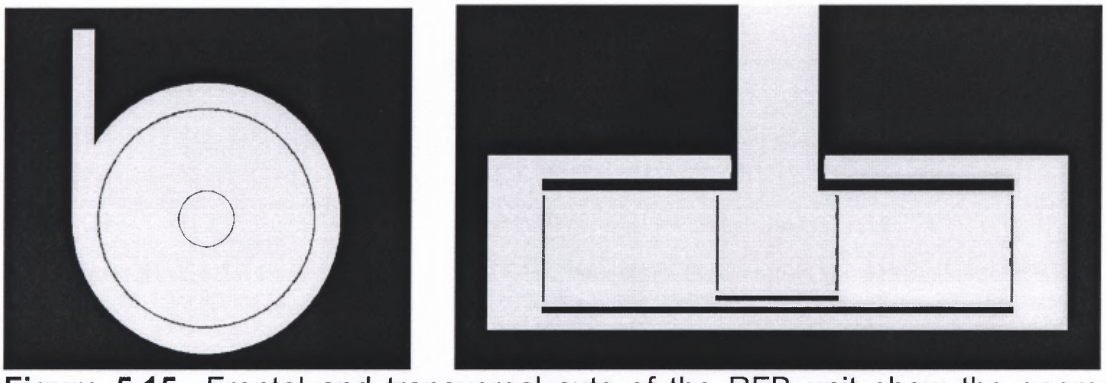

Figure 5.15 Frontal and transversal cuts of the RFB unit show the geometry used for numerical simulation purposes.

In order to have a better understanding of the dynamic behavior of gas/particle flow, a simpler case of a single phase (gas) system was studied as a first step. In these simulations, a coupled solver and implicit formulation were employed considering their stability and fast convergence. The gas media used in this computation is regarded to be an ideal gas with properties equals those of air. Since the gas speed is relatively high inside the computational field, it was treated as a compressible media instead of incompressible. The standard κ-ε *turbulence model* was used to describe the turbulence behavior for its robustness, reliability, and reasonable accuracy.

Since the density of the fluid plays a significant role in all the equations previously shown, the assumption of previous models of treating the gas as an incompressible fluid in the theoretical approach had to be verified; thus, the densities of the fluid at different inlet velocities and constant rotating speeds are shown in Figure 5.16. As shown, the density of the air increases with the volumetric flow does so, but for low flow conditions the assumption of a constant fluid density is valid and the fluid media can be treated either as a compressible or incompressible system.

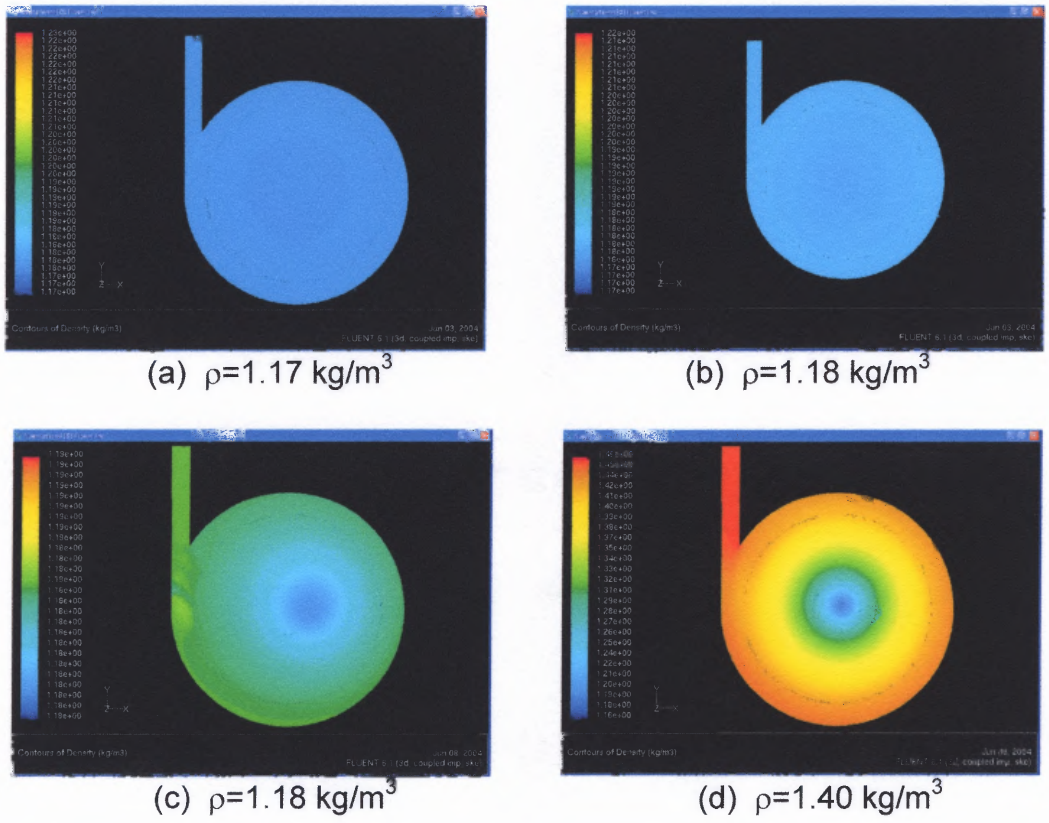

(a) ρ=1.17 kg/m^3 (b) ρ=1.18 kg/m^3

(c) ρ=1.18 kg/m^3 (d) ρ=1.40 kg/m^3

Figure 5.16 Contours of density of the gas at constant angular speed of 420 rpm (40 times gravity) (a) 2 m/s at the inlet, 9.5 cm/s radial velocity at distributor; (b) 6 m/s at the inlet, 28.6 cm/s radial velocity at distributor; (c) 12 m/s at the inlet, 57.3 cm/s radial velocity at distributor; (d) 60 m/s at the inlet, 286.5 cm/s radial velocity at distributor.

As explained in the theoretical approach of the rotating fluidized bed model, the tangential component of the fluid velocity vector can change the magnitude of the pressure along the radial direction if the Coriolis term becomes significant. Hence, a change in the tangential velocity was sought; for this purposes, the rotating speed was kept constant and the velocity of the gas at the entry of the chamber was changed. The results of these numerical calculations using Fluent® are shown in the contours of velocity in Figure 5.17.

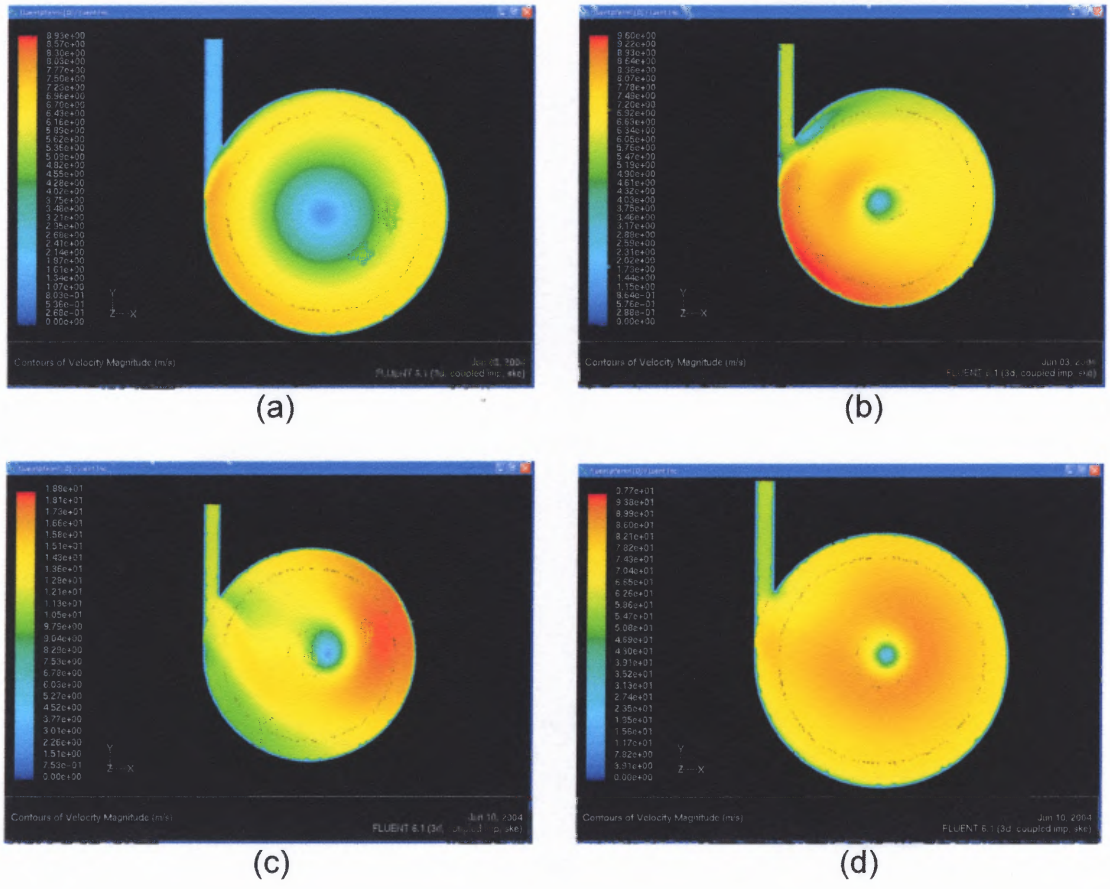

Figure 5.17 Contours of fluid velocity having the distributor rotating at a constant angular speed of 420 rpm (40 times gravity) (a) 2 m/s at the inlet, 9.5 cm/s radial velocity at distributor; (b) 6 m/s at the inlet, 28.6 cm/s radial velocity at distributor; (c) 12 m/s at the inlet, 57.3 cm/s radial velocity at distributor; (d) 60 m/s at the inlet, 286.5 cm/s radial velocity at distributor.

Figure 5.17 requires further explanation. The tangential fluid velocity component is extremely large compared to the radial fluid velocity; therefore, the contribution to the magnitude of the velocity vector from the radial velocity is almost negligible in the contours of fluid velocity shown; therefore, the changes in color observed in the figures are due to changes in the tangential velocity. In all four cases (a, b, c & d) the tangential velocity of the distributor (outer dotted circumference) is about 8.83 m/s; therefore, if the fluid velocity in the proximity of the distributor differs from 8.83 m/s a Coriolis effect is expected. Figure 5.17 (a) shows that the fluid velocity has an approximate value of 6.43 m/s in the proximity of the distributor, 2.4 m/s less than at the distributor; Figure 5.17 (b) shows that the tangential velocity of the fluid in the proximity of the entry is almost equal to the distributor's velocity (8.8 m/s), however, the tangential velocity reduces as the fluid moves away from the entry falling to a value of about 6 m/s; furthermore, this figure shows that the chamber flow field is not symmetrical due to the asymmetrical boundary conditions. In Figure 5.17 (c), the fluid velocity at the entrance (12 m/s) of the chamber is even higher than the tangential velocity of the distributor (8.83 m/s), hence the tangential velocity of the fluid in the proximity of the distributor and the entrance (10 m/s) is slightly higher than the distributor's velocity. However, at the opposite end of the entrance, the velocity of the fluid has increased to 18 m/s; once again, the tangential velocity of the fluid respect to the distributor is neither equal nor constant along the angular component. In Figure 5.17 (d), the fluid velocity at the entrance (60 m/s) is a lot larger than the tangential velocity of the distributor (8.83

m/s) so that the fluid velocity in the whole system is dominated by the velocity at the entry, but at this point, convective forces play a significant role.

Figure 5.18 shows the contours of static pressure for the four different inlet velocities. It can be seen that in cases (b) and (c) the lowest pressure in the chamber does not match exactly with the geometrical center and that the pressure field is not symmetrical. Since the fluid velocity is also pressure driven, changes in the contours of pressure imply changes in the velocity vectors.

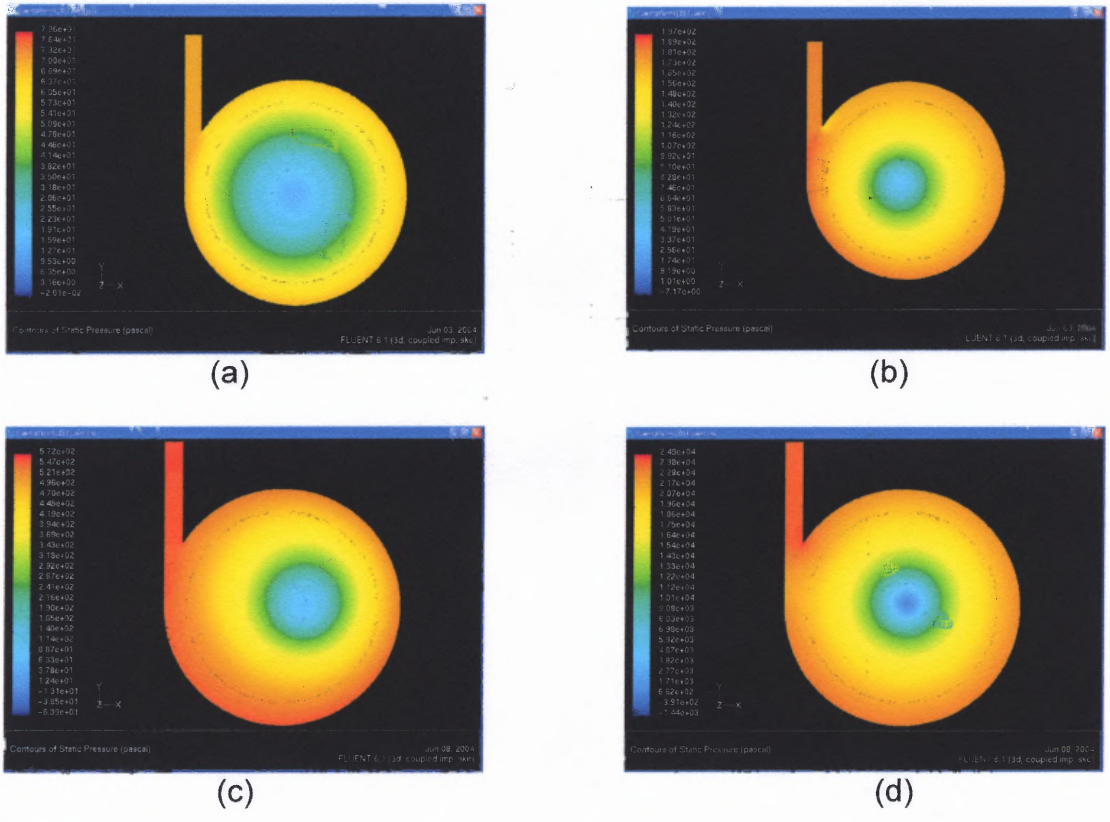

Figure 5.18 Contours of static pressure having the distributor rotating at a constant angular speed of 420 rpm (40 times gravity) (a) 2 m/s at the inlet, 9.5 cm/s radial velocity at distributor; (b) 6 m/s at the inlet, 28.6 cm/s radial velocity at distributor; (c) 12 m/s at the inlet, 57.3 cm/s radial velocity at distributor; (d) 60 m/s at the inlet, 286.5 cm/s radial velocity at distributor.

Figure 5.19 shows the contours of the velocity magnitude inside of the rotating frame when the distributor has an angular speed of 211 rpm. As before, the velocity of the fluid gas at the inlet of the unit was changed to values of 2, 6, 12 and 60 m/s. Again, the tangential fluid velocity component is changing in both the radial and angular directions.

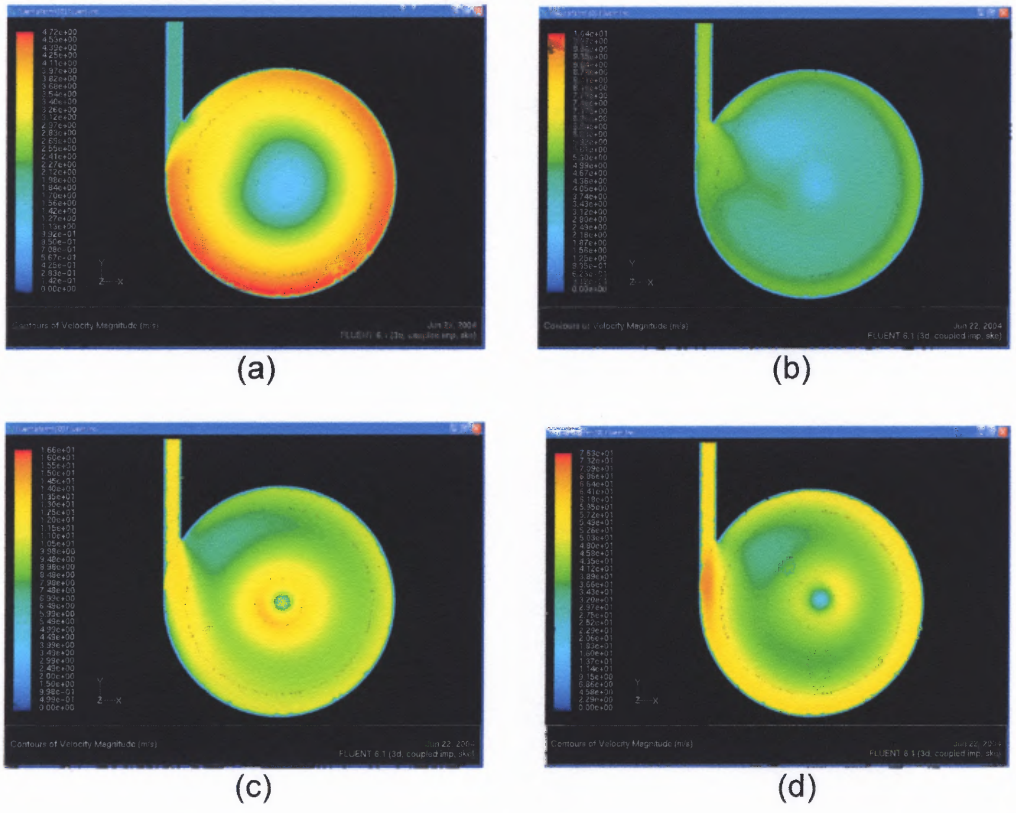

Figure 5.19 Contours of fluid velocity having the distributor rotating at a constant angular speed of 211 rpm (10 times gravity) (a) 2 m/s at the inlet, 9.5 cm/s radial velocity at distributor; (b) 6 m/s at the inlet, 28.6 cm/s radial velocity at distributor; (c) 12 m/s at the inlet, 57.3 cm/s radial velocity at distributor; (d) 60 m/s at the inlet, 286.5 cm/s radial velocity at distributor.

A better explanation of the difference between the tangential fluid velocity and the tangential velocity of the rotating frame can be deduced from Figure 5.20, which shows the tangential velocity of the rotating frame as a function of the radial position (solid line without dots) and the tangential fluid velocities as a

function of the radial position of the different inlet gas velocities (data extracted from the contours of velocity). As shown in this figure, the tangential velocity of the fluid gas can be greater or lesser than the tangential velocity of the rotating frame, which means that the magnitude of V_θ can be either positive or negative. This fact demonstrates that the tangential velocity of the fluid is not necessarily equal to the tangential velocity of the rotating frame, condition assumed for past models (rigid body rotation).

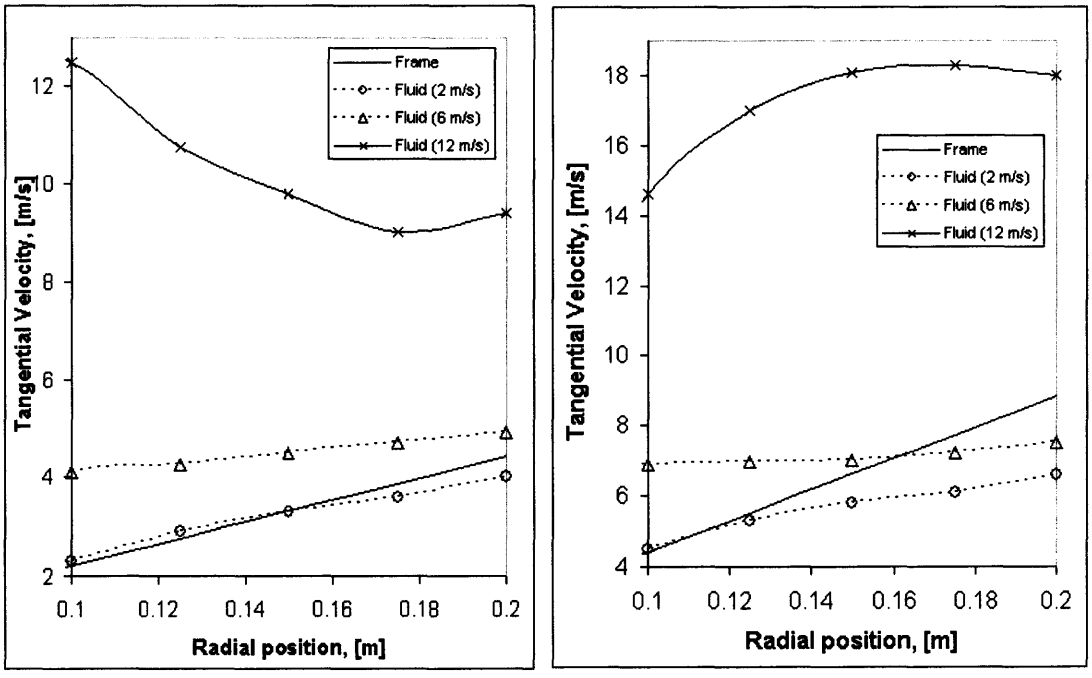

Figure 5.20 Tangential velocities of the frame and the fluid as a function of the radial position in the chamber. These magnitudes were obtained from the contours of velocity. Different curves correspond to a different inlet velocity of the fluid. The value of V_θ can be obtained by subtracting the velocity of the frame from the velocity of the fluid.

Since the tangential velocity of the fluid could be significant in some cases, Coriolis effects have to be considered in the calculation of the pressure drop across the region of interest as shown by Equation 5.22. This equation can

be further applied to the full fluidization of agglomerates of nanoparticles by considering the mix of agglomerates and gas as a new fluid. This new fluid will have a density equal to the weight of the powder divided by the entire fluidized bed volume when expanded; otherwise, the bulk density of the agglomerates can be modified by the empty bed voidage which depends on the bed expansion. In addition, the bed pressure drop has to be evaluated in the region of interest which is the fluidized bed. Thus, Equation 5.20 can be modified for estimating the bed pressure drop in the RFB as shown in Equation 5.25.

$$\frac{d\mathrm{P}}{dr} = \rho_a \left(1-\varepsilon\right)\left(\Omega^2 r + 2\Omega \cdot \mathrm{V}_{\theta(r,\theta)}\right) \tag{5.25}$$

In this equation, the tangential velocity of the fluid bed is expected to be positive and its behavior different than the tangential velocity of the fluid gas only. For fluidization of agglomerates of nanoparticles of fumed silica, the fluidized bed of agglomerates is expected to behave like a denser fluid with much higher viscosity than the air; it is believed that this higher viscosity will transfer the tangential velocity of the distributor over the entire bed, maintaining an approximate constant value of the tangential velocity in the radial direction in the bed region while the tangential velocity of the frame reduces; this effect increases by the fact that the fluidized bed height doubles the bed height at no fluidization, a behavior that does not occur during fluidization of micron size particles.

A nondimensional number *Cor* can be defined for evaluating the contribution of the Coriolis force to the total pressure drop:

$$\text{Cor} = \frac{\text{Coriolis forces}}{\text{Centrifugal forces}} = \frac{2\Omega v_\theta}{\Omega^2 r} = \frac{2v_\theta}{\Omega r}. \tag{5.26}$$

If this nondimensional number (Cor) is less than 0.05 (Cor < 0.05) then the Coriolis forces can be neglected, otherwise it should be considered in the calculations. The greatest difficulty is to find the value of the tangential velocity of the fluid (mixture of particulates suspended in the fluid gas) respect to the rotating frame, since it is a function of the radial and angular positions, the inlet fluid velocity and the static pressure inside of the chamber.

Since agglomerate of nanoparticles of Aerosil® R974 and R972 are much lighter than agglomerates of micron size particles, they can be easily dragged by the gas flow not only in the radial direction but in the tangential direction as well. The drag of these agglomerates in the radial and tangential direction implies the presence of an additional force which is related to the Coriolis effect; moreover, as mentioned before, a significant bed expansion was observed for agglomerates of R974 and R972, which does not occur when fluidizing agglomerates of micron size particles or even Aeroxide® P25.

A force balance on the agglomerate based on the equations previously explained is sketched in Figure 5.21. Here $\mathbf{V_r}$ is the velocity of the agglomerate in the radial direction reflected by the bed expansion while $\mathbf{V_\theta}$ is the velocity of the agglomerate in the tangential direction with respect to the rotating reference. In addition, in order to compensate for the centrifugal and Coriolis forces, the drag force has to have two components, in the radial and in the tangential directions.

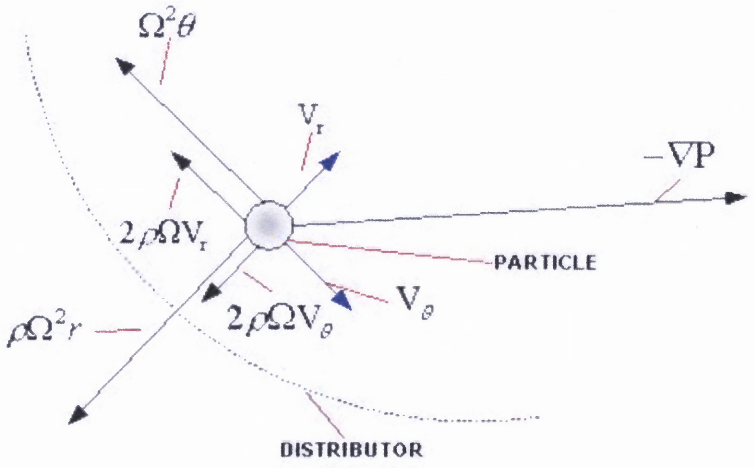

Figure 5.21 Schematic of the forces balance of the agglomerate in the proximities of the distributor showing velocity vectors (blue) and force vectors (black).

5.5 Conclusions

Agglomerates of nanoparticles can be fluidized in the RFB unit, as seen by the plateau region in the plots of bed pressure drop vs. gas flow velocity. The minimum fluidization velocity in a RFB is higher than in a conventional fluidized bed due to the large centrifugal force and other additional forces involved in the system. During fluidization, agglomerates of nanoparticles of Aerosil® R974 and R972 presented a significant bed expansion.

The pressure drop across the bed of agglomerates depends not only on the centripetal force but on the Coriolis force originated by the tangential velocity of the fluid gas which drags the agglomerates. This tangential velocity component of the fluid gas depends on the velocity of the fluid at the entrance of the chamber (volumetric flow rate), the rotational speed of the distributor and the pressure distribution inside of the chamber. A model that accounts for the

additional forces due to rotation of the frame and the fluid has been developed and it explains some of the discrepancies between experimentally measured pressure drop data when compared with previous theoretical models.

A significant difference in the tangential velocities of the fluid gas inside of the chamber was found between low gas flow rates (when fluidizing nanoparticles) and high gas flow rates (when fluidizing micron size particles). Moreover, for the fluidization of micron size powders, the convective term becomes important when calculating the bed pressure drop depending on the value of the Rossby number.

Further analysis of the rotating fluidized bed unit is required in order to fully evaluate the different forces present in this system. For example, a unit designed with a very large chamber diameter implies that the Coriolis forces are less important; in addition, elutriation of powder is expected to decrease since the centrifugal field can interact with the particles over a greater area. Moreover, the entrance of the fluid gas to the chamber could be modified in a way that the initial tangential velocity of the fluid can be made negligible or changed to a desired value. Regarding the instrumentation, the actual location of the pressure taps seems to be important because of the changes in pressure along the radial and angular directions as shown by the different contours of pressure obtained using the numerical calculations. Thus a different criterion to quantify the pressure drop in the system is required. In order to quantify the tangential velocity of the fluid in the chamber, it is necessary to install a device for measuring the gas velocity such as a Pitot tube; furthermore, additional Pitot

tubes should be installed close to the static pressure taps in order to quantify the total pressure.

From the experience of working with a RFB unit with a 40 cm diameter distributor, it can be concluded that an even larger size unit is required in order to properly measure all the variables in the system. This is necessary because agglomerates of nanoparticles require large volumes because of their low density and in many cases, coating or granulation of powders require the installation of devices inside of the chamber like nozzles, sprayers, and instrumentation such as Pitot tubes to measure local gas velocities.

REFERENCES

Bird, R. B., Stewart, W. & Lightfoot, E. (2001). Shell Momentum Balances and Velocity Distributions in Laminar Flow. *Transport Phenomena.* New York: John Wiley & Sons, Inc.

Brouwers, J. J. H. (2002). Phase separation in centrifugal fields with emphasis on the rotational particle separator. *Experimental Thermal and Fluid Science, 26,* 325-334.

Chen, Y. M. (1987). Fundamentals of a Centrifugal Fluidized Bed. *AIChE Journal, 33,* 722 - 727.

Coulaloglou, C. (1979). Fluidization of Permanently Magnetic Particle Beds. *US Patent 4132005.*

Gupta, C. K., & Sathiyamoorthy, D. (1999). Generalities and Basics of Fluidization (pp.1 – 51). *Fluid Bed Technology in Materials Processing.* New York: CRC Press LLC.

Ganzha, V. L. & Saxena, S. C. (2000). Hydrodynamic behavior of magnetically stabilized fluidized beds of magnetic particles. *Powder Technology, 107,* 31 – 35.

Hristov, J. Y. (1998). Fluidization of ferromagnetic particles in a magnetic field Part 2: Field effects on preliminary gas fluidized bed. *Powder Technology, 97,* 35 - 44.

Jackson, R. (2000). Fluidization Fundamentals. *The Dynamics of Fluidized Particles.* London: Cambridge University Press.

Jang, H. D. (2001). Experimental study of synthesis of silica nanoparticles by a bench-scale diffusion flame reactor. *Powder Technology, 119,* 102 - 108.

Kao, J., Pfeffer, R., Tardos, G. I. (1987). On Partial Fluidization in Rotating Fluidized Beds. *AIChE Journal, 33,* 858 - 860.

Kunii, D., Levenspiel, O. (1991). Introduction. *Fluidization Engineering.* Elsevier Science and Technology Books.

Lu, X., Li, H. (2000). Fluidization of $CaCO_3$ and Fe_2O_3 particle mixtures in a transverse rotating magnetic field. *Powder Technology, 107,* 66 - 78.

Mangold, H., Kerner, D., Kleinschmit, P. (1999) Pyrogenic silica, process for the production thereof and use. *US Patent 5976480.*

Matsuda, S., Hatano, H., Muramoto, T. & Tsutsumi, A. (2001). Particle and Bubble Behavior in Ultrafine Particle Fluidization. *Fluidization X,* 501-507. Beijing.

Nam, C., Pfeffer, R., Dave, R. N. & Sundaresan, S. (2003). Aerated Vibrofluidization of Silica Nanoparticles. *AIChE Journal, submitted.*

Pratsinis, E., Stark, W. (2002). Aerosol flame reactors for manufacture of nanoparticles. *Powder Technology, 126,* 103 - 108.

Qian, G., Bagyi, I., Burdick, I., Pfeffer, R., Shaw, H. & Stevens, J. (2001). Gas-Solid Fluidization in a Centrifugal Field. *AIChE Journal, 47,* 1022 - 1034.

Richardson, J. F. & Zaki, W. N. (1954). Sedimentation and Fluidisation: Part I. *Trans. Instn. Chem. Engrs. 32.*

Rietema, K. (1991). Particle and Powder Characteristics (pp. 19 – 34). *The Dynamics of Fine Powders.* New York: Elsevier Science.

Rietema, K. (1991). Mechanics of Powders at Rest (pp. 39 – 49). *The Dynamics of Fine Powders.* New York: Elsevier Science.

Rhodes, M. J., Wang, X. S., Forsyth, A. J., Gan, K. S. & Phadtajaphan, S. (2001). Use of a magnetic fluidized bed in studying Geldart Group B to A transition. *Chemical Engineering Science, 56,* 5426 – 5436.

Rosensweig, R. (1987). Process for Magnetically Stabilizing a Fluidized Bed Containing Nonmagnetizable Particles and a Magnetizable Fluid. *US Patent 4668379.*

Seville, J.P.K., Tuzun, U., & Clift, R. (1997). Fluid Particle System (pp. 226 – 242). *Processing of Particulate Solids.* New York: Blackie Academic & Professional.

Singh, P., Solanky, T. K. S., Mudry, R., Pfeffer, R. & Dave R. (2001). Estimation of coating time in the magnetically assisted impaction process. *Powder Technology, 121,* 159-167.

Vanyo, J. P. (2001). Rotating Fluid Theory. *Rotating fluids in Engineering and Science.* New York: Dover Publications.

Wang, Y., Wei, F., Jin, Y. & Luo, T. (2000). Agglomerate Particulate Fluidization and E-particles. *Proceedings of CUChE-3.* Beijing: Tsinghua University Press.

Wang, Y., Gu, G., Wei, F. & Wu J. (2002). Fluidization and agglomerate structure of SiO_2 nanoparticles. *Powder Technology, 124,* 152-159.

Watano, S., Imada, Y., Hamada, K., Wakamatsu, Y., Tanabe, Y., R. Dave, et al. (2001). Microgranulation of fine powders by a novel rotating fluidized bed granulator. *Powder Technology, 131,* 250 - 255.

Wu, W. Y., Navada, A. & Saxena, S. C. (1997). Hydrodynamic characteristics of a magnetically stabilized air fluidized bed of an admixture of magnetic and non-magnetic particles. *Powder Technology, 90,* 39 – 46.

Zhu, C., Lin, C. H., Qian, G. H. & Pfeffer, R. (2001). Modeling of the Pressure Drop and Flow Field in a Rotating Fluidized Bed. *6th World Congress of Chemical Engineering.* Melbourne.

Zhu, C., Liu, G., Yu, Q., Pfeffer, R., Dave, R. & Nam, C. (2004). Sound Assisted Fluidization of Nanoparticle Agglomerates. *Powder Technology, 141,* 119 - 123.